University of Liège – Faculty of Applied Sciences

Hydromechanical modelling of a ventilation test in the Underground Research Laboratory of ANDRA

Master's Thesis submitted in partial fulfilment of the requirements
for the degree of Master in CIVIL ENGINEERING

Conducted by Công-Tâm THAI

Supervisor: Professor F. Collin

Jury Composition:

Prof. J-P. JASPART, president (University of Liège)

Prof. F. COLLIN, thesis supervisor (University of Liège)

Prof. R. CHARLIER, member (University of Liège)

Prof. F. NGUYEN, member (University of Liège)

Prof. A. LÉONARD, member (University of Liège)

Prof. P. GERARD, member (Brussels School of Engineering)

Academic Year 2014-2015

With these final words, I thereby dedicate this work
to my mother.

Acknowledgments

I would like to express my sincere gratitude to the people who helped me achieving this Master's thesis.

First of all, I would like to thank Prof. F. COLLIN for having accepted to supervise my thesis. It is thanks to him and to the lectures he gave me that I was able to enjoy working in such field. I am also grateful for always being able to find some spare time to answer to my questions and to give me remarks, opinions in order to advance.

My sincere thanks also go to B. PARDOEN, with whom I have the most learnt during this work. I thank him for his availability, and his precious help. To me, he was like a second supervisor.

Then, I would also like to thank the members of the geotechnical department who have provided me every now and then some precious pieces of advice.

My special thanks goes to my friends, those accepted to bear with me this particular challenge, those who accepted to read my work and those in the same situation as I was.

Eventually, I would like to thank my family for helping me during the hard times, and supporting me, as always.

Abstract

When producing electricity, nuclear energy plays an important role in our modern societies: more than 13 % of the world electricity production comes from nuclear sources. This share rises up to 75 % in France. With its 58 nuclear reactors among the 439 operational around the world, it is the country the most dependent on nuclear electricity. However, the nuclear wastes generated can be extremely harmful to man and nature, in such a way that it is crucial to isolate them. Deep geological storage was thus selected as a potential solution for the most critical wastes. Yet, the feasibility of such task is still under study. In France, ANDRA runs scientific research programs that investigate the storage possibilities in the Callovo-Oxfordian argillite, located at a depth between 400 and 600 m in the Meuse/Haute-Marne region.

An underground research laboratory (URL) was installed in the rock formation. It carries out series of experiments to study the thermal, hydraulic and mechanical behaviours of the rock formation following the disposal phase (excavation, wastes storage and sealing). Among these, the Saturation Damaged Zone (SDZ) experiment investigates the impact of the exploitation phase in the argillite through saturation/desaturation cycles (i.e. ventilation test). In particular, the excavation damaged zone (EDZ) and its evolution has to be characterised.

In this context, one of the main contributions of this work is to propose laws of behaviour that modify the hydraulic parameters on the basis of the mechanical variables, such that the hydraulic behaviour of the medium evolves in the same way regardless of the orientation. Furthermore, we developed a formulation able to describe correctly the EDZ by correlating the intrinsic permeability of the medium with the ratio of plasticity. Then, the influence of the ventilation test itself was examined in further details. Among the aspects discussed, the analysis of the influence of the mass transfer coefficient suggested that using values determined through drying tests was possible. In addition to that, the work also introduced the concept of anisotropy of the mechanical parameters and explores the limitations of the newly proposed formulation.

Résumé

Dans nos sociétés modernes, l'énergie nucléaire joue un rôle important lors de la production d'électricité : plus de 13% de la production d'électricité mondiale provient du nucléaire. En France, cette part monte jusqu'à 75%. Avec ses 58 réacteurs nucléaires parmi les 439 opérationnels dans le monde, c'est le pays le plus dépendant de l'électricité nucléaire. Cependant, cela génère des déchets radioactifs nocifs pour l'Homme et la nature ; de telle sorte qu'il faille à tout prix les isoler. Le stockage géologique profond a été sélectionné comme solution potentielle pour les déchets les plus critiques. Or, la faisabilité d'une telle tâche reste toujours en cours de recherche. En France, ANDRA mène des programmes de recherche dédiés à l'étude des possibilités de stocker dans les couches de l'argilite du Callovo-Oxfordien, situé entre 400 et 600 m de profondeur, dans la région de la Meuse/Haute-Marne.

Un laboratoire de recherche souterrain fut installé dans cette formation rocheuse. On y mène des séries d'expériences axées sur les comportements de nature thermique, hydraulique et mécanique que la roche adopte suite à la phase de stockage (excavation, entreposage des déchets et scellement). Parmi ces aspects, l'expérience de la zone endommagée saturée (SDZ) enquête l'impact de la phase d'exploitation sur l'argilite à travers des cycles de saturation/désaturation (i.e. test de ventilation). Plus particulièrement, il s'agit de caractériser la zone excavée endommagée (EDZ) ainsi que son évolution.

Dans ce contexte, une des majeures contributions de ce travail est de proposer des lois de comportement qui modifient les paramètres hydrauliques sur base des variables mécanique, de telle sorte que le comportement hydraulique du milieu évolue de la même manière et ce, peu importe l'orientation considérée. En outre, ce travail développe une formulation capable de décrire correctement l'EDZ en corrélant la perméabilité intrinsèque du milieu avec le ratio de plasticité. Ensuite, l'influence du test de ventilation en lui-même est étudiée plus en détails. Parmi les sujets abordés, l'analyse de l'influence du coefficient de transfert montre qu'il est possible de servir des valeurs déterminées au moyen de tests de séchage pour modéliser le test. A côté de cela, le travail introduit le concept d'anisotropie des paramètres mécaniques, et explore les limites du la nouvelle formulation proposée.

Enoncé

Le sujet de ce travail est la modélisation en couplage hydromécanique de l'expérience de ventilation SDZ du laboratoire souterrain de l'Agence Nationale pour la gestion des Déchets Radioactifs (ANDRA), situé à Bure en France.

L'agence est en charge de l'étude de la faisabilité et de la fiabilité à long terme d'un stockage de déchets nucléaires en couche géologique profonde faiblement perméable. Ces formations ont pour rôle de constituer une barrière naturelle ultime face à une éventuelle migration de radionucléides vers la biosphère. Plus précisément, les recherches effectuées au laboratoire de Bure se concentrent sur le stockage des déchets radioactifs de moyenne et haute activité à vie longue dans les argilites du Callovo-Oxfordien. L'expérience de ventilation SDZ, qui a lieu dans la galerie GED à une profondeur de 490 m sur le site de la Meuse/Haute-Marne, s'inscrit dans le cadre de ce programme de recherche.

L'expérience de ventilation SDZ est dédiée à l'étude de l'évolution de la zone endommagée de la galerie suite au processus d'excavation. Cette zone, appelée « Excavated Damaged Zone » (EDZ) est soumise à des chargements de nature mécanique d'une part, et de nature hydraulique d'autre part. La modélisation de cette expérience sera réalisée au moyen du code de calcul éléments finis « LAGAMINE » développé par l'Université de Liège. Au préalable, il convient de caractériser le matériau sur base d'essais triaxiaux réalisés en laboratoire, ainsi qu'au travers d'une recherche bibliographique.

Pour caractériser la structure et la taille de cette zone, un modèle numérique prenant en compte divers aspects sera élaboré. Sous l'hypothèse d'un milieu isotherme non saturé, le modèle mécanique de base est isotrope avec une loi élastoplastique à frottement interne. La particularité de ce mémoire est de proposer des lois de comportement qui modifient les paramètres hydrauliques sur base des variables mécaniques. Plus précisément, il s'agira de corréler l'évolution de la perméabilité intrinsèque du milieu avec une variable qui quantifie l'endommagement de la roche. De cette manière, le comportement hydraulique du milieu reste isotrope. Un modèle mécanique orthotrope sera également développé.

Enfin, ce travail de fin d'études abordera les conditions limites dites « non classiques » pour modéliser les échanges d'eau et de vapeur se produisant au sein d'une couche limite hydraulique, notamment par le biais de l'étude du coefficient de transfert d'évaporation.

Les membres du jury :

F.COLLIN R.CHARLIER F.NGUYEN A.LÉONARD P.GERARD

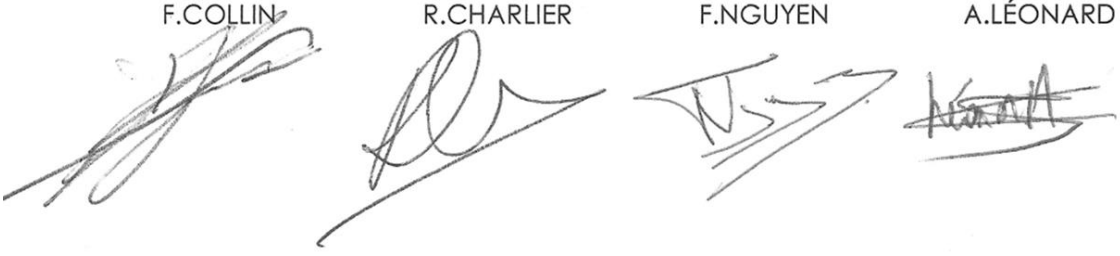

Table of Content

Table of Figures

List of Tables

1 Introduction

Producing electricity using the nuclear energy leads to the generation of radioactive wastes. Regarding High Level Wastes and Intermediate-level long-lived wastes, one solution adopted is the deep geological storage. However, the feasibility of such task is still under study. In Europe several research programs are carried out in different countries. Until now, the targeted geological formations are either composed of granitic or clayey rocks.

In France, ANDRA (Agence Nationale pour la gestion des Déchets Radioactifs) studies the feasibility of such task in the geological layers of the Callovo-Oxfordian argillite. For this purpose, ANDRA installed an underground research laboratory located at Bure in France, in which series of experiments are carried out to study the behaviour of the rock from a mechanical, hydraulic and thermal point of view.

Among them, the experiment SDZ investigates the evolution of the Excavated Damaged Zone (EDZ) following the exploitation phase by doing a ventilation test. The effects of the saturation/desaturation cycles are being studied. This work is aimed to simulate this ventilation test by means of a hydromechanical modelling.

This work is divided into 4 main parts. The first one explains the motivations and the context in which such experiment is realised. The second part is describes the mathematical model behind the phenomena we want to reproduce.

These models come with parameters. The next part is thus concentrated on the calibration of the parameters, on the basis of laboratory tests and of a preliminary bibliographic research.

The last part is entirely dedicated to the modelling of the ventilation test. The conditions are detailed and the values of the parameters are listed. Then, the simulation are discussed and analysed in details, before reaching to the conclusion.

2 General Context

2.1 Energy consumption

World energy consumption has been increasing for the past decades. In 2013, primary energy consumption reached a value of 12 730.4 $MToe$[1], that is to say +2.3 % with respect to the previous year. However, this increase slowed down compared to what has been observed throughout the last 15 years. In addition to that, there are regional disparities. The primary energy consumption in Europe and Eurasia decreased in 2013 by 0.3 %, while in other regions, the increase ranges from 1.7 % in Africa to 3.4 % in Asia [BP, 2014].

World energy production can be divided into several fuel uses. Figure 1 displays the distribution of the Total Energy Supply (TPES) in 2012. Among these energy sources, 4.8 % comes from nuclear contributions.

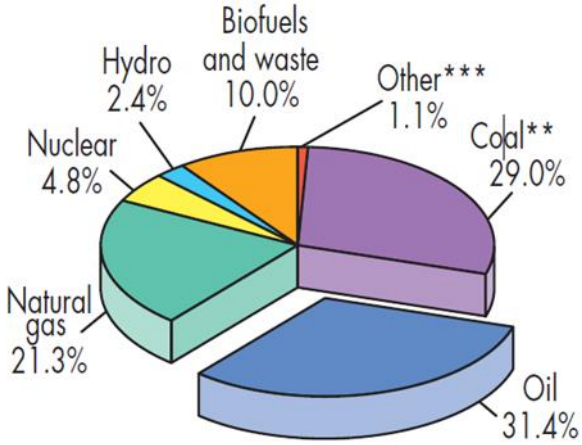

Figure 1: World fuel shares of Total Primary Energy Supply (TPES) in 2012. « Others » includes renewable energy sources other than hydroelectricity and biofuels & waste [IEA, 2014].

2.2 Nuclear energy

Nuclear energy refers to the energy produced by both nuclear fission and nuclear fusion. The former is the process in which "the nucleus of a heavy atom splits into lighter elements", while the latter is the process in which "two or more atomic nuclei collide at a very high speed and join to form a new type of atomic nucleus" [JEWETT, et al., 2010]. Both processes release a large amount of energy, but nuclear fusion does not produce high-level wastes (HLW) and therefore storage in deep geological layers is not needed. However, as nuclear fusion requires extreme temperature and pressure conditions, it is yet not used in the production of energy (experimental phase only). As a consequence, the term "Nuclear energy" will most likely apply to the production of energy using nuclear fission processes [Georgia State University, 2015] [Texas State Energy Conservation Office, 2015] [IEA, 2015].

Nuclear energy is essentially used for electricity production, but can be also found in several other applications, such as nuclear medicine (diagnosis and therapy), in agriculture (fertilisers and insect control), scientific researches, industries (industrial tracers, radiography, power sources, dating), and for military purposes [WNA, 2014a]. The following sections solely focus on the sectors linked to the production of electricity.

[1] Toe: ton of oil equivalent is the amount of energy released by burning one tonne of crude oil, which is approximately 42 Giga Joules.

2.2.1 Physical process

In typical nuclear reactors, the nuclear fission mechanism is induced by the bombardment of neutrons on the isotope 235 of uranium, which is thus called a *fissile nuclear fuel*. The reaction is the following:

$$^{235}_{92}U + ^{1}_{0}n \rightarrow ^{92}_{36}Kr + ^{141}_{56}Ba + 3\,^{1}_{0}n + 210\,MeV \qquad \textbf{(1)}$$

The isotope 235 becomes an isotope 236 as it absorbs a neutron. At this point, the isotope is in an excited phase, until a point where the energy inside is great enough to divide the nucleus into two parts (fission energy threshold). As a result, an atom of krypton 92 and one of Barium 141 are produced, and a huge amount of energy is liberated. This nuclear reaction can be amplified and controlled via a nuclear chain reaction, as each released neutron can trigger yet more events, releasing subsequently more neutrons, which in turn cause more fission.

Let us note that another process exists and is called spontaneous fission (radioactive decay), but is not used in industry. Other examples of fissile nuclear fuels are the isotope 238 of uranium and the isotope 239 of plutonium [ENS, 2015] [CHOPPIN, et al., 2002].

2.2.2 Electricity production

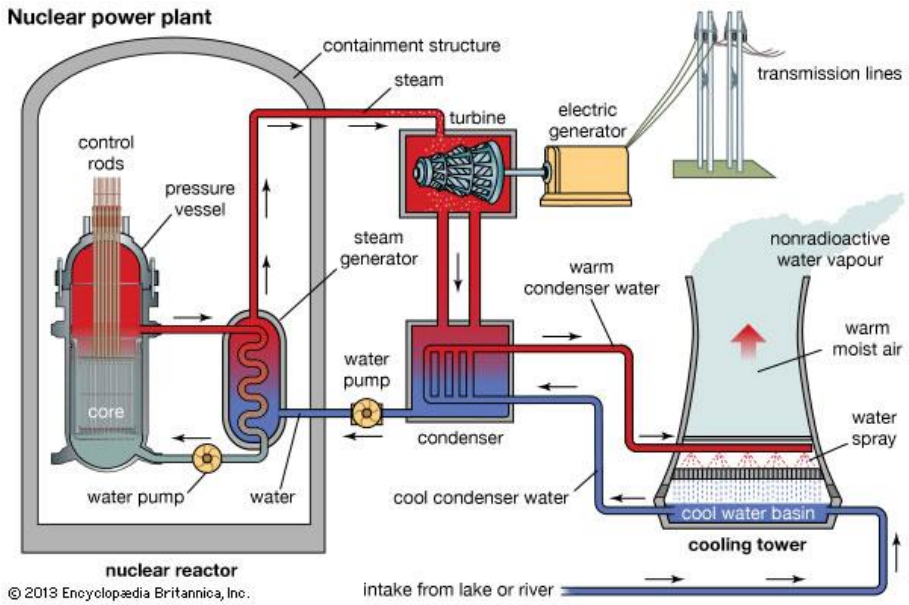

Figure 2: Sketch of a nuclear power plant using a PWR [Britannica, 2013].

The amount of energy produced by Equation 1 in the core of the reactor is used to heat the water. The steam produced activates a turbine which generates electricity. As mentioned above, nuclear fission processes lead to chain reactions. Control rods are put into the core of the reactor to absorb neutrons and therefore limit the fission rate. One of the most used reactors is the *Pressurised Water Reactor* (PWR). Figure 2 displays the general functioning of a nuclear power plant with PWR. Water in direct contact with the core is circulating in a primary loop (first system). It is heated at $330\,°C$ under $155\,bar$ of pressure. This heat is transferred to a secondary loop (second system), in which water is transformed into steam ($T = 280\,°C, P = 70\,bar$), and in turn activates the turbine. The third system is an open cycle which uses external water sources (e.g. river, sea) to cool the secondary loop [COPPOLANI, 2004]. Alternative models can be found around the world, and result most of the time from a combination of Rankine and Brayton cycles. For instance, putting turbines at high and low pressure (i.e. staged expansion) can increase the efficiency of the system [LÉONARD, 2012].

Other types of reactor can consume less radioactive resources, generate less nuclear waste, or use less imposing features, in exchange with other downsides [Britannica, 2015]. They vary on the composition of the core fuel (plutonium, uranium 238, or mix), the type of neutron moderator (graphite, deuterium, boiling water), and the heat-transfer fluid (water, lead, sodium) [WNA, 2015a] [CEA, 2014a] [CEA, 2014b].

Nuclear technology was discovered in the 1940s, in a context of war. Researches intended to generate power only began 10 years later. Figure 3 shows the time evolution of the nuclear electricity production. Commercialisation of nuclear energy was put in place in the 1960s in order to decrease the dependence on fossil fuels. However, the sector suffered some major economic decline and stagnation from the late 1970s until the beginning of the 21st century [WNA, 2014b]. This was mainly due to the safety concerns resulting from the Three Mile Island (1979) and Chernobyl (1986) incidents [IEA, 2015].

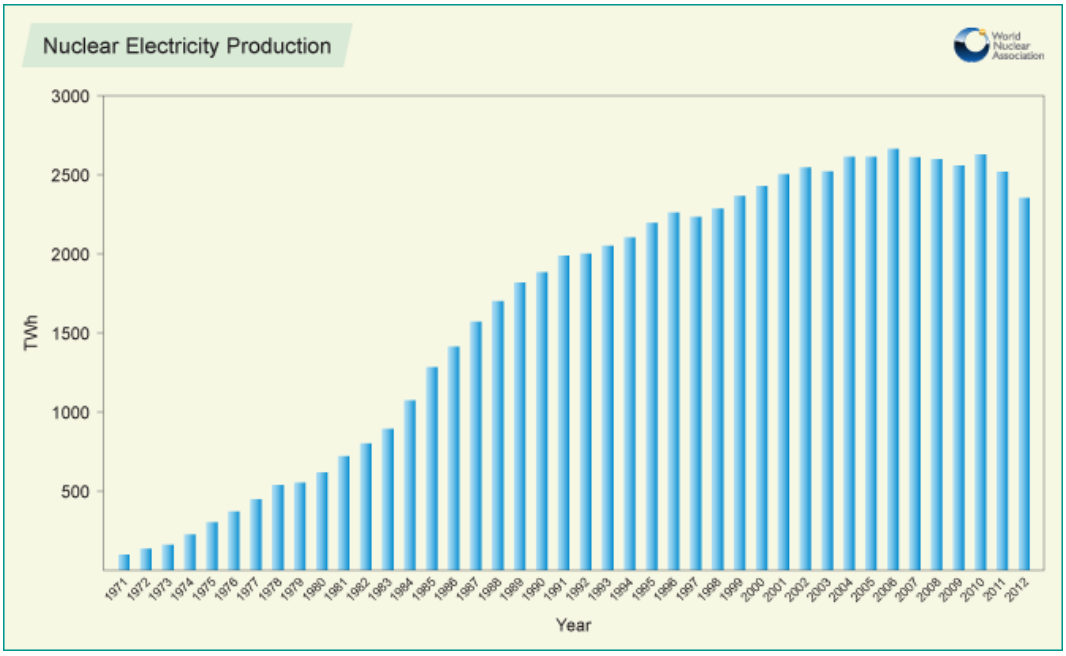

Figure 3: Evolution of nuclear electricity production throughout the years (in TWh) [WNA, 2014b].

Nowadays, the production of nuclear electricity has enormously decreased. Following the accident of Fukushima in 2011, several countries decided to change their energy policy regarding nuclear energy. Germany pushed forward his phasing-out of nuclear energy by taking offline eight nuclear power plants in the same year. Moreover, the phase-out of the remaining nine nuclear power plants is to be completed gradually by 2022. Switzerland and Belgium are willing to shut down all their nuclear plants by (respectively) 2034 and 2025 [Siemens, 2012]. A referendum in Italy stalled attempts to launch anew any nuclear plan.

On the other hand, most other countries around the world decided to maintain their nuclear program in order to ensure their energy independence [The Guardian, 2011]. These policies led to the drop of the production of nuclear electricity by 4% in 2011 and 6.9 % in 2012 [BP, 2012] [BP, 2013]. In contrast, the production went up by 0.9 % in 2013 [BP, 2014].

According to the WNA (World Nuclear Association), nuclear sources account nowadays for 13.4 % of the World Electricity Production (Figure 4) [WNA, 2014b]. Currently, there are 439 nuclear reactors operable in 31 countries, 2 in long-term shutdown, and 69 under construction (from which 34 are being built in Far East Asia) [IAEA, 2015a].

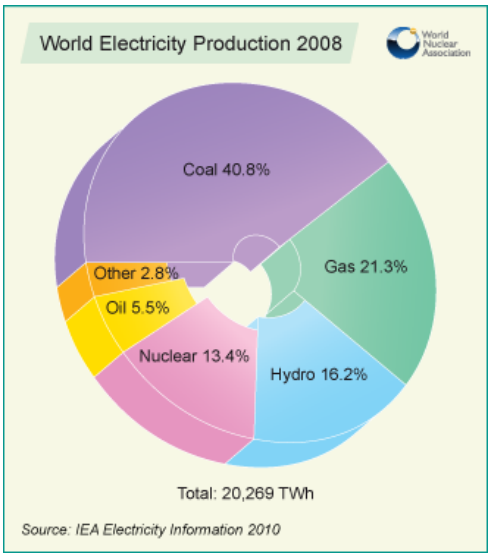

Figure 4: World electricity production in 2008. Nuclear contributions are equal to 13.4 % of the total production [WNA, 2014b].

Figure 5 shows the disparities of the nuclear electricity contribution among the countries. More precisely, it is depicted that France's nuclear share is by far the biggest one in the world, followed by Slovakia and Belgium. The International Atomic Energy Agency declares on their website that nuclear electricity contribution in France was equal to 73.28 % in 2013 for 58 operational nuclear reactors, which represents an electricity production of $403\,700\ GW.h$ [IAEA, 2015b]. As the context of this work takes place in France, the following sections focuses solely on this country.

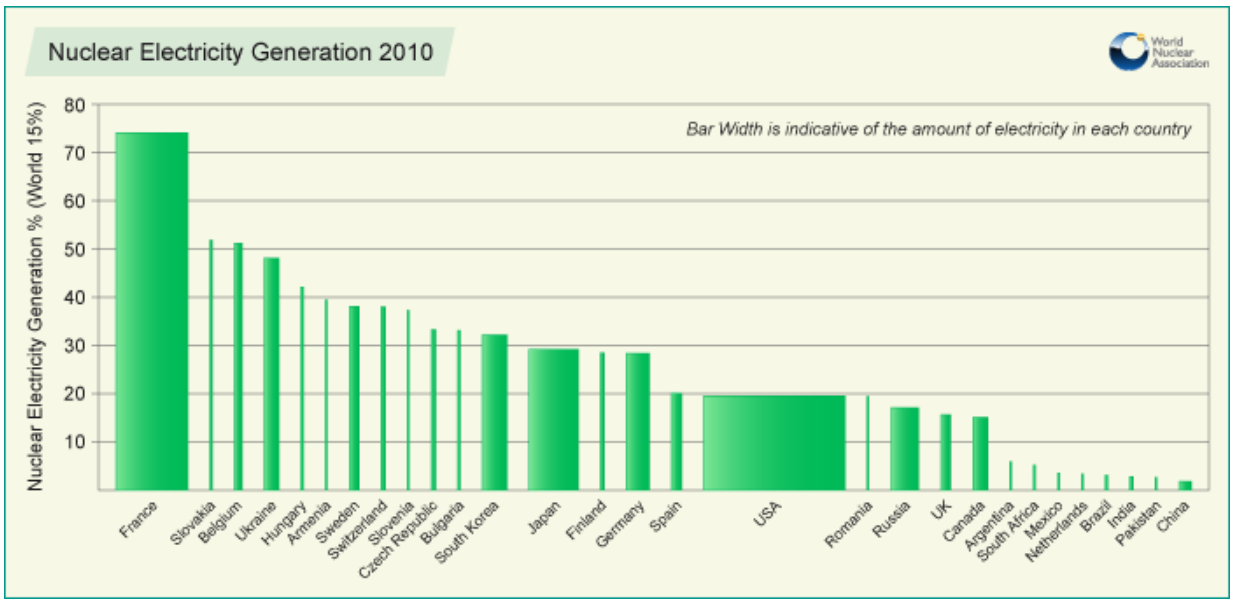

Figure 5: Nuclear electricity generation shares in each country in 2010 [WNA, 2014b].

2.2.3 Nuclear in France

The 58 nuclear reactors currently operating in France are all PWRs (which work as explained in section 2.2.2). These second generation reactors were designed by Areva, and can be classified into three groups: 900 MWe[2] (34), 1300 MWe (20) and 1450 MWe (4) reactors (Figure 6). Let us note that all first-generation reactors have been shut down several years ago and are being dismantled [Ministère de France, 2014].

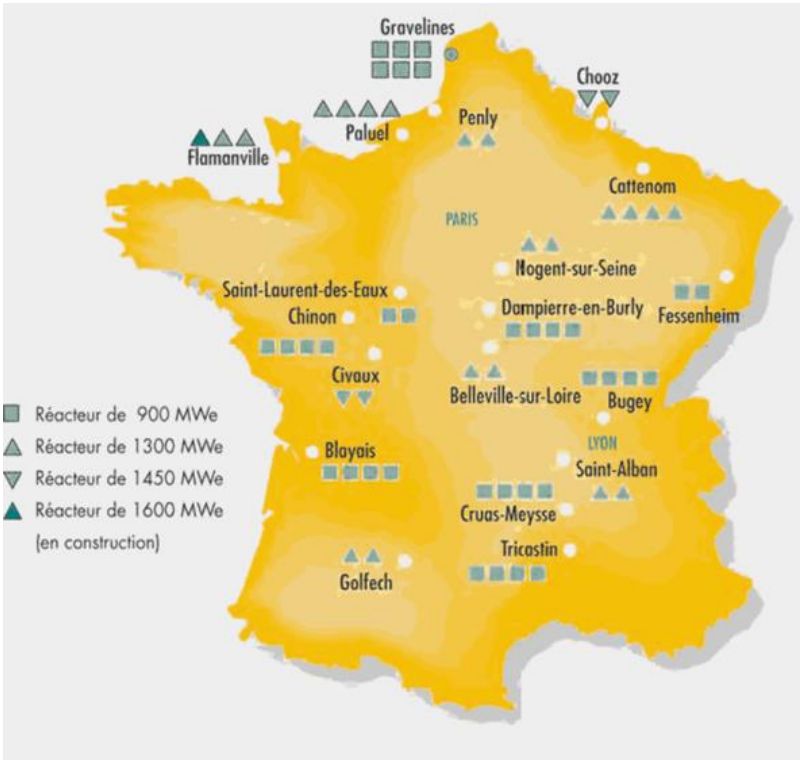

Figure 6: Map of Nuclear Reactors in France [Ministère de France, 2014].

In collaboration with Siemens (Germany), Areva developed the European Pressurised Water Reactor (EPR). The construction started in 2007 and its commercial operation is foreseen to 2017 [WNA, 2015b]. This model located in Flamanville will be the most powerful in the world (1600 MWe net), and is denominated as reactor of Generation III+, as it shall be put in place before the arrival of Generation IV reactors. Some major advantages on previous PWRs are smaller exploitation and maintenance costs, higher thermal efficiency, greater electricity production (with respect to the same quantity of uranium used), and safety measures against extreme events (flood, earthquake, plane crash…) [Areva, 2015a] [Areva, 2015b] [Areva, 2015c]. The investment costs are estimated at 8 billion euros [EDF, 2015].

There are no Category III reactors in France (e.g. Advanced PWR), but the government has planned to introduce reactors of Generation IV within a 30-year time frame. Although they are still in an experimental phase[3], they consist mainly in fast-neutron reactors (FNR) using sodium instead of water as neutron moderator and heat-transfer fluid [Ministère de France, 2014].

---

[2] *Megawatt electrical*

[3] *Experimental FNRs Rhapsodie, Phénix and Superphénix were put in place in the 1960s and 1970s, but were eventually shut down due to technical and political issues. [WNA, 2015b]. The construction of a new project called ASTRID (*Advanced Sodium Technological Reactor for Industrial Demonstration) has to be approved by 2019 *[CEA, 2014c]*.

Finally, let us remark that the Energy Transition bill introduced in October 2014 by Environmental Minister Ségolène Royal (under Holland's Presidency) aims at decreasing the nuclear share from 75 to 50% by 2025 [L'Express, 2014] [Le Monde, 2015].

2.2.4 Nuclear Fuel Cycle

Every year, France uses around 10 500 tonnes of uranium to generate electricity [WNA, 2015b]. The fuel used in reactors undergoes a series of steps, which are part of the nuclear fuel cycle. Figure 7 displays all the cycle stages, from the extraction until the disposal phase, with a possible reprocessing. This work takes part in the ultimate step of the nuclear fuel cycle: the nuclear wastes disposal.

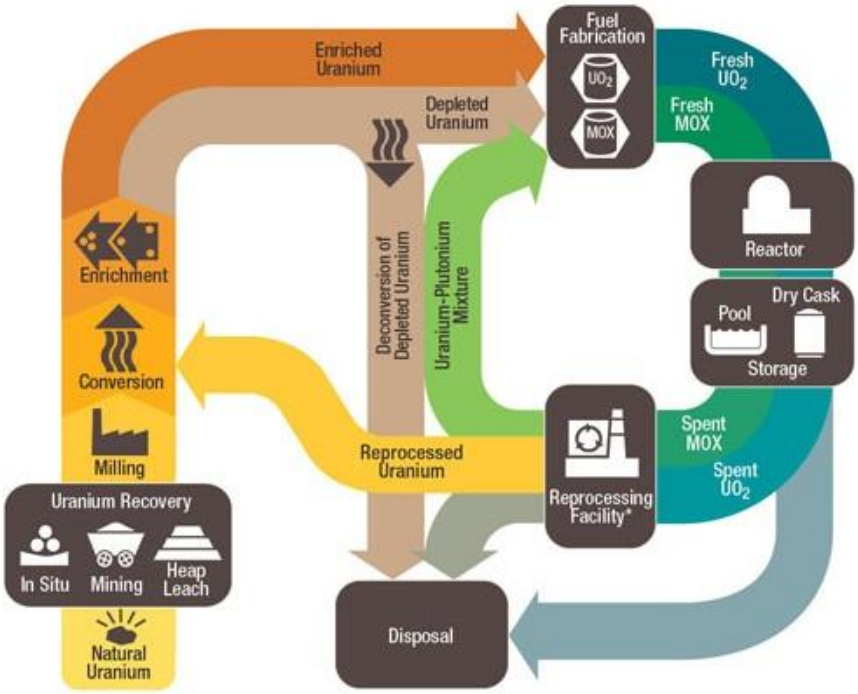

Figure 7: Sketch of the nuclear fuel cycle [USNRC, 2014].

According to the WNA, uranium is a "slightly radioactive metal" present in the Earth's crust. This resource is about 500 times more abundant than gold. However, only a number of areas around the world exhibit a concentration of uranium sufficiently high, such that extraction is economically feasible [WNA, 2014c]. The term "ore fields" will then be used to refer to these areas. Ore fields usually have a uranium content of 0.1 to 0.3 %, and it can go up until 20 % in exceptional cases (e.g. McArthur River, Canada) [SCF, 2015].

All the currently known recoverable resources of uranium account for 5.4 million of tonnes, from which more than half are found in Australia (31%), Kazakhstan (12%), Canada (9%) and Russia (9%) all together [WNA, 2012]. In 2013, France didn't produce any uranium [WNA, 2014d].

Uranium ores recovery can either be done using in situ techniques, excavation (underground or open pit) or heap leaching[4]. The material extracted is milled with sulphuric acid to get rid of waste rocks. The components produced are uranium oxide concentrates (U_3O_8), sometimes referred as "yellow cake" when dried. This product is not yet usable in most nuclear reactors (such as PWRs). The concentration of isotope 235 of uranium has to be increased, as enriched uranium is more inclined to undergo fission. This enrichment process is carried out by first transforming the yellow cake into gas (UF_6), then by separating by mass differentials (1%) between molecules of UF_6 containing the isotope 235 and the others. As a result, the concentration increases from 0.7 % in natural state, to an enriched $UF_6$with 3 to 5% of isotope 235. Finally, the product is sintered into pellets of uranium dioxide (UO_2) ready to be used in reactors.

In average, 1 tonne of natural uranium would produce *in fine* 44 $GW.h$. By comparison, it is equivalent to 20 000 tonnes of coal, or 8.5 million m³ of natural gas.

After 18 to 36 months inside the reactor, the used fuel is being discharged. It is then composed of about 96 % of uranium (with an isotope 235 content smaller than 1 %), 1 % of plutonium, and 3 % of waste products. There are two alternatives for the used fuel:

- **Reprocessing and Recycling:** Reprocessing the components consists in separating uranium and plutonium from waste products. Uranium and plutonium can be combined to form mixed oxide fuel (MOX) for instance, and be used anew. Recycling limits the waste quantities produced, and also decreases the radiotoxicity of the used fuel.
- **Long-term storage and final disposal:** The fuel is unloaded into a storage pond or into dry cask storage in order to absorb part of the heat emitted and allow the radiation levels to decrease. Wastes disposal depends on the level of state of radioactivity as well as their half-life [WNA, 2014c].

In 2011, 70% of EdF's[5] used fuel was in used fuel pools, mostly at La Hague, 19% was in dry casks and 11% had been reprocessed. Total storage accounted for 14,200 tonnes of wastes [WNA, 2015b]. The following section will focus on nuclear wastes management in France.

2.3 Nuclear Wastes Management

Nuclear wastes are radioactive. This means that they contain atoms called radionuclides which emit radiation, such as alpha particles, beta particles or gamma rays harmful to man and nature. It is therefore important to avoid any contact with the biosphere [ANDRA, 2009a].

Radioactivity can be measured through several units. The Becquerel (Bq) represents the activity (emission rate) of a nuclide. It is the number of radiation emitted per second. The nuclear energy deposited on the tissues (received dose) is quantified in Gray (Gy): $1\ Gy = 1\ J/kg$. Since identically received doses with different types of radiation do not have the same level of harmfulness, equivalent doses in Sievert (Sv) were defined. The international commission on radiological protection (ICRP) recommends a maximum annual dose of 1 mSv.

[4] Note: in situ leaching differs from heap leaching. The latter "places ore on a liner, then adds the chemicals via drip systems to the ore, whereas in situ mining lacks these liners and pulls pregnant solution up to obtain the minerals." [Wikipedia, 2015].

[5] Electricité de France

Although it might take thousands of years, the level of radioactivity does not remain the same. The half-life time is defined as the period after which the radioactivity is reduced by half, i.e. decrease of half of the number of radio-elements [COLLIN F. , 2015].

In France, the production of electricity is responsible for about 60 % of all the radioactive wastes produced in the country in 2010 (which is about 2 kg per inhabitant). A quarter stems from scientific researches, and the rest is generated by the military, industrial and medical sectors [ANDRA, 2012a]. Wastes treatment and disposal mainly depend on radioactivity, on half-life, but also on volume and content. Therefore, there is a need to establish a classification.

2.3.1 Waste classification

Waste classification differs from one country to another. In France, it is depicted by Figure 8. According to ANDRA, there were 1.32 million m³ of nuclear wastes in 2010. This volume shall increase of about 44% (1.90 million m³) by 2020 and 105 % (2.70 million m³) by 2030.

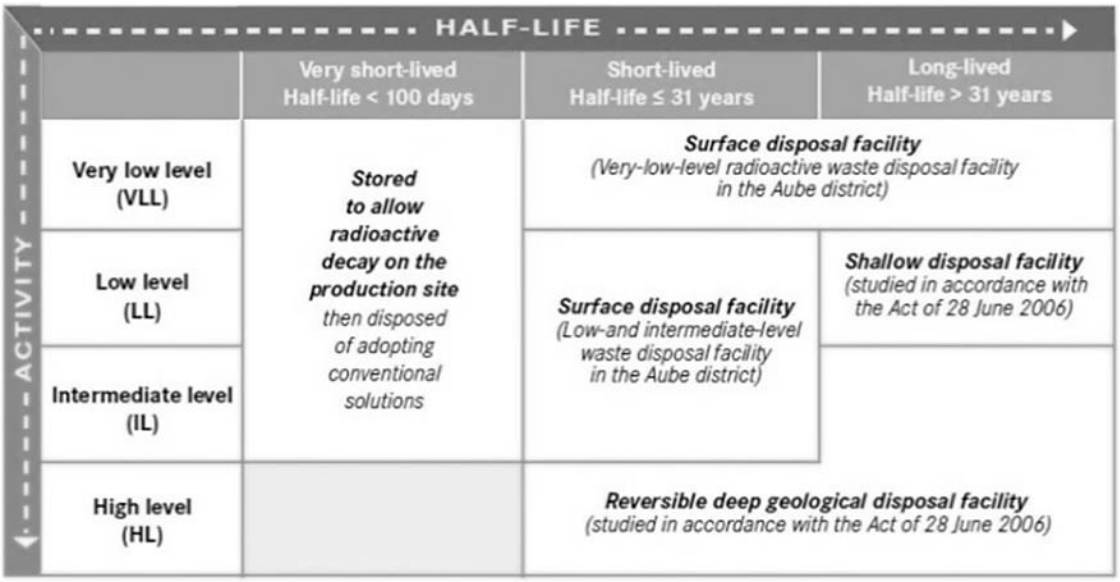

Figure 8: Classification of radioactive wastes in France [ANDRA, 2014a].

Wastes are classified into 6 categories:

- **Very-short-lived wastes (VSLW)**
- **Very-low-level wastes (VLLW)**
- **Low and intermediate level short-lived waste (LILW-SL)**
- **Low-level long-lived waste (LLW-LL)**
- **Intermediate-level long-lived waste (ILW-LL)**
- **High-level waste (HLW)**

Figure 8 also describes the way these wastes are handled in France. The key idea is to isolate them from the biosphere to let radioactive decay occur without affecting living organisms.

More specifically, deep geological storage has been selected as potential solution for the Intermediate-level long-lived (ILW-LL) and the high-level (HLW) wastes. The former mainly consists in metallic structures surrounding spent fuels (hulls). They are compacted into pucks and put into metal packages, which are in turn placed (by group of 4) into a concrete container (Figure 9). On the other hand, HLW consist mainly in non-reusable residues following the recycling process. They are calcined into powder and incorporated into molten glass (Weight ratio HLW/glass = 11/400). Lastly, the whole mixture is poured into stainless steel containers (Figure 10).

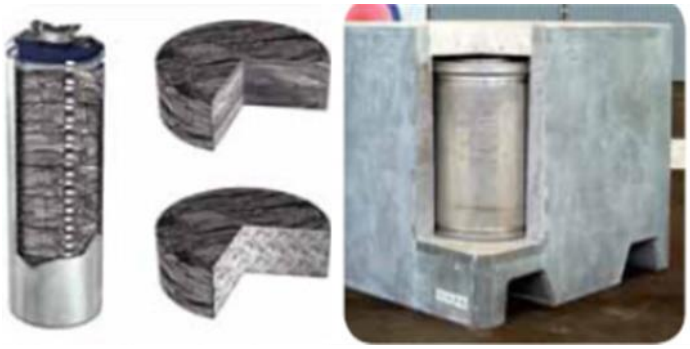

Figure 9: Metal package containing pucks of ILW-LL (left) which is in turn placed into a concrete container (right). [ANDRA, 2009b]

Figure 10: Stainless steel container of vitrified HLW. [ANDRA, 2009c]

The following sections focus on these two types of wastes. ANDRA also names them B and C wastes, respectively for ILW-LL and HLW [ANDRA, 2005]. Table 1 displays the distribution of the radioactive wastes produced in France at the end of 2010. It shows that less than 5 % of the total wastes volume accounts for almost all the wastes in terms of level of radioactivity.

	HLW	ILW-LL	Others
Distribution of the level of radioactivity (end of 2010)	96 %	4 %	< 0.05%
Distribution of the volume of radioactive wastes (end of 2010)	0.2 %	3 %	96.8%

Table 1: Distribution of level of radioactivity and volume of radioactive wastes produced in France at the end of 2010. The values were taken from [ANDRA, 2012b].

Figure 11: Storage centres (pink) and main repository sites (green) in France. HLW and ILW-LL repository is taken care of at La Hague, Marcoule, and Cadarache. [ANDRA, 2012c]

2.3.2 Underground Research facilities in France and Europe

In France, there are numerous facilities that discard these wastes (Figure 11). As of now, regarding deep geological storage of HLW and ILW-LL, the sites dealing with their repository are located at past (La Hague) and current production sites (Marcoule, and Cadarache) [ANDRA, 2009b], [ANDRA, 2009c].

Yet, the feasibility of such task is still under study. In Europe, the investigations are conducted in underground research facilities (Figure 12). Some of them were built as an extension of a mine gallery or an existing tunnel (e.g. Mont Terri and Grimsel, Switzerland), while others are solely dedicated to deep geological storage research (e.g. Mol in Belgium, Onkalo in Finland) [EURIDICE, 2015].

Figure 12: Map of the underground research facilities in Europe. In parentheses the type of rock in which the laboratory was built ("Klei", "Graniet", and "Zout" stand for respectively Clay, Granite and Salt). [EURIDICE, 2015]

In the frame of these research programs, France has selected two sites (Figure 12). The first site located in Tournemire investigates the potential risks related to deep geological storage. In other words, the laboratory researches where and how to bury those wastes [LADEPECHE, 2008]. The site of Bure studies the feasibility of deep geological storage in a layer located in the Meuse/Haute-Marne region. The characteristics of the rock formation will be developed in Section 2.4.

Unlike the second site, Tournemire's facility (which was an old railway tunnel beforehand) is only dedicated to research, notably because of the presence of a fault and underground running waters [LADEPECHE, 2008]. However, as the site of Tournemire (supervised by IRSN[6]) has similar properties to the host formation of Bure, the experiments are conducted as expertise for the potential storage in the Meuse/Haute-Marne region [LE FIGARO, 2013].

.

6 Institut de radioprotection et de sûreté nucléaire

2.3.3 Role of ANDRA

ANDRA (Agence Nationale pour la gestion des Déchets Radioactifs) is a public institution in France which is in charge of the management of the totality of the radioactive waste products on the long term. It runs scientific research programs that study the storage possibilities of high-level wastes (HLW, or type C), as well as long-lived intermediate-level wastes (ILW-LL, or type B).

More precisely, the agency has been entrusted in 1991 the conception of a safe and reversible disposal system: the Cigéo[7] project. For this purpose, two geological media have been considered: granite and clay. Although ANDRA does not have an underground laboratory for granite, it receives contributions from foreign laboratories (such as Sweden and Switzerland). On the other hand, the underground laboratory in Meuse/Haute Marne has been created to assess the feasibility of deep geological storage in the Callovo-Oxfordian formation [ANDRA, 2005].

2.4 The Meuse/Haute-Marne site: Callovo-Oxfordian formation

2.4.1 General features

The laboratory is located about 200 km to the East of Paris (Figure 13). The geological domain consists in a succession of horizontal layers of limestone, marls and clay from the Mesozoic[8] and Cenozoic eras (Figure 16). The Callovo-Oxfordian argillite is an indurated clay formation of at least 130 m thick, dated to 155 million years and located at a depth of between 400 and 600 metres (Figure 14).

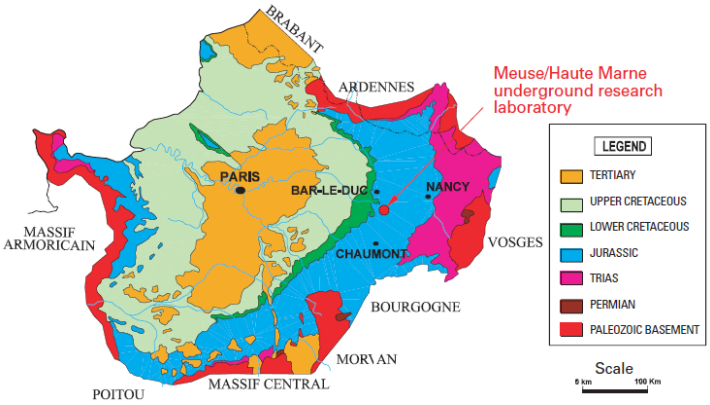

Figure 13: Position of the Meuse/Haute Marne underground laboratory [ANDRA, 2005]

The mineralogy arrangement of the argillite influences its properties as a rock. The material is composed of clay minerals, carbonates and quartz. Indeed, the first component confers retention properties while the large amount of carbonates (25% in volume) makes the medium chemically stable. Regarding quartz, the material is well known for its good mechanical properties and its high thermal conductivity.

[7] *Centre Industriel de stockage Géologique*
[8] *The Mesozoic era contains the Triassic, Jurassic and Cretaceous periods.*

In addition to these requirements, other main assets that led to considering the Callovo-Oxfordian argillite as a potential solution for deep geological storage are a stable geological environment (against seismicity and erosion) without the presence of exploitable natural resources and most of all the homogeneity and regularity of such formation over a considerable surface. The next section gives more details about the underground research laboratory that was installed on this site.

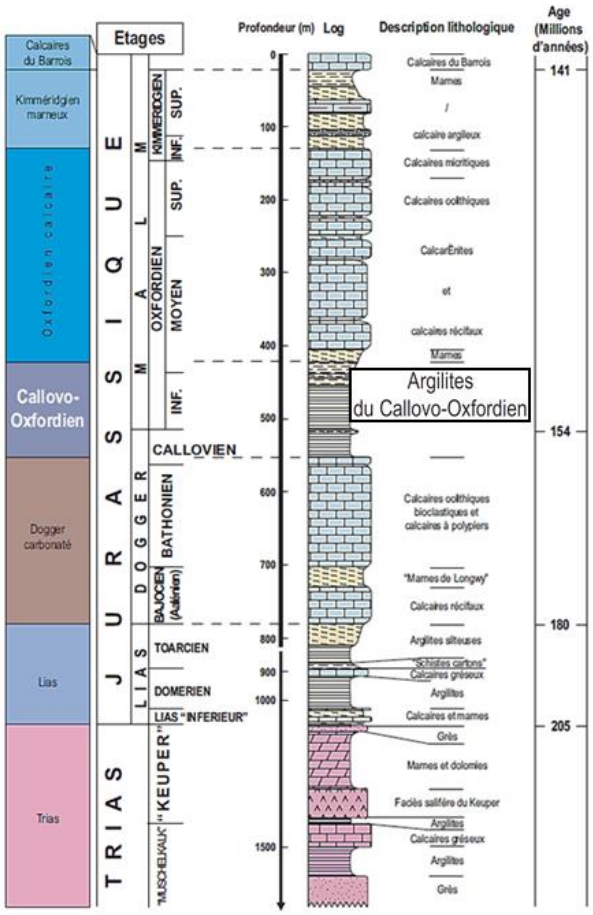

Figure 14: Geological cross-section at the Meuse/Haute-Marne Laboratory site. [ANDRA, 2005]

2.4.2 The Underground Research Facility at Bure

As part of their studies on the feasibility of a deep geological storage in the Callovo-Oxfordian argillite, ANDRA installed an underground laboratory located at Bure (Figure 13). The facility has developed a network of galleries to conduct series of experiments (Figure 15) which cover several aspects, such as the thermal behaviour of the host formation following the heat emitted from the waste packages, the diffusion and retention properties of radioactive elements, or the mechanical behaviour subsequent to the excavation process [ANDRA, 2014b].

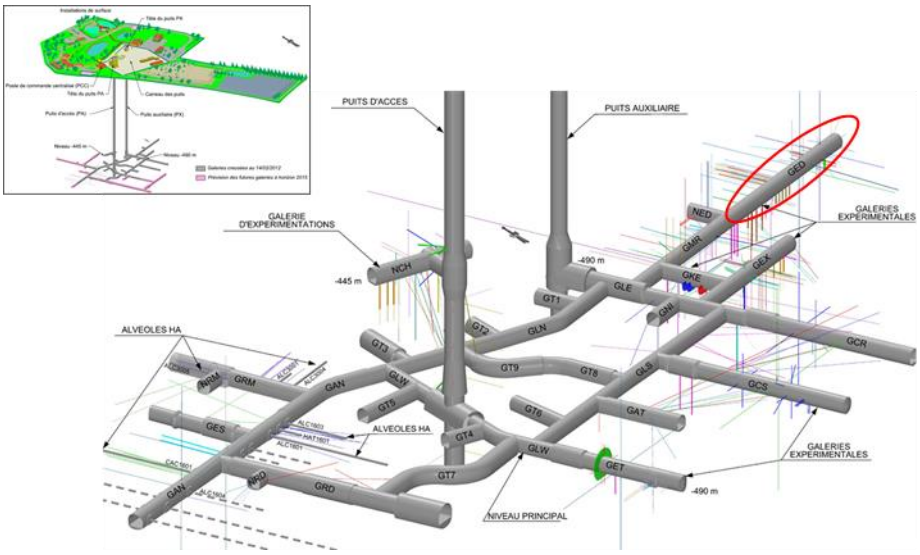

Figure 15: Experimental galleries network of the underground facility. The GED Gallery is circled in red [ANDRA, 2014b]

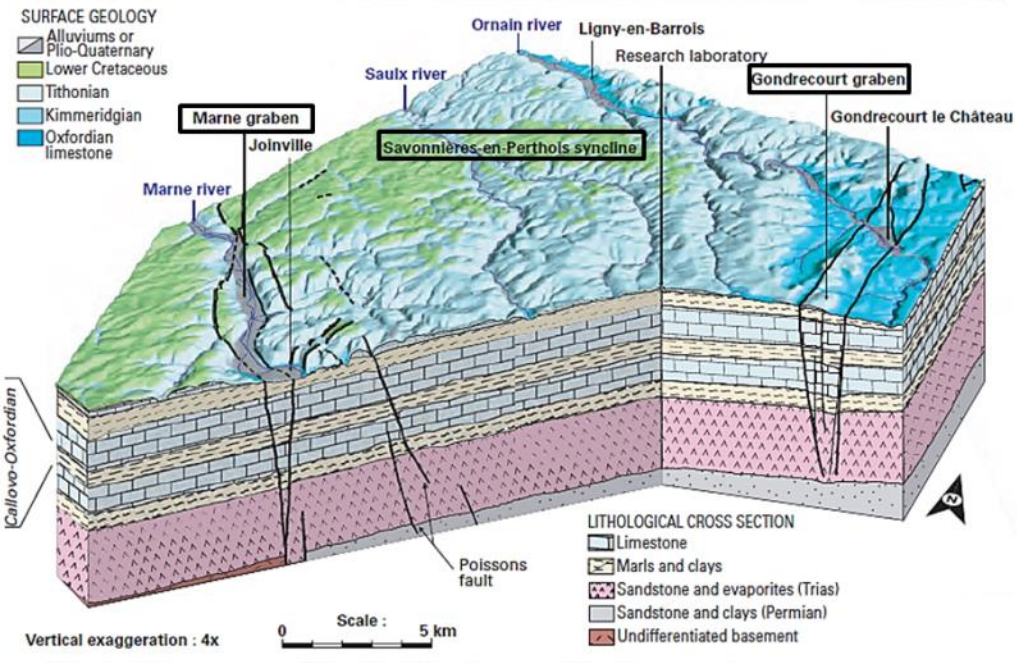

Figure 16: 3D block diagram of the Meuse/Haute-Marne sector. [ANDRA, 2005]

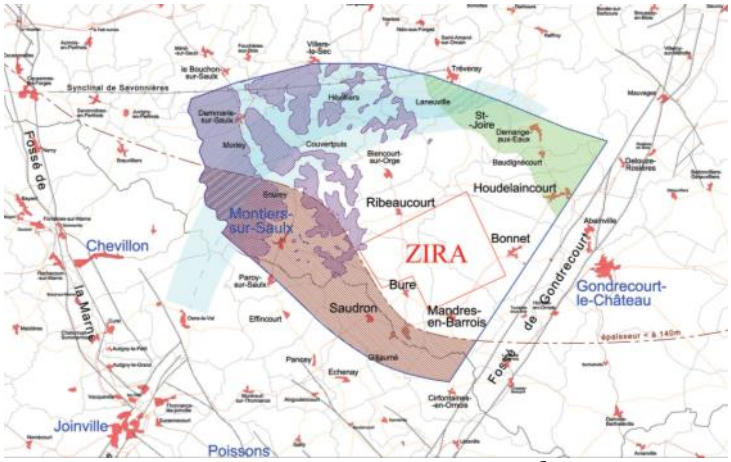

Figure 17: Map of the Transposition Zone of 250 km² determined in 2005 (blue), and of ZIRA of 30 km² determined in 2009 (red). [ANDRA, 2012d]

2.4.3 Meuse/Haute-Marne site: Zone of Investigation

As mentioned here above, the Meuse/Haute-Marne site contains a quite homogenous and regular layer of argillite. Detailed investigations conducted in the underground laboratory can be extended to a 250 km² zone. Figure 16 shows that the research area is bounded by:

- The Gondrecourt graben in the South-East;
- The Marne graben in the South-West;
- The Savonnières-en-Perthois syncline to the North (i.e. presence of dipping layers).

As a result, the agency defined that area of 250 km² as the Transposition Zone in 2005. It is an area in which the rock properties are similar to the ones of the rock in the vicinity of the underground laboratory. Moreover, in 2009, ANDRA defined a zone of 30 km² in which more elaborate researches on the implantation of underground installations are conducted: ZIRA[9] (Figure 17). It is in that zone that the storage might potentially take place [ANDRA, 2012d].

The following section describes the underground installations of the Cigéo project conceived by ANDRA.

2.4.4 Future repository installations imagined by ANDRA

The Cigéo project has the mission to design a safe and reversible disposal system for nuclear wastes (types B and C). Such centre has to guarantee its functioning for at least a century. It is located at a depth of around $-490\,m$, right in the middle of the Callovo-Oxfordian argillite layer (Figure 14).

Figure 18 gives an overview of the architecture of the installations. There are two surface installations which are used for, among other things, the reception of the waste packages and their preparation for the transfer at $-490\,m$ of depth. The underground gallery network is endowed with 4 vertical shafts[10] and 2 ramps[11]. The shafts connect the surface to the underground structure, and can be sorted according to their function, i.e. waste package transfer (1), personnel, materials and heavy equipment transfer (2), and ventilation purposes (1). The use of access ramps in parallel has been considered because unlike shafts, they do not depend on a unique equipment with high cost of maintenance and are flexible in terms of operations (no throughput interruption) [ANDRA, 2005].

The repository zones are separated from each other according to the type of wastes they are containing (type B or C). They are linked to the shafts by means of access drifts (Figure 19). These drifts can also be sorted according to their function (package transfer, ventilation…).

In the repository zone containing B wastes, the disposal cells consist in sub-horizontal tunnels. Each of them has a maximum diameter of 12 m and is 270 m long. The disposal packages in concrete (cf. section 2.3.1) can weigh up to 25 tonnes and their dimensions vary between 1.20 to 3 m. They are stacked on several levels all along the tunnels (Figure 20). Once a tunnel is filled, it is sealed, notably by the use of swelling clay and concrete (Figure 22). The footprint of the B waste repository zone would be around 1 km².

[9] *Zone d'Intérêt pour la Reconnaissance Approfondie*
[10] *Puits d'accès de stockage (Figure 18).*
[11] *Descenderies d'accès de stockage (Figure 18).*

Regarding C waste repository zone, the disposal cells are dead-end horizontal tunnels (diameter of 0.7 m and 40 m long). Each stainless steel package (cf. section 2.3.1) is enveloped with an additional container made of non-alloyed steel, and the whole weighs up to 2 tonnes, with a diameter and a length which can goes up to 0.65 m and 1.60 m respectively (Figure 21). Similarly to the B waste cell, the sealing is also realised by means of swelling clay and concrete (Figure 23). The footprint is about 5 km². The final procedure of the storage is to seal all the access galleries and shafts.

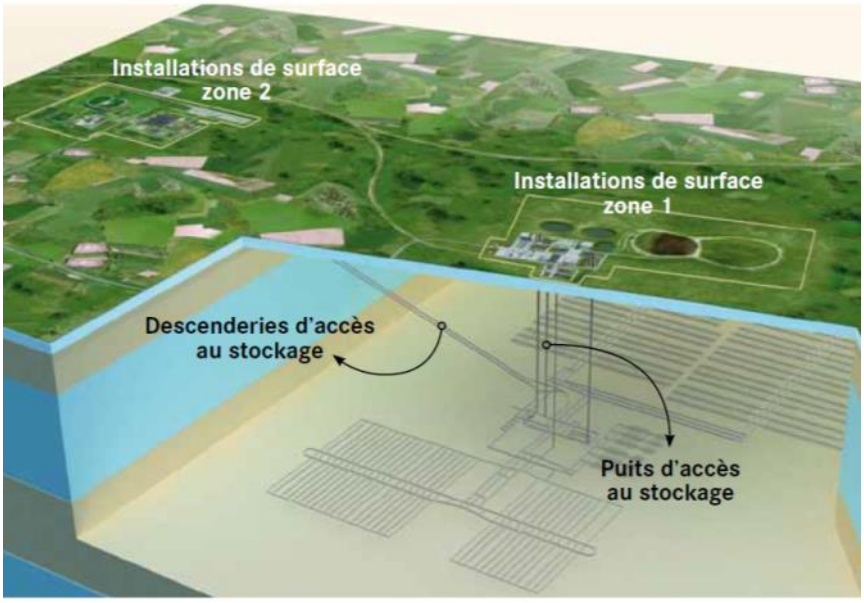

Figure 18: Sketch of the installations of Cigéo. [ANDRA, 2012b]

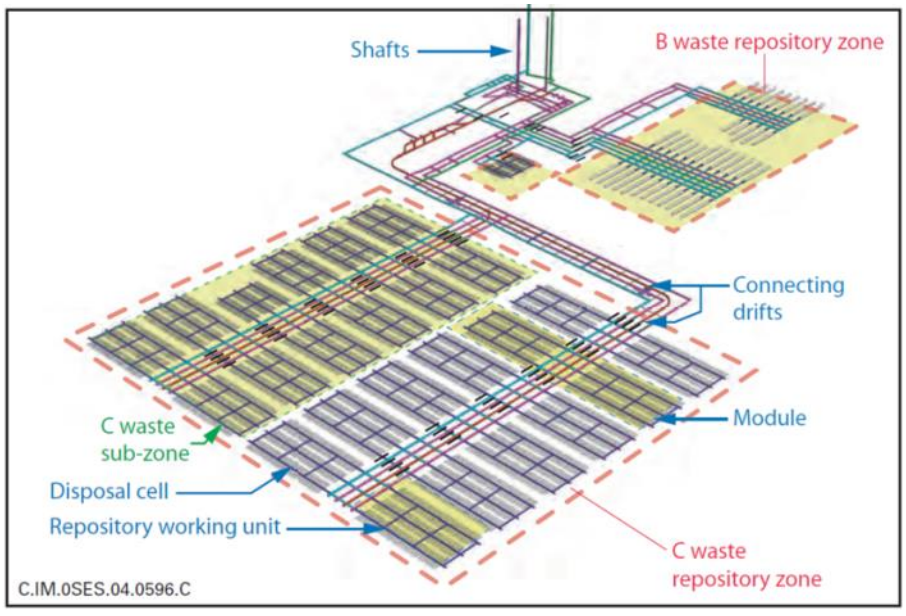

Figure 19: General layout of the repository. [ANDRA, 2005]

Lastly, let us remark that the area devoted to C waste storage can be halved if the pre-disposal storage period is doubled. In that case, the temperature of the containers would be much lower. Consequently, there would be no need for spacing buffers, which are originally used for a thermal decoupling effect, i.e. limiting the heat released by the packages (Figure 21). Further information about the underground installations and the execution processes are available at [ANDRA, 2005].

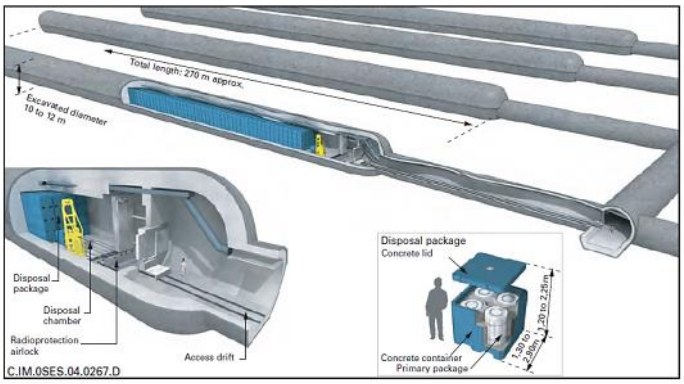

Figure 20: B waste disposal cell while in operation. [ANDRA, 2005]

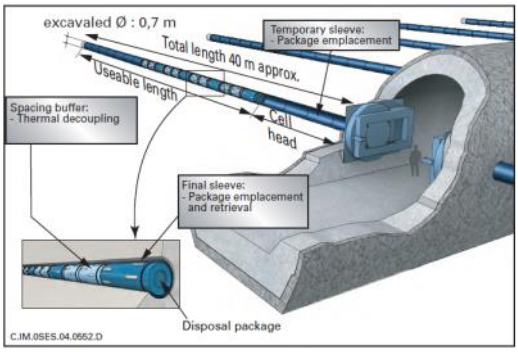

Figure 21: C waste disposal cell while in operating configuration. [ANDRA, 2005]

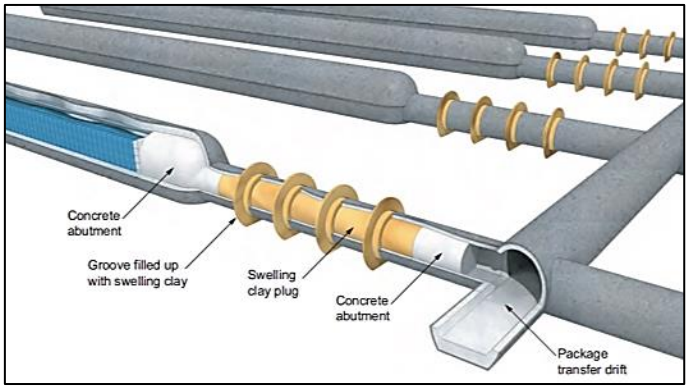

Figure 22: B waste disposal cell after sealing. [ANDRA, 2005]

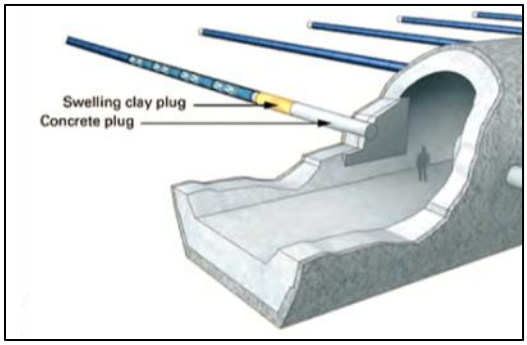

Figure 23: C waste disposal cell after sealing. [ANDRA, 2005]

2.5 Description of the SDZ experiment

ANDRA conducts series of experiments in the Underground Research Laboratory (URL) of Bure in order to study the feasibility of a deep geological storage (Figure 18). The experiment treated in this work is called the Saturation Damaged Zone experiment (SDZ). It investigates the evolution of the Excavated Damaged Zone (EDZ) through a ventilation test. The aim is to reproduce the exploitation phase that follows the excavation. This test is performed in the GED[12] gallery (Figure 15), and induces a desaturation (and possible resaturation) of the host formation (Callovo-Oxfordian argillite) [CHARLIER, et al., 2013a].

2.5.1 Excavated Damaged Zone

The excavation process leads to a change in the stress field within the rock formation. The radial stresses decrease as the orthoradial stresses increase (cf. section 5.1.3B). The resulting damage is linked to several factors, such as the in situ stress and the rock resistance. In the URL of Bure, the drilling of the experimental galleries at $-490\ m$ has created a fractures

[12] Galerie Expérimentale Deux

network. These fractures can be divided into two categories: shear and tensile fractures. The fractured zone is called the Excavated Damaged Zone [BOSSART, et al., 2002] and [GUILLON, 2011].

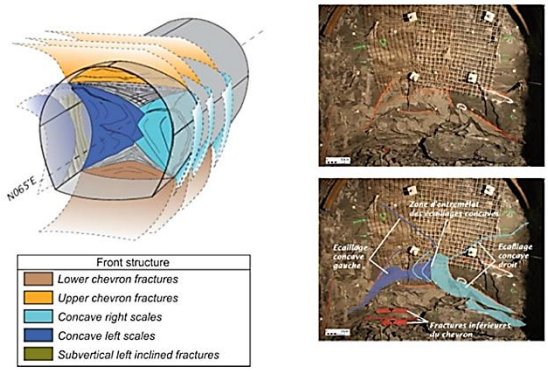

Figure 24: Fractures at the front of the GED gallery: sketch (left) and photos (right). [ARMAND, et al., 2014], [CRUCHAUDET, et al., 2010b]

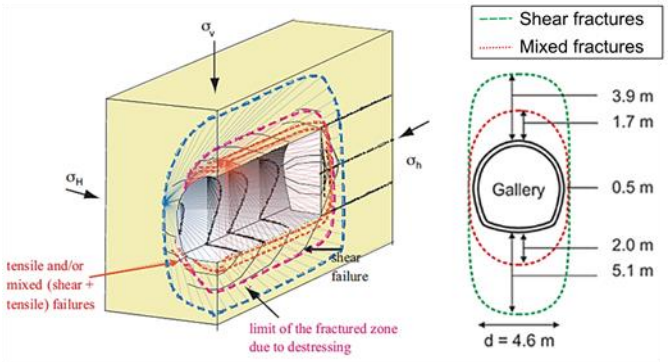

Figure 25: Representation of the damaged zones around the GED gallery. [BOURDEAU, et al., 2007], [ARMAND, et al., 2014]

The GED gallery is oriented along the minor horizontal principal stress σ_h (Figure 25). Chevron fractures (i.e. shear type) were detected at the excavation front of this gallery (Figure 24). Furthermore, the extension of the damaged zone can be decomposed into two sub-zones: an inner zone close to the gallery that has both types of fracture (i.e. mixed fractures) and an outer zone surrounding the first one with only shear fractures. The extension of such zones is quantified on Figure 25 [BOURDEAU, et al., 2007] , [CRUCHAUDET, et al., 2010b] and [ARMAND, et al., 2014].

The concept of EDZ suggests that the rock properties are altered. Indeed, the fractures allow a preferential flow path within the medium, which increases the permeability[13] of the material in that zone. The ventilation might intensify the effects of the EDZ on the mechanical and hydraulic properties of the host formation. Therefore, quantifying the impacts allows a better understanding of the state of the wastes cells at the end of their exploitation phase.

2.5.2 Objectives

The SDZ experiment is aimed to reproduce the impact of the excavation and exploitation phases on the rock formation. Furthermore, the objectives are:

- Evaluation of saturation, pressure and permeability profiles in the argillite (damaged and undamaged zones);
- Characterise the EDZ and its evolution around the gallery during the controlled ventilation;
- Characterise the mechanical evolution (convergence, strains…) of the gallery during desaturation-resaturation cycles.

Before describing the modelling, the principles of the experiment are explained.

[13] *The notion of permeability is linked to the scale at which the material is analysed. Here, the rock is considered to be homogeneous, the property is thus inherent to the material.*

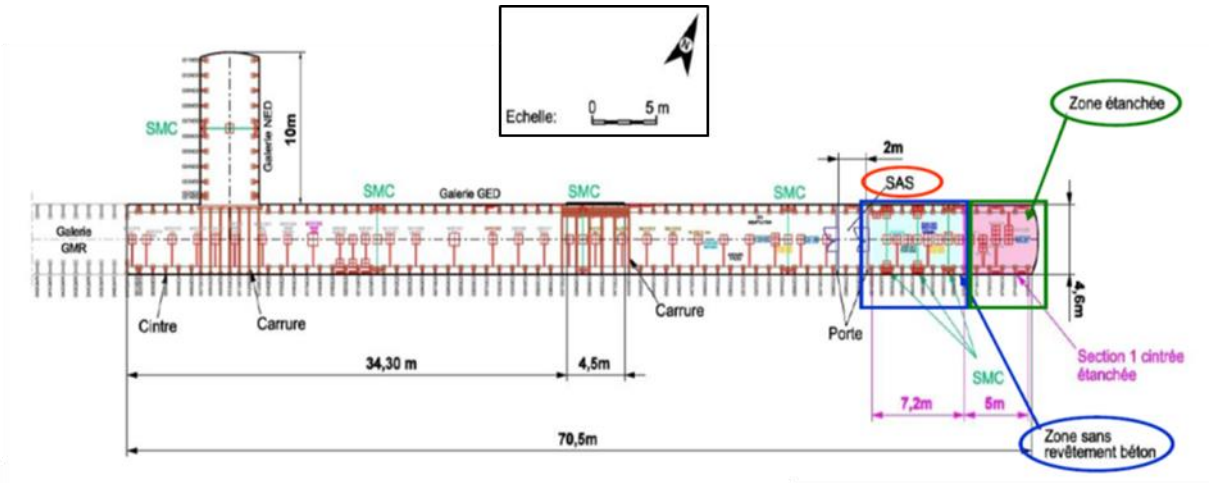

Figure 26: Situation of the SDZ experiment in the GED gallery. [CRUCHAUDET, et al., 2010a]

2.5.3 Ventilation Test and Measures

A. Ventilation Mechanism

The SDZ experiment is realised at the end of the GED gallery. The test zone (Figure 26) is composed of an airlock of 2 m long (for insulation), a first test zone of 7.2 m (bare wall), and a second test zone of 5 m staunched by means of a geotextile and a thermowelded plastic membrane. Figure 27 shows a typical section of the SDZ zone.

The ventilation system takes the air from the GED gallery and treats it. The air inlet is pre-heated and humidified, then cooled down until it reaches its dew point[14]. After that, it is heated and humidified again until the wanted temperature and relative humidity. It is blown towards the end of the gallery. Lastly, the air outlet is also treated. The condensed water is continuously weighted in order to establish water mass balances.

Several sensors measuring climatic, hydraulic or mechanical properties are installed in the test zone in order to evaluate the repercussions of the ventilation on the argillite.

B. Climatic and hydraulic Measures

The climatic measures refer to the temperature and hygrometric data's, whereas the hydraulic ones to the water pressure and the water content. The uncoated test zone (i.e. the first 7.2 m) is dedicated to taking these measures. It is coloured in green on Figure 28. The climatic measures are taken in sections 4, 6, 8 and 10, and the hydraulic ones in sections 5 and 6. Appendices 8.1 to 8.3 give more details on the position of the sections, the position of the sensors, as well as the time evolution of the measures.

C. Mechanical Measures

They consist mainly in displacements measures. These displacements can correspond to the convergence of the gallery or to the cracks openings. This work focuses on the first type of displacements. Sections 4, 7 and 10 on Figure 28 use convergence measuring devices and section 8 uses extensometers to monitor the displacement of the rock formation. Appendices 8.4 and 8.5 give more details on the position of the sections, the position of the sensors, as well as the time evolution of the measures.

---

14 Lowest temperature (for given pressure and humidity) at which a sample of air is saturated (equilibrium between evaporation and condensation rates).

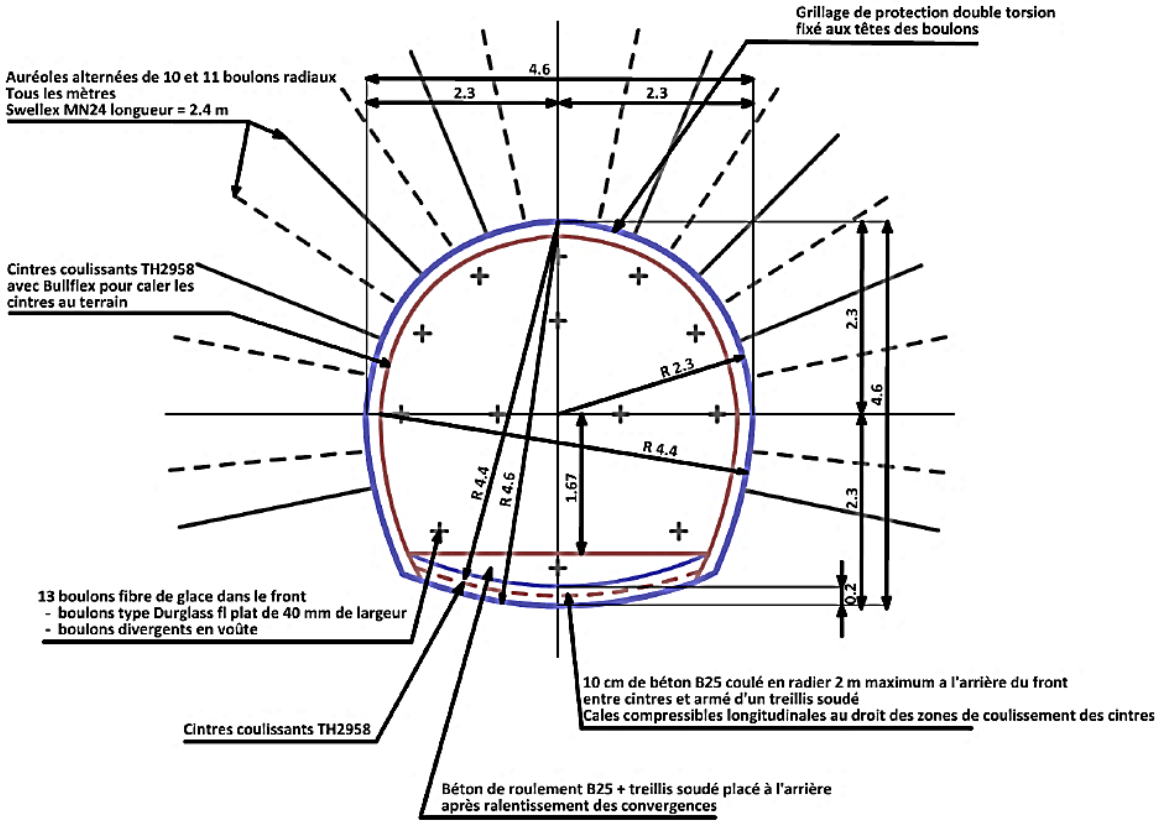

Figure 27: Sketch of a typical section of the SDZ gallery. [CRUCHAUDET, et al., 2010a]

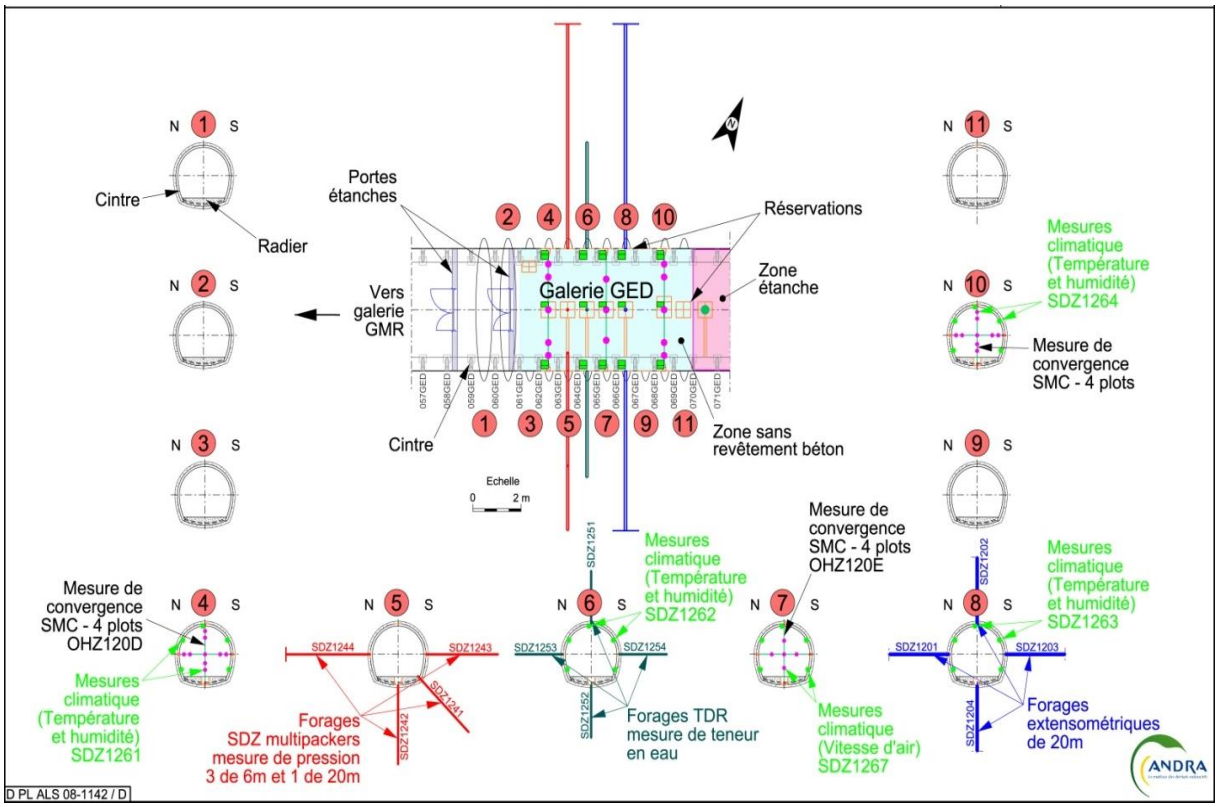

Figure 28: Localisation of the measures in the SDZ zone. [CRUCHAUDET, et al., 2010a]

2.6 Contributions of the Work

In order to characterise the structure and the size of the EDZ, a correct numerical model is needed. This work investigates the subject considering the excavation phase prior to the ventilation test. Its particularity is to propose laws of behaviour that modify the hydraulic parameters on the basis of the mechanical variables. More specifically, the work seeks to correlate the evolution of the intrinsic permeability of the medium with a variable that quantifies the rock damage. Consequently, the hydraulic behaviour of the medium evolves in the same way regardless of the orientation.

For this purpose, the chapter dedicated to the modelling is divided into 3 parts. The first one is devoted to describing the evolution of the permeability and leads to the determination of a numerical model that provides a good correspondence with the experimental measurements. The second part analyses the several impacts of the ventilation test itself, such as the desaturation, the drop of water pressure and the convergence of the rock formation. Lastly, the third part introduces the concept of anisotropy of the mechanical parameters and interprets the resulting effects.

2.7 Conclusion

When producing electricity, nuclear energy plays an important role in our modern societies: more than 13 % of the world electricity production comes from nuclear sources. This share rises up to 75 % in France. With its 58 nuclear reactors among the 439 operational around the world, it is the country the most dependent on nuclear electricity. Following the recent event of Fukushima in 2011, several countries have decided to gradually part ways with the nuclear option, while others decided to maintain their energy policy.

The nuclear wastes can be extremely harmful to man and nature, in such a way that it is crucial to isolate them. Deep geological storage was selected as a potential solution for the most critical wastes: intermediate-level long-lived (ILW-LL) and high-level (HLW) wastes. Yet, the feasibility of such task is still under study. In France, ANDRA runs scientific research programs that investigate the storage possibilities in the Callovo-Oxfordian argillite, located at a depth between 400 and 600 m in the Meuse/Haute-Marne region.

An underground research laboratory (URL) was installed in the rock formation. It carries out series of experiments to study the thermal, hydraulic and mechanical behaviours of the rock formation following the disposal phase (excavation, wastes storage and sealing). Among these, the Saturation Damaged Zone (SDZ) experiment investigates the impact of the exploitation phase in the argillite through saturation/desaturation cycles (i.e. ventilation test). In particular, the excavation damaged zone (EDZ) and its evolution has to be characterised.

In this context, one of the main contributions of this work is to propose laws of behaviour that modify the hydraulic parameters on the basis of the mechanical variables, such that the hydraulic behaviour of the medium evolves in the same way regardless of the orientation.

Modelling such aspects requires a mathematical model which considers the physical phenomena occurring within the rock. Therefore, the next chapter is dedicated to explaining the main concepts and theories that describe its behaviour.

3 Mathematical Model

During the excavation phase, the redistribution of the stresses around the gallery might damage the rock mass. Subsequently, the mechanical behaviour of the rock influences its hydraulic properties. For instance, volumetric deformations modify the porosity, and thus the quantity of water stored in the porous structure.

In addition to that, during the digging and the exploitation of these galleries, the rock wall becomes progressively unsaturated. This may lead to physical alterations such as shrinkage and fissuring. As a consequence, all these events create a zone with modified transfer properties and disturbed water flows: the *Excavated Damaged Zone* (EDZ).

The mathematical model representing these phenomena is based on the concept of an isotherm medium saturated by two immiscible fluids: water and air. This part first describes the hydraulic model. Then, it focuses on the hydromechanical couplings before detailing the mechanical model. Lastly, the concept of water-vapour exchanges at the gallery wall is introduced.

3.1 Hydraulic Model

In the scope of the modelling, a soil sample is considered as "partially saturated" when the porous spaces are not all filled with water. This misuse of language means that a certain quantity of air is also present among the sample.

The hydraulic model is based on biphasic transfers. On one hand, we have a liquid phase composed of liquid water and dissolved air. On the other hand, the gas phase consists in dry air and water vapour (Figure 29).

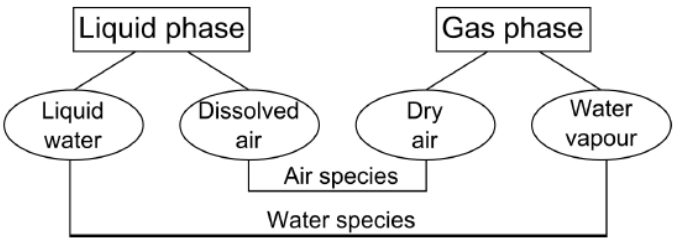

Figure 29: Definition of the phases and components. [COLLIN F. , 2015]

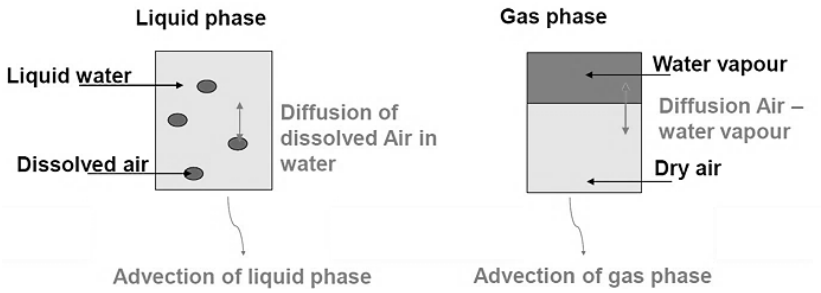

Figure 30: Description of the phenomena occurring within an isothermal medium saturated by two immiscible fluids. [COLLIN F. , 2015]

In a partially saturated soil sample, several phenomena occur (Figure 30):

- Advection of liquid phase (liquid water and dissolved air);
- Advection of gas phase (water vapour and dry air);
- Diffusion of dissolved air in liquid water (in liquid phase);
- Diffusion dry air – water vapour (in gas phase).

Before developing the flow phenomena, some hydraulic properties need to be defined first.

3.1.1 Main Hydraulic Properties

A. Capillarity

The presence of two immiscible fluids (gas and liquid) leads to the notions of fluid interface and therefore of surface tensions σ_{GL}. These tensions result from the equilibrium of the forces between the fluids within the interface. They take part in the capillarity phenomenon, which is governed by Jurin's law. This law is depicted through Jurin's experiment (Figure 31). The concept of surface tensions explains the rise and fall of a liquid within a thin capillary tube. In other words, Jurin's law expresses the vertical equilibrium, which gives the height h of the water column inside a tube of radius r.

$$p_c = p_G - p_L = \rho_w . g . h = \frac{2\,\sigma_{GL}\cos\theta}{r} \qquad \textbf{(2)}$$

With p_c the capillary pressure (or suction), p_G the pressure of the gaseous phase, p_L the pressure of the liquid phase, ρ_w the water density, g the gravity acceleration, θ the contact angle, r_c the capillary tube radius, and σ_{GL} the superficial tension between the gaseous and liquid phases. [Miny, 2013]

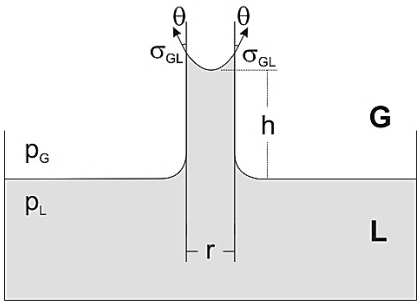

Figure 31: Capillarity Phenomenon depicted through a sketch of Jurin's Experiment. [GERARD, 2011]

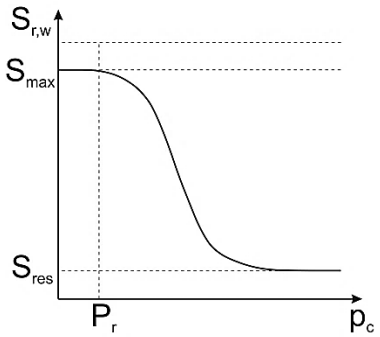

Figure 32: Model of Retention Curve given by Van Genuchten. [DIEUDONNE, 2011]

B. Retention Curve

The retention curve of a porous material consists in the evolution of water saturation $S_{r,w}$ with respect to the capillary pressure p_c within the material. This pressure is derived from Kelvin's law, which links it to the relative humidity H_r (Equation 3). This law suggests an equilibrium between the liquid water and water vapour within porous media.

$$H_r = \frac{p^g_{H_2O}}{p^g_{H_2O,0}} = \exp\left(\frac{-p_c . M_{H_2O}}{\rho_w . R . T}\right) \qquad \textbf{(3)}$$

With $p_{H_2O}^g$ the vapour pressure within the gaseous phase, $p_{H_2O,0}^g$ the saturated vapour pressure, $M_{H_2O} = 0.018\ [kg.mol^{-1}]$ the molar mass of water, $R = 8.314\ [J.mol^{-1}.°K^{-1}]$ the ideal gas constant, and $T\ [°K]$ the temperature. Therefore, every gaseous component of the mixture behaves like an ideal gas.

Once the capillary pressure p_c is calculated, the water saturation of the medium $S_{r,w}$ is obtained according to the model of Van Genuchten:

$$S_{r,w} = S_{res} + \frac{S_{max} - S_{res}}{\left[1 + \left(\frac{p_c}{P_r}\right)^n\right]^m} \quad \textbf{(4)}$$

With $p_c = p_g - p_w$, S_{max} the maximal saturation degree, S_{res} the residual saturation degree, n and m the coefficients of Van Genuchten's law, such as $m = 1 - 1/n$, and P_r the air entry value. These parameters account for the shape of the curve displayed at Figure 32.

Lastly, using the hypothesis of a medium saturated by two immiscible fluids, the air saturation $S_{r,a}$ is simply given by Equation 5:

$$S_{r,a} = 1 - S_{r,w} \quad \textbf{(5)}$$

3.1.2 Transfer Equations of the Fluids

A. Advection of Liquid Phase

Let us neglect the effect of dissolved air in liquid phase on the properties of the liquid water – dissolved air mixture. Therefore, the advection of the mixture is defined as the advection of water among the porous medium (Darcy's law):

$$\underline{q_l} = -\frac{k_{int}\ .\ k_{r,w}(S_{r,w})}{\mu_w}\left(\underline{\nabla}\mathrm{p_w} + \rho_w g\ \underline{\nabla} y\right) \quad \textbf{(6)}$$

With k_{int} the intrinsic permeability, $k_{r,w}$ the water relative permeability, $S_{r,w}$ the water saturation, μ_w the dynamic viscosity of water, ρ_w the water density, g the gravity acceleration, and y the vertical coordinate.

When the medium becomes partially saturated, Darcy's law remain valid, as long as the relative permeability $k_{r,w}$ changes as well. It is commonly expressed using Van Genuchten's model:

$$k_{r,w} = \sqrt{S_{r,w}}\left[1 - \left[1 - \left(S_{r,w}\right)^{\frac{1}{m}}\right]^m\right]^2 \quad \textbf{(7)}$$

With m being the parameter of the retention curve.

Let us note that water is considered to be compressible. Thus it behaves according to the following law:

$$\rho_w = \rho_{w,0}.\left[1 + \frac{p_w - p_{w,0}}{\chi_w}\right] \quad \textbf{(8)}$$

With $\rho_{w,0}$ the water density at the reference pressure $p_{w,0}$, and χ_w the water compressibility.

B. Advection of Gaseous Phase

The equation of the advection of the gaseous phase is similar to the one of the liquid phase. In this case, Darcy's law (Equation 6) is adapted by considering the gas parameters.

$$\underline{q_g} = -\frac{k_{int}.k_{r,g}(S_{r,g})}{\mu_g}\left(\underline{\nabla}\mathrm{p_g} + \rho_g g\,\underline{\nabla}z\right) \qquad \textbf{(9)}$$

With $k_{r,g}$ the gas relative permeability, $S_{r,g}$ the gas saturation, μ_g the dynamic viscosity, and ρ_g the density of the gaseous phase.

In the scope of the modelling, the effect of gravity is not taken into consideration. Moreover, a constant gas pressure has been considered (cf. section 5). Indeed, the possible variations of gas pressure are not significant (no gas injection and moderated changes in temperature). As a result, the overall contribution of the advection of the gaseous phase can be neglected.

C. Diffusion of Dissolved Air in Liquid Water

The diffusion of dissolved air in liquid water can be quantified using the air concentration gradient within the liquid mixture. This phenomenon is depicted by the diffusive flow of dissolved air $\underline{i}_{(Air)_d}$ though Fick's law:

$$\underline{i}_{(Air)_d} = -\rho_w.S_{r,w}.\varphi.\tau.\mathrm{D}^w_{\mathrm{Air}}.\,\underline{\nabla}\left(\frac{\rho^w_{Air}}{\rho_w}\right) \qquad \textbf{(10)}$$

With φ and τ respectively the porosity and the tortuosity of the soil sample, $\mathrm{D}^w_{\mathrm{Air}}$ the diffusion coefficient of the dissolved air in liquid water, and ρ^w_{Air} the relative density of dissolved air. Tortuosity is defined as the ratio between the distance between two points on a straight line, and the real distance a fluid particle would take to travel from one end to another. This parameter thus depicts the easiness/difficulty with which a molecule diffuses within the porous medium.

The relative density of dissolved air ρ^w_{Air} can be obtained from Henry's law:

$$\rho^w_{Air} = H_{Air}(T).\rho^g_{Air} \qquad \textbf{(11)}$$

With H_{Air} the constant of Henry which depends on the composition of the gas and on the temperature T $[°K]$, and ρ^g_{Air} the relative density of dry air.

D. Diffusion Dry Air – Water Vapour

Concerning the gaseous phase, both dry air and water vapour are able to diffuse within the mixture. The diffusive flow of one component is equal and of opposite sign to the other one. This type of diffusion is also governed by Fick's law:

$$\underline{i}_{(Air)_g} = -\rho_g.(1-S_{r,w}).\varphi.\tau.\mathrm{D}^{Vapour}_{\mathrm{Air}}.\,\underline{\nabla}\left(\frac{\rho^g_{Air}}{\rho_g}\right) = -\underline{i}_{(H_2O)_g} \qquad \textbf{(12)}$$

With $\mathrm{D}^{Vapour}_{\mathrm{Air}}$ the diffusion coefficient of the mixture *dry air – water vapour*.

3.1.3 Fluid Mass Balance Equations

After having defined the several phenomena considered in a model of biphasic transfers, a mass balance equation can be established for each chemical constituent.

A. Mass Balance of Water

Water can be found either in a liquid state, either as vapour. The mass balance equation of water is expressed as follows:

$$\dot{S}_{(H_2O)_l} + div\left(\underline{f}_{(H_2O)_l}\right) + \dot{E}_{H_2O}^{l\to g} = Q_{(H_2O)_l} \quad \textbf{(13)}$$

$$\dot{S}_{(H_2O)_g} + div\left(\underline{f}_{(H_2O)_g}\right) - \dot{E}_{H_2O}^{l\to g} = Q_{(H_2O)_g} \quad \textbf{(14)}$$

With $\dot{S}_{(H_2O)_l}$ the storage term of liquid water, $\underline{f}_{(H_2O)_l}$ the mass flow of liquid water, $\dot{E}_{H_2O}^{l\to g}$ the evaporation mass rate, and $Q_{(H_2O)_l}$ the production or consumption of liquid water (respectively for water vapour).

The advection of the gaseous phase and the diffusion of dissolved air within liquid water are both neglected. As a result, the mass flow term of liquid water $\underline{f}_{(H_2O)_l}$ expresses solely the advection of the liquid phase, whereas the one linked to water vapour $\underline{f}_{(H_2O)_g}$ only takes into account the diffusion of water within the gaseous mixture.

$$\underline{f}_{(H_2O)_l} = \rho_w . \underline{q}_l \quad \textbf{(15)}$$

$$\underline{f}_{(H_2O)_g} = \underline{i}_{(H_2O)_g} \quad \textbf{(16)}$$

With $\underline{q}_l$ the liquid phase flow, and $\underline{i}_{(H_2O)_g}$ the diffusive water vapour flow.

Equation 13 and Equation 14 can be grouped together, such that the evaporation mass terms $\dot{E}_{H_2O}^{l\to g}$ cancel each other. Using Equation 15 and Equation 16, the mass balance of water can be written as:

$$\frac{\partial}{\partial t}\left(\rho_w . \varphi . S_{r,w} + \rho_{H_2O}^{g} . \varphi . S_{r,g}\right) + div\left(\rho_w . \underline{q}_l\right) + div\left(\underline{i}_{(H_2O)_g}\right) - Q_{H_2O} = 0 \quad \textbf{(17)}$$

With Q_{H_2O} the total production or consumption of the water component.

B. Mass Balance of Air

Air can be found either in a gaseous state, either as dissolved air. The mass balance equation of air is expressed as followed:

$$\dot{S}_{(Air)_g} + div\left(\underline{f}_{(Air)_g}\right) + \dot{E}_{Air}^{g\to d} = Q_{(Air)_g} \quad \textbf{(18)}$$

$$\dot{S}_{(Air)_d} + div\left(\underline{f}_{(Air)_d}\right) - \dot{E}_{Air}^{g\to d} = Q_{(Air)_d} \quad \textbf{(19)}$$

With $\dot{S}_{(Air)_g}$ the storage term of dry air, $\underline{f}_{(Air)_g}$ the mass flow of dry air, $\dot{E}_{Air}^{g\to d}$ the dissolution mass rate, and $Q_{(Air)_g}$ the production or consumption of dry air (respectively for dissolved air).

The advection of the gaseous phase is neglected. As a result, the mass flow term of dry air $\underline{f}_{(Air)_g}$ expresses solely the diffusion of air within the gaseous mixture, whereas the one

linked to dissolved air $\underline{f}_{(Air)_d}$ takes into account both the advection of the liquid phase and the diffusion of air within the liquid phase.

$$\underline{f}_{(Air)_g} = \underline{i}_{(Air)_g} \quad (20)$$

$$\underline{f}_{(Air)_d} = \rho^w_{Air}.\underline{q}_l + \underline{i}_{(Air)_d} \quad (21)$$

With $\underline{q}_l$ the liquid phase flow, $\underline{i}_{(Air)_d}$/ $\underline{i}_{(Air)_g}$ the diffusive dissolved air/dry air flow. The expression of ρ^d_{Air} is given by Henry's law (Equation 11).

Equation 18 and Equation 19 can be grouped together, such that the dissolution mass terms $\dot{E}^{g\to d}_{Air}$ get cancelled. Using Equation 20 and Equation 21, the mass balance of air can be written as:

$$\frac{\partial}{\partial t}\left(\rho^g_{Air}.\varphi.S_{r,g} + \rho^d_{Air}.\varphi.S_{r,w}\right) + div\left(\underline{i}_{(Air)_g}\right) + div\left(\rho^g_{Air}.H_{Air}.\underline{q}_l + \underline{i}_{(Air)_d}\right) - Q_{Air} = 0 \quad (22)$$

With Q_{Air} the total production or consumption of the air component.

3.2 Hydromechanical Couplings

The hydromechanical couplings express the effect of the mechanical contributions on the hydraulic model, and vice versa. Concerning the developed model, the couplings are noticeable on three aspects: the notion of effective stresses, the solid density of the medium and in Darcy's law. As for now, this section develops the first two concepts.

3.2.1 Notion of Effective Stresses

In saturated conditions, the mechanical behaviour is influenced by the presence of the fluid. This phenomenon is described by Terzaghi's definition of effective stress:

$$\sigma_{ij} = \sigma'_{ij} + p_w\,\delta_{ij} \quad (23)$$

With σ_{ij} the total stress tensor, σ'_{ij} the effective stress tensor, p_w water pressure, and δ_{ij} Kronecker's delta. Equation 23 assumes a punctual contact between the grains. Nevertheless, for more coherent rocks, Terzaghi's principle is not valid anymore. Taking into account the compressibility of the solid particles, Bishop proposed an alternative definition for a partially saturated porous medium:

$$\sigma_{ij} = \sigma'_{ij} + b_{ij}.\left(p_w.S_{r,w} + p_g.S_{r,g}\right).\delta_{ij} \quad (24)$$

With σ_{ij} and σ'_{ij} respectively Bishop's total and effective stress tensor, and b_{ij} Biot's tensor, which translates the proportion of the surface particle subjected to the fluid pressure. For isotropic materials, the tensor can be reduced to a scalar b, such as:

$$b = 1 - \frac{K}{K_s} \quad (25)$$

With $K = \frac{E}{3\,(1-2\nu)}$ the bulk modulus of the poroelastic material and K_s the bulk modulus of the solid phase only (i.e. grain compressibility).

3.2.2 Solid Density Variation

The deformability of the solid grains is taken into consideration through Coussy's expression of the porosity variation [COUSSY, 2004]:

$$\dot{\varphi} = (b - \varphi).\left(\dot{\varepsilon}_v + \frac{S_{r,w}.\dot{p}_w + S_{r,g}.\dot{p}_g}{K_s}\right) \quad \textbf{(26)}$$

With $\dot{\varepsilon}_v$ the volumetric deformation rate of the porous skeleton. Let us note that Equation 26 is used in the storage term $\dot{S}$, which intervenes in the fluid mass balance equations (Equation 17 and Equation 22).

3.3 Mechanical Model

The mechanical behaviour depicts the relation between stress and strain rates. Three fundamental types of models can be distinguished:

- Elasticity: the stress state at a given time depends only on the strain at the same moment;
- Plasticity: the stress state takes into account the (loading) history of the material;
- Viscosity: the strains are related to the loading rate.

This section concentrates on an isotropic material, which means that its properties are the same in every direction. A linear elastic model is first introduced. It is then followed by an elastoplastic model with an internal friction law.

3.3.1 Linear Elastic Model

The linear elastic model is governed by Hooke's law (Equation 27). When a certain amount of stress σ is applied to a linear elastic material, it undergoes a certain quantity of deformation ε, in a proportional way. Moreover, the lateral strains ε_{lat} induced by σ are proportional to ε.

$$\sigma = E\varepsilon \quad \textbf{(27)}$$

$$\varepsilon_{lat} = -\nu\varepsilon = -\nu\frac{\sigma}{E} \quad \textbf{(28)}$$

With E the Young modulus and ν Poisson'ratio. In addition to using the notion of effective stress, Equation 27 can be expressed with tensors:

$$\sigma'_{ij} = C_{ijkl} \,.\, \varepsilon_{kl} \quad \textbf{(29)}$$

$$\varepsilon_{kl} = D_{ijkl} \,.\, \sigma'_{ij} \quad \textbf{(30)}$$

For an isotropic material, the stiffness tensor C_{ijkl} and the compliance tensor D_{ijkl} are given by Equation 31 and Equation 32 respectively (with $D_{ijkl} = [C_{ijkl}]^{-1}$).

$$C_{ijkl} = \frac{E}{(1+\nu)(1+2\nu)} \cdot \begin{bmatrix} 1-\nu & \nu & \nu & 0 & 0 & 0 \\ \nu & 1-\nu & \nu & 0 & 0 & 0 \\ \nu & \nu & 1-\nu & 0 & 0 & 0 \\ 0 & 0 & 0 & 1-2\nu & 0 & 0 \\ 0 & 0 & 0 & 0 & 1-2\nu & 0 \\ 0 & 0 & 0 & 0 & 0 & 1-2\nu \end{bmatrix} \quad \textbf{(31)}$$

$$D_{ijkl} = \frac{1}{E} \cdot \begin{bmatrix} 1 & -\nu & -\nu & 0 & 0 & 0 \\ -\nu & 1 & -\nu & 0 & 0 & 0 \\ -\nu & -\nu & 1 & 0 & 0 & 0 \\ 0 & 0 & 0 & 1+\nu & 0 & 0 \\ 0 & 0 & 0 & 0 & 1+\nu & 0 \\ 0 & 0 & 0 & 0 & 0 & 1+\nu \end{bmatrix} \quad \textbf{(32)}$$

3.3.2 Elastoplastic Model with Internal Friction Law

For low values of stresses and strains, the material has an elastic behaviour. When they increase until a point where the yielding limit is reached, the material enters the plasticity phase. While the elastic behaviour can be modelled as a spring, the rheological model of a perfect plasticity is assimilated to a sliding frictional element. The behaviour of an elastoplastic material can be represented in Figure 33.

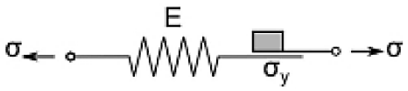

Figure 33: Rheological model of an elastoplastic material [COLLIN F. , 2014]

Regarding elastoplasticity, the strain rate $\dot{\varepsilon}_{ij}$ can be decomposed into an elastic component $\dot{\varepsilon}_{ij}^{e}$ and a plastic component $\dot{\varepsilon}_{ij}^{p}$:

$$\dot{\varepsilon}_{ij} = \dot{\varepsilon}_{ij}^{e} + \dot{\varepsilon}_{ij}^{p} \qquad \textbf{(33)}$$

Using Equation 30, the elastic strain rate can be written as:

$$\dot{\varepsilon}_{ij}^{e} = D_{ijkl}.\dot{\sigma}'_{kl} \qquad \textbf{(34)}$$

The Drücker-Prager criterion is often used to depict the mechanical behaviour of the material, notably concerning the entrance in plasticity. Let us define the I_σ the first stress invariant, and $II_{\hat{\sigma}}$ the second deviatoric stress invariant:

$$I_\sigma = \sigma_{ij}\,\delta_{ij} = \sigma_{ii}$$

$$II_{\hat{\sigma}} = \sqrt{\frac{1}{2}\,\hat{\sigma}_{ij}\,\hat{\sigma}_{ij}} \quad with\ \hat{\sigma}_{ij} = \sigma_{ij} - \frac{I_\sigma}{3}\delta_{ij}$$

The Drücker-Prager criterion is

$$f \equiv II_{\hat{\sigma}} + m.\left(I_\sigma - \frac{3c}{\tan\phi}\right) = 0 \qquad \textbf{(35)}$$

With m which is written as followed:

$$m = \frac{2\sin\phi}{\sqrt{3}\,(3-\sin\phi)}$$

Furthermore let us consider the deviatoric stress q and the mean stress p, which are expressed using to the first two invariants:

$$q = \frac{II_{\hat{\sigma}}}{\sqrt{2}}$$

$$p = \frac{I_\sigma}{3}$$

In the reference frame of principal stresses, the limit between the elastic and plastic domain is defined by a surface (Figure 34). In the $p-q$ axes, the Drücker-Prager criterion [BARNICHON, 1998] is simply a line of slope M (Figure 35). Equation 35 becomes:

$$f = q + M.\left(p - \frac{c}{\tan\phi}\right) = 0 \qquad \textbf{(36)}$$

With $M = \frac{6\sin\phi}{3-\sin\phi}$.

While the elastic parameters (for an isotropic material) are the Young Modulus E and Poisson's ratio ν, the criterion takes into account the cohesion c and the internal friction angle ϕ of the material. Their analytical expression can be derived from Equation 36. Their values will be drawn from the calibration of the triaxial tests (cf. section 4.2.2).

$$c = q|_{p=0} \cdot \frac{\tan(\phi)}{M} \quad (37)$$

$$\phi = \arcsin\left(\frac{3M}{6+M}\right) \quad (38)$$

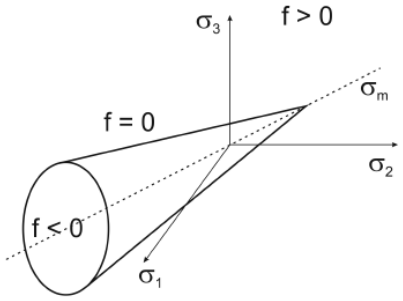

Figure 34: Yield surface according to Drücker-Prager. [CHARLIER, 2000]

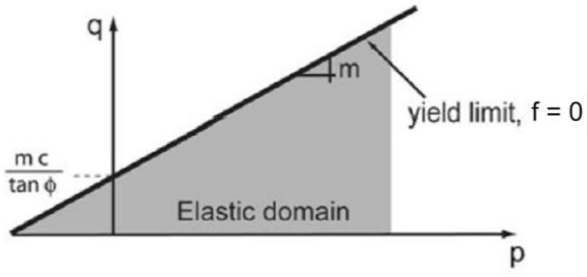

Figure 35: Yield limit according to Drücker-Prager. [FRANCOIS, et al., 2012]

The plastic strain rate $\dot{\varepsilon}_{ij}^{p}$ from Equation 33 has the following expression:

$$\dot{\varepsilon}_{ij}^{p} = \lambda^{p} . \frac{\partial g}{\partial \sigma'_{ij}} \quad (39)$$

With λ^{p} a plastic multiplier which is determined through the consistency condition. The stress state has to stay on the surface plasticity f as long as the yielding limit is reached: $\dot{f} = 0$ (Figure 34).

Concerning the plastic flow potential g, it represents a non-associated plasticity of the material. This means that the plastic volumetric strains depend on the dilatancy angle ψ. From an analytical point of view, this means that

$$g \equiv II_{\hat{\sigma}} + m' . \left(I_{\sigma} - \frac{3c}{\tan\phi}\right) = 0 \quad (40)$$

With $m' = \frac{2\sin\psi}{\sqrt{3}\,(3-\sin\psi)}$. If $\psi = 0°$, the volumetric strains are constant during the plastic phase.

The model allows the hardening/softening of the plastic parameters ϕ and/or c (Figure 36), as function of the Von Mises equivalent plastic strain

$$\hat{\varepsilon}_{eq}^{p} = \sqrt{\frac{2}{3}\,\hat{\varepsilon}_{ij}^{p}\hat{\varepsilon}_{ij}^{p}}$$

The phenomenon is described through a hyperbolic function (Figure 37). The internal friction angle ϕ varies in the following conditions:

$$if\ \hat{\varepsilon}_{eq}^{p} < \delta_p : \phi = \phi_0 \quad (41)$$

$$if\ \hat{\varepsilon}_{eq}^{p} \geq \delta_p : \phi = \phi_0 + \frac{(\phi_f - \phi_0).(\hat{\varepsilon}_{eq}^{p} - \delta_p)}{B_p + (\hat{\varepsilon}_{eq}^{p} - \delta_p)} \quad (42)$$

With ϕ_0 and ϕ_f respectively the initial and final internal friction angle, B_p the value of equivalent plastic strain for which half of the hardening/softening is achieved, and $\delta_p$the delay after which the phenomenon starts. Figure 37 displays the evolution of ϕ with respect to $\hat{\varepsilon}_{eq}^{p}$ during hardening. Regarding the variation of cohesion c, the mathematical expression is similar to Equation 41 and Equation 42.

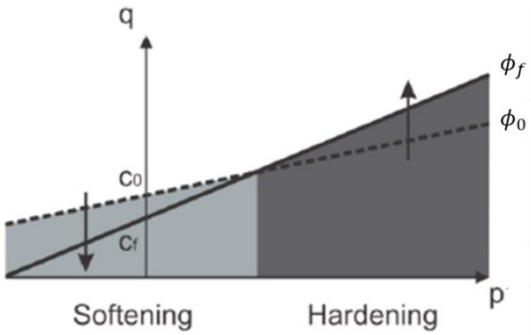

Figure 36: Hardening and softening effects of the Drücker-Prager model: yield surface. [PARDOEN, et al., 2014]

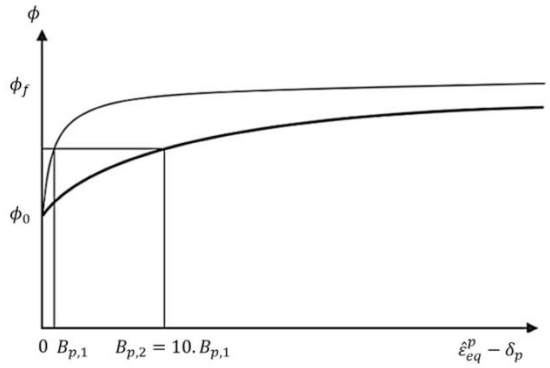

Figure 37: Hardening effect of the internal friction angle ϕ: Hyperbolic relation for two values of B_p. *[PARDOEN, et al., 2014]*

3.4 Water and Vapour Exchanges at Rock Wall

In this section, the concept of a non-classical hydraulic boundary condition is introduced in order to describe the water exchanges between the humid air in the gallery and the rock wall [GERARD, et al., 2008]. The total water flow $\bar{q}$ in the boundary layer is composed of a seepage flow $\bar{S}$ and a vapour exchanges flow $\bar{E}$ (Figure 38):

$$\bar{q} = \bar{S} + \bar{E} \quad (43)$$

The seepage flow contribution $\bar{S}$ is a unilateral condition which occurs when the pore water pressure in the rock formation p_w^f is greater than both the cavity air pressure p_w^{cav} and the atmospheric pressure p_{atm}. If $p_w^{cav} = p_{atm}$, water flows take place at the same moment.

$$\bar{S} = K_{pen}.\left(p_w^f - p_{atm}\right)^2 \quad if\ p_w^f \geq p_w^{cav}\ and\ p_w^f \geq p_{atm} \quad (44)$$

$$\bar{S} = 0 \quad if\ p_w^f < p_w^{cav}\ \ or\ \ p_w^f < p_{atm} \quad (45)$$

With K_{pen} a penalty coefficient for numerical convergence.

The vapour exchanges $\bar{E}$ are expressed by the difference between the vapour densities of the air in the gallery and of the air contained in the boundary layer of the rock formation (resp. ρ_v^{cav} and ρ_v^f):

$$\bar{E} = \alpha_0.(\rho_v^f - \rho_v^{cav}) \quad (46)$$

With α the mass transfer coefficient which is determined through drying tests [GERARD, et al., 2010]. However, in this work, a default value of α_0 will be taken from the literature. The coefficient will then be calibrated in accordance to the experimental results [CHARLIER, et al., 2013a]. [CHARLIER, et al., 2013b].

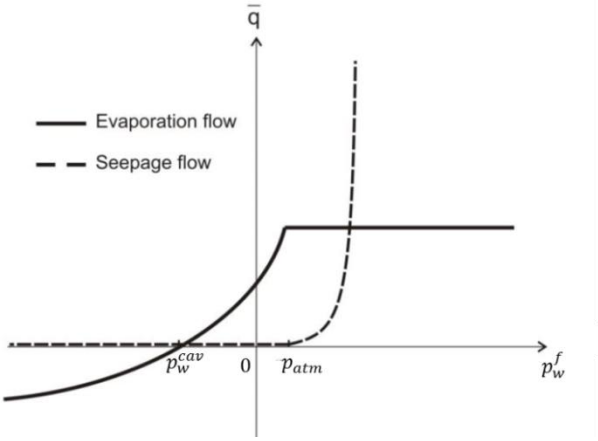

Figure 38: Flow boundary conditions. [GERARD, et al., 2008]

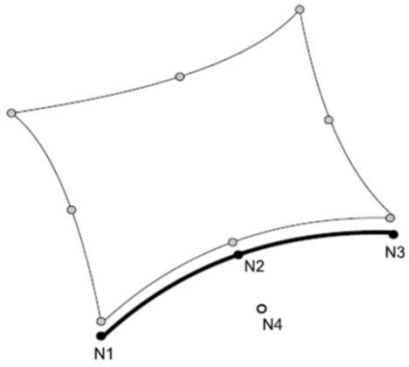

Figure 39: 2-D finite element and boundary FMIVP element. [GERARD, et al., 2008]

From a numerical point of view, a brief description on the finite elements used in this modelling is available in Appendix 8.6. The water and vapour exchanges are modelled through FMIVP elements. They are associated with a classical quadrilateral 2-D finite element, and are defined by four nodes (Figure 39). While the first three nodes (N1, N2 and N3) intervene in the scope of the spatial discretisation of the pore water pressure distribution along the boundary, the fourth node (N4) defines the relative humidity within the cavity. The position of the latter does not influence the water exchanges [GERARD, et al., 2008].

3.5 Conclusion

In the context of hydromechanical modelling, the mathematical model presented is composed of 4 parts: the hydraulic and mechanical models, the hydromechanical couplings and the water and vapour exchanges at the rock wall. The model considers an isotherm medium with a constant gas pressure, and does not take into account the effect of gravity.

The hydraulic model consists in biphasic exchanges in a porous medium saturated by two immiscible fluids: water and air. Because of the constant gas pressure and the absence of gas injection, the phenomena considered are: the advection of the liquid phase, the diffusion of dissolved air in liquid water and the diffusion dry air – water vapour. This model impacts on the mechanical one and vice versa, through the hydromechanical couplings, which are: the notion of effective stresses, the solid density of the medium and in Darcy's law.

The mechanical model presents the properties of elastic and elastoplastic materials. The latter is governed by an internal friction law and considers the hardening/softening effect of the plastic parameters (ϕ and c).

Lastly, water and vapour exchanges between the rock wall and the gallery are described by a non-classical hydraulic condition. It suggests that the total water flow has 2 components: seepage evaporation exchanges.

These mathematical models come with several parameters. The following chapter thus explains how their numerical values are obtained.

4 Parameters Calibration

4.1 The Callovo-Oxfordian Argillite: Description of the Behaviour

Before modelling the ventilation test, the Callovo-Oxfordian argillite (COX) has to be characterised. This section is therefore dedicated to the calibration of the mechanical parameters by means of triaxial tests realised in laboratory conditions. Table 2 describes the conditions in which they were executed. The experimental curves are displayed on Figure 40 and Figure 41.

Name	Triax 01	Triax 02	Triax 03	Triax 04	Triax 05
Laboratory	LML	LML	LML	LAEGO	LAEGO
Size height x diameter [mm]	$40\ x\ 20$	$40\ x\ 20$	$40\ x\ 20$	$40\ x\ 20$	$40\ x\ 20$
Relative humidity: $R.H.$ [%]	90	90	90	90	90
Axial strain rate: $d\varepsilon/dt$ $[s^{-1}]$	10^{-6}	10^{-6}	10^{-6}	$2 * 10^{-5}$	$3.5 * 10^{-6}$
Confining pressure: σ_3 $[MPa]$	12	12	6	2	12
Orientation of the loading with respect to the bedding planes	$\perp$	//	$\perp$	$\perp$	$\perp$

Table 2: Description of the triaxial tests.

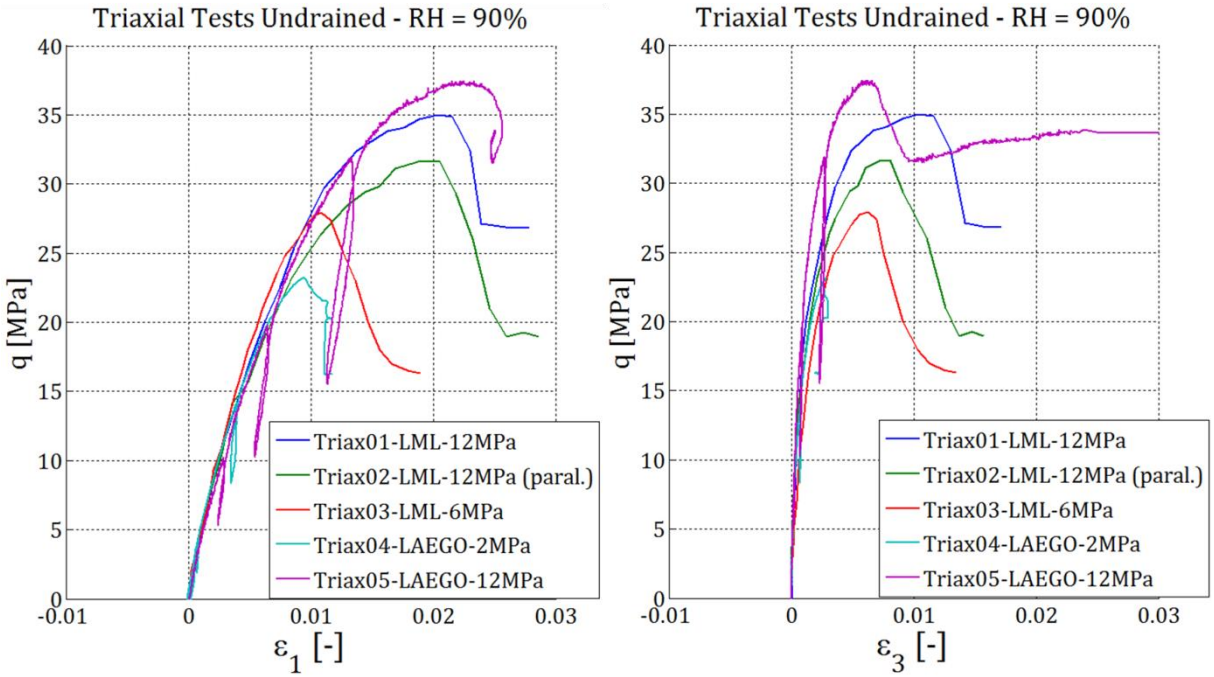

Figure 40: Experimental - Triaxial Tests in Laboratory. Evolution of the deviatoric stress q *with respect to the axial strain* ε_1 *(left) and to the lateral strain* ε_3 *(right).*

The behaviour of the material is quite remote from textbook cases (e.g. perfect plasticity). The stresses path is curved and after the peak, rather than having a horizontal plateau, there is a brittle failure (steep slope) which ends by a residual strength (Figure 40). Figure 41 shows that the stress path $p - q$ stays on the same straight line (i.e. no tilting of the curves) during the whole experiment, even after the breaking point.

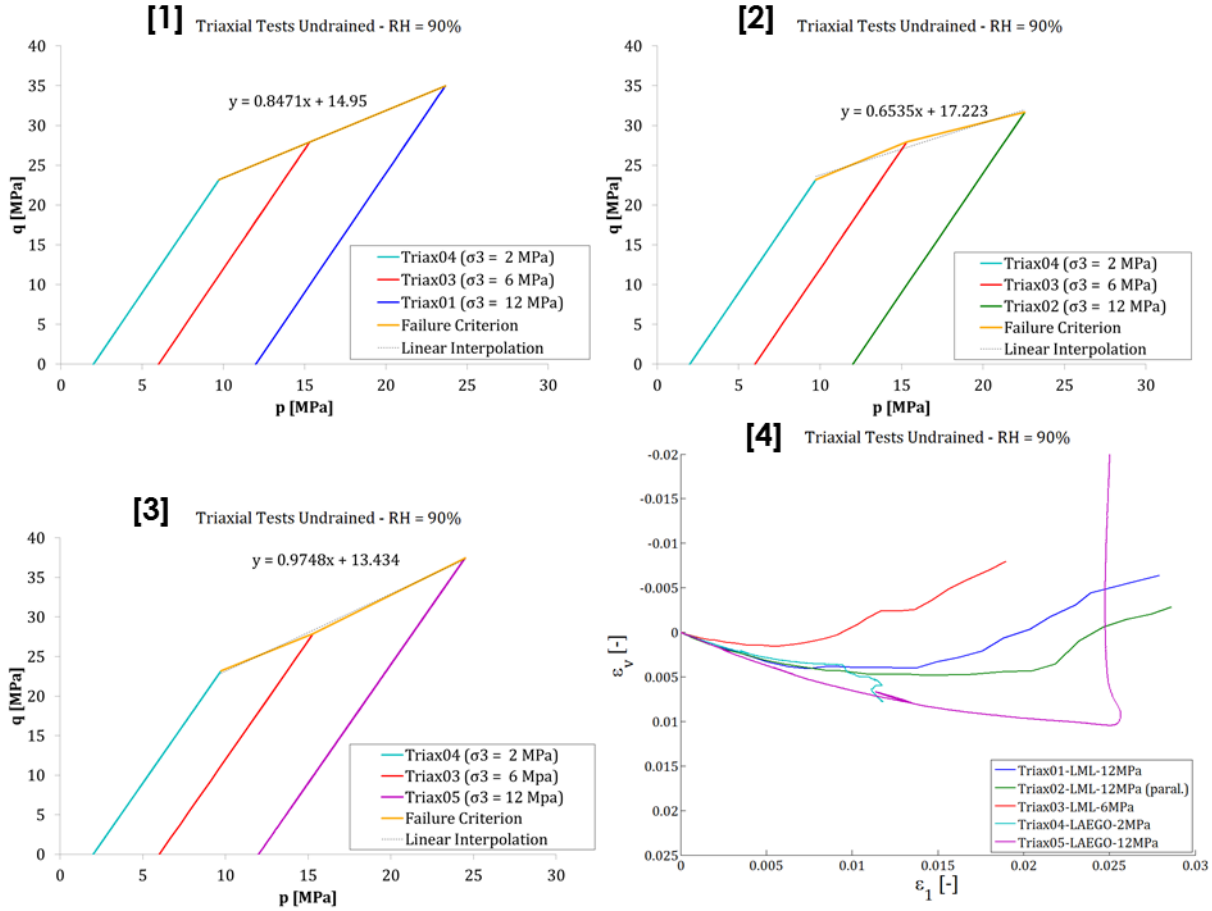

Figure 41: Experimental - Triaxial Tests in Laboratory.
Evolution of the deviatoric stress q *with respect to the mean stress* p *([1], [2] and [3])*
and Evolution of the volumetric strain ε_v *with respect to the axial strain* ε_1 *([4]).*

The damage of the samples results in the development of fractures and can be represented in several ways. On one hand, the fracturing can be reproduced as such by means of classical finite element models (evolving meshing). Furthermore, phenomena prior to the fracture such as cracks and strain localisation can also be modelled (notably using shear banding). In this context, enhanced physical models use the concept of internal length in order to not depend on meshing. They can be split into two categories: models with enriched constitutive laws and models with enriched kinematics i.e. use of macro kinematics and additional micro kinematics, notably through the local second gradient model [PARDOEN, et al., 2014].

On the other hand, the damage can be depicted by a modification of the properties of the material. This method is explored in this work (for plastic properties). In the context of elastoplasticity, delimiting the elastic from the plastic phase is a major hypothesis.

If the behaviour of an elastic material is assimilated to a single straight line, the $q - \varepsilon_1$ graph of Figure 40 shows that the yielding limit is quite rapidly reached ($\varepsilon_1 < 0.5\%$). As a result, the hardening effect of the internal friction angle ϕ must be taken into account (cf. section 3.3.2). The increase of ϕ widens the surface of plasticity (Figure 36). It happens as the material starts to yield. Hence, referring to Equation 41 and Equation 42, we have $\phi_i < \phi_f$ and $\delta_p = 0$.

Moreover, the COX post-peak behaviour is a brittle fracture (steep slope). The development of fractures along which sliding can occur can be interpreted as a post-peak softening effect. In this case, due to the brittleness of the material, the softening is depicted by a sudden decrease of the cohesion c (i.e. softening coefficient $B_c \ll$). Unlike the variation of ϕ, we thus have $c_i > c_f$ and $\delta_c \neq 0$.

Lastly, the dilatancy angle is considered to be equal to zero ($\psi = 0°$). Indeed, the residual strength of the material is represented by a nearly horizontal plateau (Figure 40). The value of ψ also corresponds to the one chosen by [WILEVEAU, et al., 2008] and [CHARLIER, et al., 2013b].

In the following section, we model a triaxial test using LAGAMINE (finite elements code developed by the University of Liège). Because the simulation requires the knowledge of the COX properties, a bibliographic research needs to be done beforehand.

4.2 Parameters Estimation

The research is aimed to find ranges of values for the mechanical (elastic and plastic) parameters in order to model the behaviour of the material.

4.2.1 Elastic Parameters

In triaxial tests, the water pressure applied on the lateral faces of the cylinder leads to the symmetry of the lateral stresses ($\sigma_2 = \sigma_3$). Therefore, the expression of the deviatoric stress q can be simplified into: $q = \sigma_1 - \sigma_3$. Furthermore, in the elastic domain, the deviatoric stress rate Δq is linked to the axial strain rate $\Delta\varepsilon_1$:

$$\Delta q = 3G.\Delta\varepsilon_1 = \frac{3E}{2(1+\nu)}.\Delta\varepsilon_1 \quad (undrained\ conditions) \qquad \textbf{(47)}$$

With G the Coulomb modulus. Let us note that this relation is theoretically only valid for saturated medium (i.e. $RH = 100\%$), thus the need to confront the results with the literature. According to [WILEVEAU, et al., 2008], [CHARLIER, et al., 2013a] and [PARDOEN, et al., 2014], the Poisson ration ν can be estimated at 0.3. Therefore, if we consider the elastic part of the $q - \varepsilon_1$ graph (Figure 40), the Young modulus E resulting from Equation 47 can be graphically deducted. It ranges between 4000 and 5000 MPa. Previous works confirm these values [MAGNENET, et al., 2011] and [PARDOEN, et al., 2015].

4.2.2 Plastic Parameters

The internal friction angle ϕ and the cohesion c can be found using the Drücker-Prager criterion (Equation 36). The $q - p$ graphs (Figure 41 [1] [2] and [3]) show the rupture criterion (in orange) by means of triaxial tests with different confining pressure (2, 6 and 12 MPa). Using the equation of the interpolation line, the parameters can be derived from Equation 37 and Equation 38. As a result, the friction angle ranges between 17° and 25° and the cohesion c from 6.5 MPa to 8.5 MPa. In addition to that, taking into account the hardening effect, initial values of ϕ can be estimated as half the values found at the peak strength, i.e. from 8° to 12° [PARDOEN, et al., 2015], and [CHARLIER, et al., 2013b].

Bibliographic researches show that the values can be more dispersed depending of the relative humidity H_r. Regarding indurated clay rocks at $H_r = 90\%$, the sources suggest values of ϕ range from 10 to 26° and c from 5 to 9 MPa. However, the calculated values are similar to these ones [MAGNENET, et al., 2011], [COLLIN F. , 2013], [PARDOEN, et al., 2015], and [CHARLIER, et al., 2013b].

4.2.3 Summary

Table 3 lists the several values mentioned in the paragraphs here above.

Parameters	Range
$E\ [MPa]$	$4000 - 5000$
$\nu\ [-]$	0.3
$\phi\ [°]$	$10 - 26$
$c[MPa]$	$5 - 9$

Table 3: Preliminary Research – Range of values for the simulation parameters.

4.3 Hydromechanical Modelling – Triaxial Undrained

The triaxial tests simulations are realised in 2D axisymetrical with hydromechanical couplings and in isotherm conditions. The material is isotropic and the mechanical model used is the one presented in section *3.3.2 (Elastoplastic Model with Internal Friction Law)*. The hydraulic model considers an unsaturated porous medium with monophasic flows. In other words, it is similar to the model presented in section 3.1, but without the presence of air.

4.3.1 Geometry and Initial Conditions

Let us consider a triaxial sample of height h and diameter $diam$. By symmetry, the test can be modelled in 2D with only half of the cell (Figure 42). In undrained conditions, there are no water flows (observable ones concern drained triaxial tests) going through the sample. Thus, the water pressure is homogenous, which allows defining the meshing as 1 finite element composed of a single mesh. Regarding the boundary conditions, the displacements are fixed at the bottom of the cell as well as along the vertical symmetry axis (left border). The constant confining pressure applied to the lateral faces of the triaxial cell is reproduced at the right border of the element. Lastly, the loading path is modelled as an increasing displacement[15] imposed at the top of the cell. The strain rate is defined at Table 2.

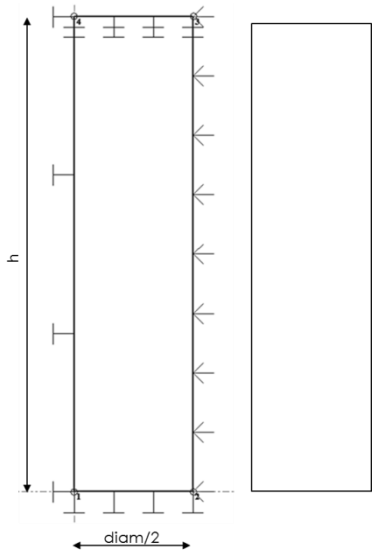

Figure 42: Triaxial Test Modelling - Geometry and Meshing

[15] *Imposed displacement and not imposed loading to avoid the effect related to the granular rearrangement within the cell, which is traduced by the shift of the $q - \varepsilon_1$ curve.*

In undrained tests, the Initial conditions have to take into account the presence of water. The initial effective stresses σ'_{init} are derived from Equation 24:

$$\sigma'_{init} = \sigma_{init} - b.p_{w,init}.S_{r,w,init} \quad \textbf{(48)}$$

With σ_{init} the initial total stresses equal to the confinement pressure, b Biot's coefficient, the initial water pressure $p_{w,init}$ and $S_{r,w,init}$ the initial water saturation degree.

Knowing the relative humidity H_r, $p_{w,init}$ in Equation 48 can be derived from Kelvin's law (Equation 3):

$$p_w = \frac{\rho_w RT}{M_{H_20}} .\ln(H_r) + p_g \quad \textbf{(49)}$$

With ρ_w the water density, M_{H_2O} the molar mass of water, R the ideal gas constant, T [$°K$] the temperature, and p_g the gas pressure. Table 4 and Table 5 show the parameters used to determine the initial water pressure and the initial saturation degree (respectively).

Symbol	Name	Unit	Value
p_g	Air Pressure	MPa	0.1
H_r	Relative Humidity	–	0.9
R	Ideal Gas Constant	$J.mol^{-1}.K^{-1}$	8.314
ρ_w	Water Density	$kg.m^{-3}$	1000
M_{H_2O}	Molar Mass of Water	$kg.mol^{-1}$	0.018
T	Temperature	$°K$	273.15
$\boldsymbol{p_{w,init}}$	**Initial Water Pressure**	$\boldsymbol{MPa}$	$\boldsymbol{-14.16}$

Table 4: Triaxial Test Modelling – Initial Conditions: Parameters of Kelvin's law.

Symbol	Name	Unit	Value
m	Van Genuchten Coefficient	–	0.33
n	Van Genuchten Coefficient	–	1.49
P_r	Air Entry Value (V.G. parameter)	MPa	15
S_{max}	Maximal Saturation	–	1
S_{res}	Residual Saturation	–	0.01
$\boldsymbol{S_{r,w,init}}$	**Initial Saturation**	–	$\boldsymbol{0.81}$

Table 5: Triaxial Test Modelling – Initial Conditions: Parameters of Van Genuchten's model.

Considering Biot's coefficient $b = 0.6$ [CHARLIER, et al., 2013b], and a confinement pressure of 12 MPa, the initial effective stresses are equal to:

$$\sigma'_{init} = 12 + 0.6 * 0.81 * 14.16 = 18.86\ MPa$$

For other values of confinement pressure (2 and 6 MPa), the initial effective stresses are respectively 8.86 and 12.86 MPa.

4.3.2 Simulation Results

In addition to the parameters in Table 4 and Table 5, other hydraulic parameters are needed. The chosen values (Table 6) are inspired from previous works [CHARLIER, et al., 2013a], [PARDOEN, et al., 2014]. The calibration procedure consists in matching the simulations with each test separately and then averaging the 5 sets of parameters obtained.

Symbol	Name	Unit	Value
μ_w	Water Dynamic Viscosity	$Pa.s$	0.001
ρ_w	Water Density	$kg.m^{-3}$	1000
$1/\chi_w$	Water Compressibility	Pa^{-1}	$5\ 10^{-10}$
k	Intrinsic Permeability	m^2	$4\ 10^{-20}$
φ	Porosity	$-$	0.18

Table 6: Triaxial Test Modelling – Hydraulic parameters.

Calibrating each test was realised through trial and error, using the ranges of values (Table 3) as first estimation. Figure 43 displays the comparison between the experimental results of the 5 tests and their respective simulation results. Table 7 lists the 5 sets of parameters used for the calibration.

Regarding the numerical results, although the material was considered isotropic, Figure 43 shows that its properties are not the same in all the directions. Indeed, when the $q - \varepsilon_1$ numerical curve matches its experimental pendant, the correspondence is not as good regarding between both $q - \varepsilon_3$ curves (and vice versa). For instance, the Triax05 test shows that before the peak, the numerical curve in magenta ($q - \varepsilon_1$) does not fit as well as the one in red ($q - \varepsilon_3$). Furthermore, while the post-peak softening happens sooner for the first curve, it occurs later for the second one. These observations are supported by the value of the Young Modulus chosen for the Triax02 test. The latter is actually the only test in which the loading is not perpendicular but parallel to the bedding planes of the sample.

Symbol	Name	Unit	Triax01	Triax02	Triax03	Triax04	Triax05
$\boldsymbol{E}$	Young Modulus	MPa	4 000	5 000	4 000	4 000	4 000
$\boldsymbol{\rho_s}$	Grain Density	$kg.m^{-3}$	2 750	2 750	2 750	2 750	2 750
$\boldsymbol{\nu}$	Poisson Coefficient	$-$	0.3	0.3	0.3	0.3	0.3
$\boldsymbol{\phi_i}$	Initial Friction Angle	°	10	10	10	10	12
$\boldsymbol{\phi_f}$	Final Friction Angle	°	22	19.5	19	22	22
$\boldsymbol{B_p}$	Hard. /Soft. Coeff.	10^{-4} [−]	9	15	9	9	9
$\boldsymbol{c_i}$	Initial Cohesion	MPa	4.5	5	6	4.8	5.5
$\boldsymbol{c_f}$	Final Cohesion	MPa	1.5	1.5	1.5	1.5	3.5
$\boldsymbol{B_c}$	Hard. /Soft. Coeff.	10^{-4} [−]	30	30	30	30	21
$\boldsymbol{\delta_c}$	Hard. /Soft. Delay	10^{-2} [−]	1.6	1.4	0.9	0.6	1.3
$\boldsymbol{\sigma_3}$	Conf. Pressure	MPa	12	12	6	2	12

Table 7: Triaxial Test Modelling – Calibration: Individual sets of mechanical parameters with representation of the post-peak behaviour.

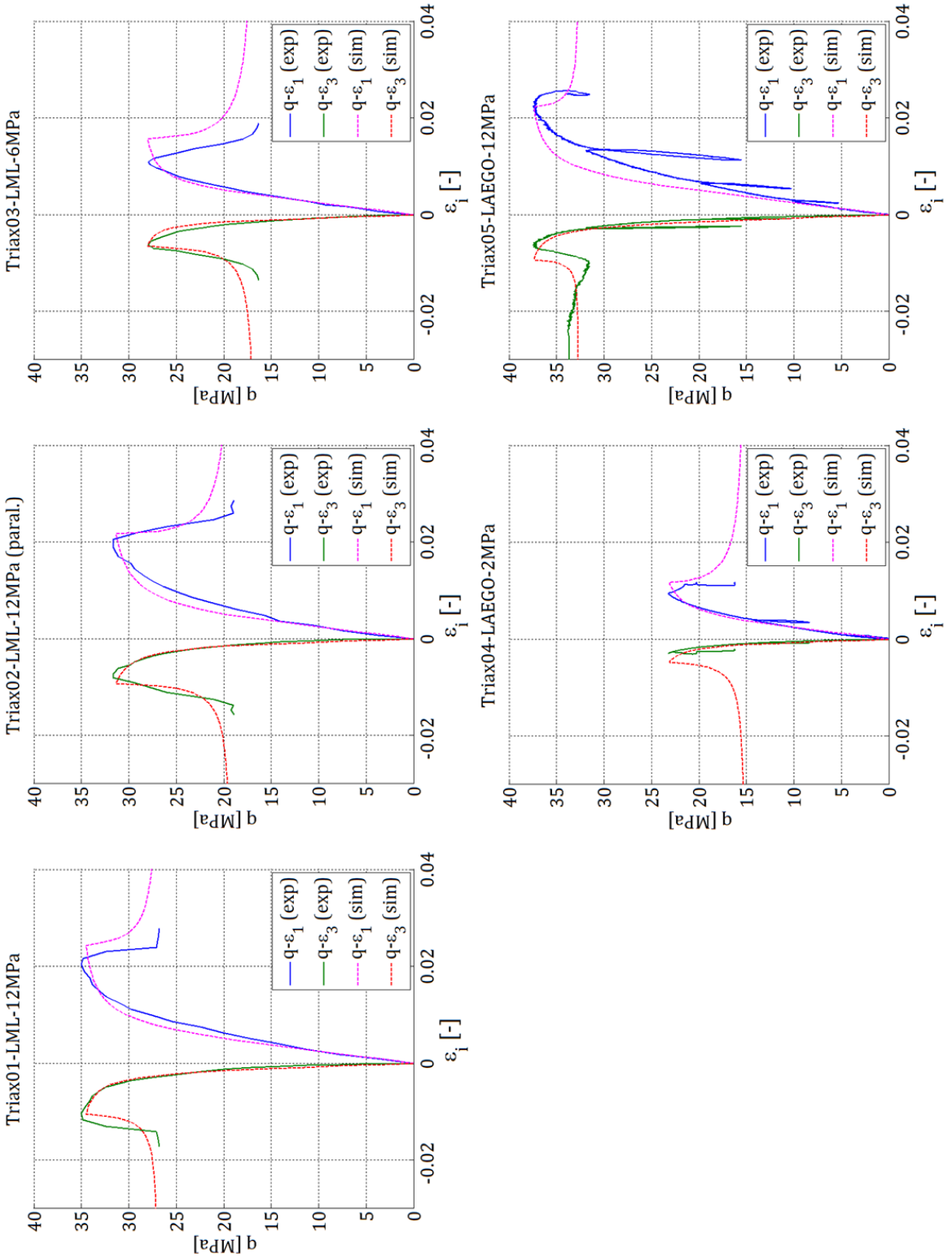

Figure 43: Triaxial Test Modelling - Results: Calibration with post-peak behaviour. Set of individual parameters (cf. Table 7). Experimental curves are in blue and green, and simulation curves in magenta and red.

Another remark is related to the post-peak behaviour. As explained previously, the steeper the slope, the smaller the softening coefficient B_c. However, it can be observed that the calibrated values are greater than those of the hardening coefficient B_p. In fact, these values are limited by numerical constraints (i.e. convergence).

Lastly disparities in the plastic parameters are observed, especially in the values of the initial cohesion c_i, and the delay at which the post-peak softening starts.

When modelling the ventilation test, only one set of parameters is needed. Table 8 displays the averaged values resulting from the individual calibration (Figure 43).

E $[MPa]$	ρ_s $[kg/m^3]$	ν $[-]$	ϕ_i [°]	ϕ_f [°]	B_p $10^{-4}[-]$	c_i $[MPa]$	c_f $[MPa]$	B_c $10^{-4}[-]$	δ_c $10^{-2}[-]$
4 000	2 750	0.3	10.4	20.9	10.2	5.16	1.62	28.3	1.16

Table 8: Triaxial Test Modelling – Calibration: Average of the sets of parameters (with representation of the post-peak behaviour) presented in Table 7.

However, the development of fractures within the COX formation is a complex phenomenon to model[16]. In addition to that, considering what happens after the peak with the presented physical model brings convergence problems during the simulations. This is the reason why we decide to not represent the post-peak softening. Still, considering a constant value of the cohesion $c = c_i = c_f$ requires repeating the calibration procedure.

As the methodology is similar to the previous case, the details of the calibration are skipped. Table 9 lists the set of final parameters used for the modelling of the ventilation test. The results of the simulation are shown on Figure 44. Let us remind that the hardening effect is maintained, and most of all that the dilatancy angle $\psi = 0°$ (hence the asymptotic horizontal behaviour of the numerical curves). The final numerical values of the strength correspond to the peak values of the experiments. Lastly, averaging the values of the parameters suggests some disparities regarding the concordance with the experimental curves.

E $[MPa]$	ρ_s $[kg/m^3]$	ν $[-]$	ϕ_i [°]	ϕ_f [°]	B_p $10^{-4}[-]$	c_i $[MPa]$	c_f $[MPa]$	B_c $10^{-4}[-]$	δ_c $10^{-2}[-]$
4 000	2 750	0.3	10	22	9	4.5	4.5	/	/

Table 9: Triaxial Test Modelling – Calibration: Mean parameters without post peak behaviour. Final set of parameters.

[16] *For instance, [PARDOEN, et al., 2015] investigates the subject by means of enhanced mathematical models, notably considering the development of shear strain localisation bands with microstructure effects taken into account.*

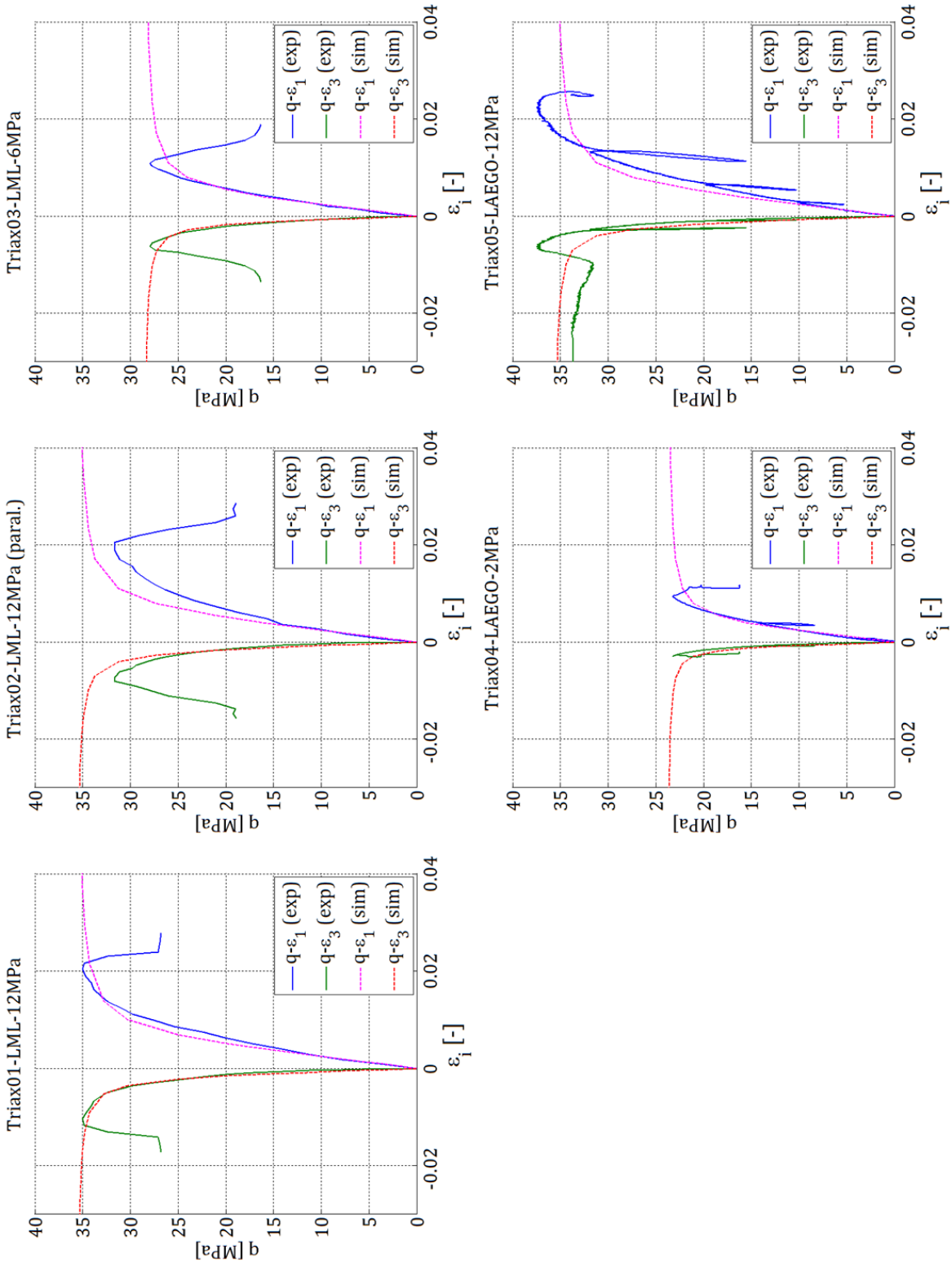

Figure 44: Triaxial Test Modelling - Results: Calibration without post peak behaviour. Set of mean parameters (cf. Table 9). Experimental curves are in blue and green, and simulation curves in magenta and red.

4.4 Conclusion

In this chapter, the parameters of the physical models are obtained by means of undrained triaxial tests realised on Callovo-Oxfordian (COX) samples. These values were first graphically estimated, which gave us ranges of values. The results were then supported by a bibliographic research.

The parameters calibration was achieved through trial and error in order to fit as well as possible the numerical curves with the experimental curves. Each test has been calibrated separately, taking the post-peak behaviour into account. The sets of parameters obtained for each simulation were then averaged in order to keep only one (i.e. mean set of parameters).

In spite of that, the final set of parameters chosen for the next simulations (Table 9) was obtained without considering the post-peak behaviour. The methodology was the same as in the previous case, with in mind that the asymptotic strength values tried to correspond with the peak values of the experimental curves. Figure 44 shows a good correspondence with the experimental curve, regardless of the disparities engendered by averaging.

With this set of parameters, the next chapter focuses on the hydromechanical modelling of the ventilation test realised in the URL of Bure.

5 Modelling

The SDZ experiment is aimed to study the evolution of the excavated damaged zone (EDZ) through a ventilation test. This test is performed in the gallery GED (Figure 15), and induces a desaturation (with possible resaturation) of the rock formation (COX).

Several works studying this phenomenon are available in the literature [GUILLON, 2011] [CARIOU, 2010] and [CHARLIER, et al., 2013a]. Among them, one solution is to model the EDZ by manually delimiting a zone (i.e. fixed dimensions) with more critical properties [CHARLIER, et al., 2013b]. In this work, the approach is different. The aim of these simulations is to propose laws of behaviour that modify the hydraulic parameters on the basis of the mechanical variables. In particular, the work seeks to correlate the evolution of the intrinsic permeability of the medium with a variable that quantifies the rock damage. Consequently, the hydraulic behaviour of the medium evolves in the same way regardless of the orientation.

For this purpose, the section dedicated to the simulations is divided into 3 parts. The first one is devoted to describing the evolution of the permeability and leads to the determination of a numerical model that provides a good correspondence with the experimental measurements. The second part analyses the several impacts of the ventilation test itself, such as the desaturation, the drop of water pressure and the convergence of the rock formation. Lastly, the third part introduces the concept of anisotropy of the mechanical parameters and interprets the resulting effects.

The modelling is achieved by means of the non-linear finite elements code LAGAMINE developed at the University of Liège. The simulations are carried out in **2D plane strain with hydromechanical couplings, in isotherm conditions and with a constant gas pressure**. The starting configuration considers an isotropic material governed by the mechanical and hydraulic models described in chapter 3.

Before entering into the main subject, this chapter first presents the conditions in which the simulations are realised: the geometry of the meshing, the initial and the boundary conditions. The latter gives the far limit conditions imposed at the extremities of the domain and explains how the excavation and the ventilation test are modelled. Furthermore, regarding the excavation, the main concepts of the convergence/confinement theory are introduced beforehand. The values of the several parameters used in the modelling are also specified.

5.1 Geometry, Initial and Boundary Conditions

5.1.1 Geometry

The problem is in 2D plane strain conditions and the reference frame $(\hat{x}, \hat{y}, \hat{z})$ is such that the represented cross-section corresponds to the $(\hat{x} - \hat{y})$ plane (Figure 46). As a reminder, the section of the GED gallery is depicted at Figure 27 (p.20). For reasons of symmetry, only half of the section has been computed (Figure 45). The boundary conditions consist in nodes fixed in displacements and pore pressure. They are located far away from the gallery, such that imposing values at these nodes (far limit conditions, cf. section 5.1.3A) doesn't affect the behaviour of the host formation surrounding the gallery. This hypothesis is verified notably through reactions close to zero (or also constant pore pressure) at the boundaries of the domain.

The meshing is composed of 4357 elements, and 12981 nodes. It extends over 400 metres vertically and 200 metres horizontally. The dimensions of the gallery are shown on Figure 47. Furthermore, the meshing represents the argillite formation, the concrete slab situated at the lower part of the gallery, and FMIVP elements (not visible, cf. section 3.4). The shape and size of each mesh depends on its position with regard to the gallery. Indeed, a fine meshing surrounds the gallery and gets coarser as we move away from rock wall. Consequently, a high precision of the results is obtained while reducing the computation time.

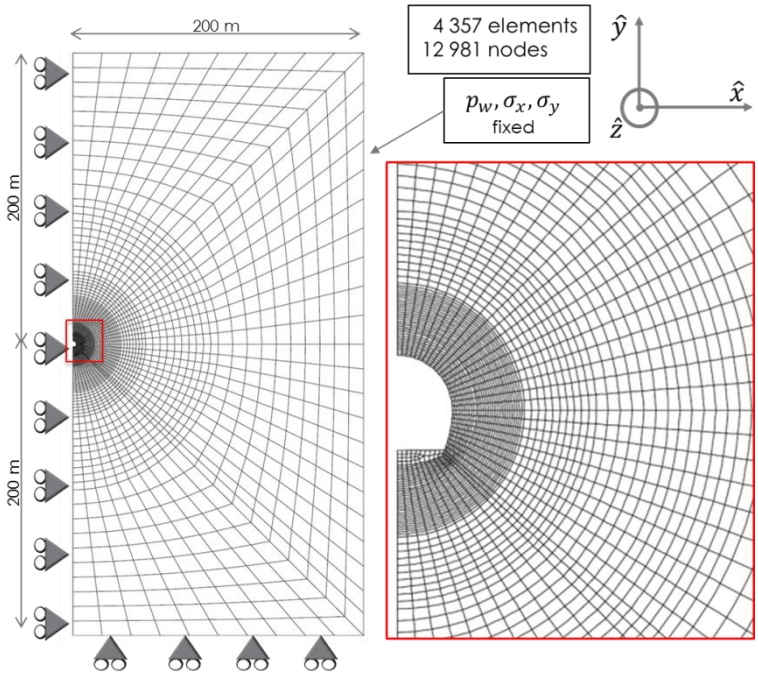

Figure 45: Global view of the geometry of the meshing, with boundary conditions (left) and zoom on the gallery (right).

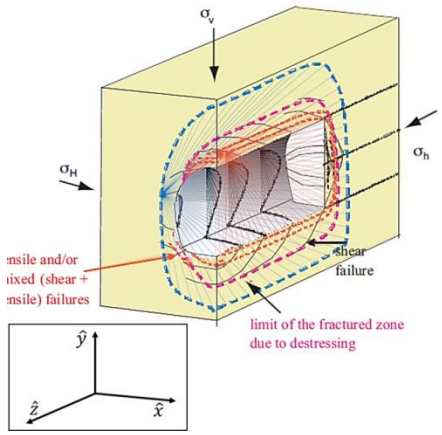

Figure 46: Reference frame adopted for the simulations

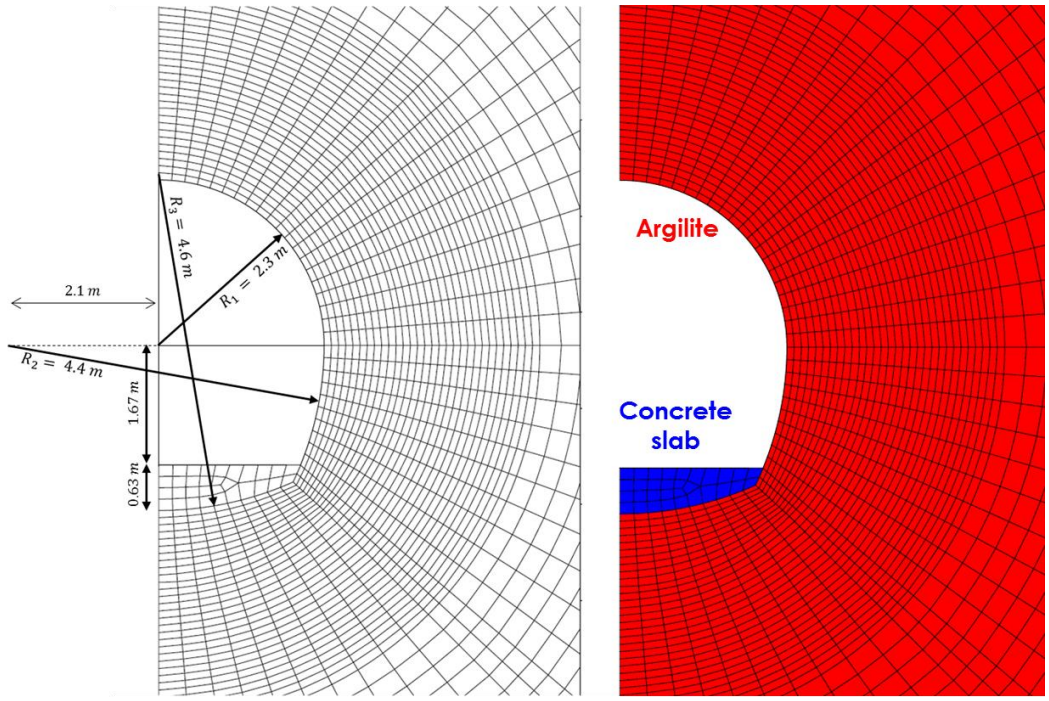

Figure 47: View of the gallery – Dimensions and Constitution

5.1.2 Initial Conditions

In addition to plane strain conditions, the gas pressure is kept at a constant value of the atmospheric pressure (0.1 MPa) and the model is entirely isotherm. Water pressure inside the argillite is initially set at 4.5 MPa and the one inside the concrete slab is equal to the atmospheric pressure:

- Gas Pressure: $p_g = 0.1\ MPa$
- Temperature: $T = 293\ °K\ (20°C)$
- Water Pressure of the argillite: $p_w = 4.5\ MPa$
- Water Pressure of the concrete slab: $p_w = 0.1\ MPa$

From a mechanical point of view, anisotropic initial stresses are imposed. They can be expressed using the coefficient K_0:

$$\sigma_0^h = K_0\ \sigma_0^v \qquad \textbf{(50)}$$

This coefficient is usually smaller than 1 [CHARLIER, 2013]. However, the initial conditions of the GED gallery are the following:

- $\sigma_{h;0} = \sigma_{v;0} = 12.0\ MPa$
- $\sigma_{H;0} = 15.6\ MPa \quad thus\colon\ K_0 = 1.3$

With $\sigma_{h;0}$ and $\sigma_{v;0}$ the minor principal stresses, respectively horizontal and vertical, and $\sigma_{H;0}$ is the major horizontal principal stress. The direction of the GED gallery is along the minor horizontal principal stress $\sigma_{h;0}$. The effect of gravity is not considered.

The hydromechanical coupling implies that the effective stresses within the host formation take the presence of water into consideration. The calculation method is similar to the one used for the triaxial tests (cf. section 4.3.1). Here, as the water pressure is far greater than the atmospheric gas pressure ($p_w = 4.5\ MPa > 0.1\ MPa$), there is no suction and the medium is initially saturated ($S_{r,w} = 1$). Therefore, the effective stresses are equal to:

$$\begin{aligned} \boxed{\sigma'_{v;0}} &= \sigma_{v;0} - b * S_{r,w} * p_w \\ &= 12.0 - 0.6 * 1 * 4.5 = \boxed{9.3\ MPa} \\ \boxed{\sigma'_{H;0}} &= \sigma_{H;0} - b * S_{r,w} * p_w \\ &= 15.6 - 0.6 * 1 * 4.5 = \boxed{12.9\ MPa} \end{aligned} \qquad thus\ \ \sigma'_{H;0} = \boxed{1.387} * \sigma'_{v;0}$$

5.1.3 Boundary Conditions

A. Far Limit Conditions

The displacements are blocked in accordance with Figure 45 (left). The stresses and the water pressure ($p_w = 4.5\ MPa$) are fixed at the boundaries of the domain, i.e. at 200 m from the centre of the GED gallery.

B. Excavation – Convergence/ Confinement Theory

The theory tells that in isotropic conditions, radial and orthoradial stresses follow respectively Equation 51 and Equation 52 in the elastic domain [Panet, et al., 1974]:

$$\sigma_\rho = \left(1 - \lambda.\frac{R^2}{\rho^2}\right).\sigma_0 \qquad \textbf{(51)}$$

$$\sigma_\theta = \left(1 + \lambda.\frac{R^2}{\rho^2}\right).\sigma_0 \qquad \textbf{(52)}$$

With λ the deconfining rate, R the radius of the gallery, and ρ ($\geq R$) the radial distance.

The deconfining rate evolves from 0 at the beginning to 1 at the end of the excavation. Indeed, before any drilling, the stresses surrounding the future gallery correspond to the initial stress state within the medium. Throughout the excavation phase, the deconfinement rate keeps increasing. This subsequently decreases the radial stress σ_r and increases the orthoradial stress σ_θ. In contrast, the mean stress remains constant for any deconfining rate λ ($(\sigma_\rho + \sigma_\theta)/2 = \sigma_0$). At the end of the process, at the rock wall the stress state is the following:

$$\begin{cases}\lambda = 1\\ \rho = R\end{cases} \rightarrow \begin{cases}\sigma_R = 0\\ \sigma_\theta = 2\,\sigma_0\end{cases}$$

These results depict the vault phenomenon. The radial stresses are gradually transferred to the tangential direction. This conversion leads to a displacement of the rock wall, known as *convergence*. In the elastic domain, the convergence is quantified by multiplying by 2 the radial displacement u_ρ which is expressed in Equation 53.

$$u_\rho = -\lambda\frac{R^2}{\rho}.\frac{\sigma_0}{2G} \qquad \textbf{(53)}$$

With G the Coulomb's modulus. Similarly to the stresses, the displacement of the rock wall at the end of the excavation is obtained with $\lambda = 1$ and $\rho = R$:

$$u_R = \frac{\sigma_0 R}{2G}$$

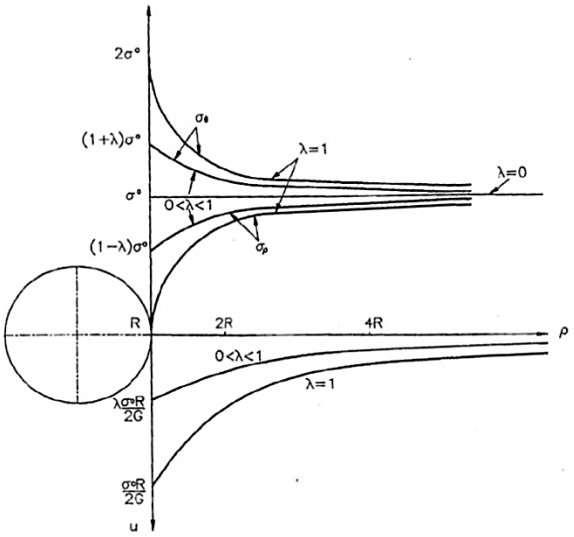

Figure 48: Evolution of the radial and orthoradial stresses, and of the displacement with respect to the radial distance, for several values of deconfining rate. [COLLIN F. , 2014]

Figure 48 displays the evolution of those three variables with respect to the radial distance ρ at the beginning ($\lambda = 1$), during ($0 < \lambda < 1$) and at the end of the excavation phase ($\lambda = 1$). Let us note that far away from the gallery ($\rho \gg$), both stresses tend to their initial value, while the displacement is close to 0.

Lastly, the theory explained here above is applicable in the elastic domain only. Indeed, the stresses do not increase indefinitely. Once they reach the failure criterion (Drücker-Prager, cf. section 3.3.2), the material yields. The plastic loading is governed by the consistency condition, i.e. the stresses path remains on the yield surface [CHARLIER, 2000].

C. Excavation – Modelling

The excavation process of the gallery is realised along the $\hat{z}$ direction (Figure 46) and is considered to last 21 days. The gallery is drilled at a rate of a radius r every week, i.e. $2.3\ m/week$ [CRUCHAUDET, et al., 2010b]. From the beginning to the end of the excavation phase, the state of stress of the rock surrounding the cavity decreases from $15.6\ MPa$ (horizontally) and $12\ MPa$ (vertically) to both $0.1\ MPa$ (atmospheric pressure). Furthermore, the excavation front also decreases the water to the same value. Figure 49 (left) represents the imposition of the stresses and water pressure at the rock wall, with respect to time. The values decrease according to the advancement of the excavation front (which is actually the result of the convergence/confinement theory, cf. Figure 49 right).

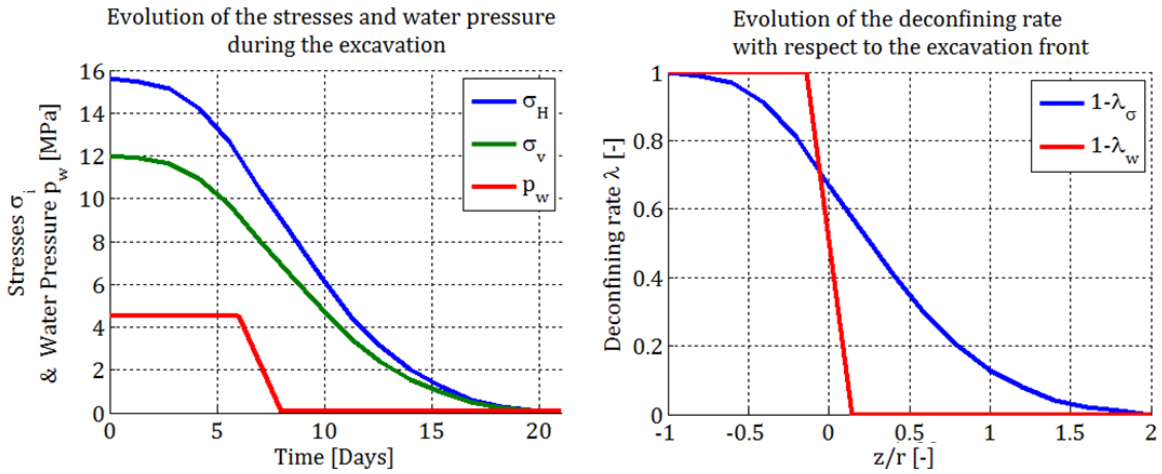

Figure 49: Left - Evolution of the stresses (blue and green) and water pressure (red) during the excavation phase (21 days). Right – Evolution of the deconfining rate with respect to the excavation front. The excavation advances at a radius r *per week, along the direction* $\hat{z}$.

The excavation is modelled from -23 days to -2 days, so that day 0 would correspond to the beginning of the ventilation test. Figure 50 displays the several events on a timeline. The chronology is listed here below:

- The initial stresses and water pressure are imposed at the rock wall;
- Between -23 days and -2 days, the stresses are decreased until the atmospheric pressure (0.1 MPa);
- Between -17 days and -15 days, the water pressure goes down to 0.1 MPa;
- Between -15 days and -2 days, the water pressure is maintained to 0.1 MPa;
- Between -2 and 0 days, the water pressure is decreased to the first measured values (beginning of the ventilation test);
- After, the water pressure is imposed in the gallery according the values of relative humidity.

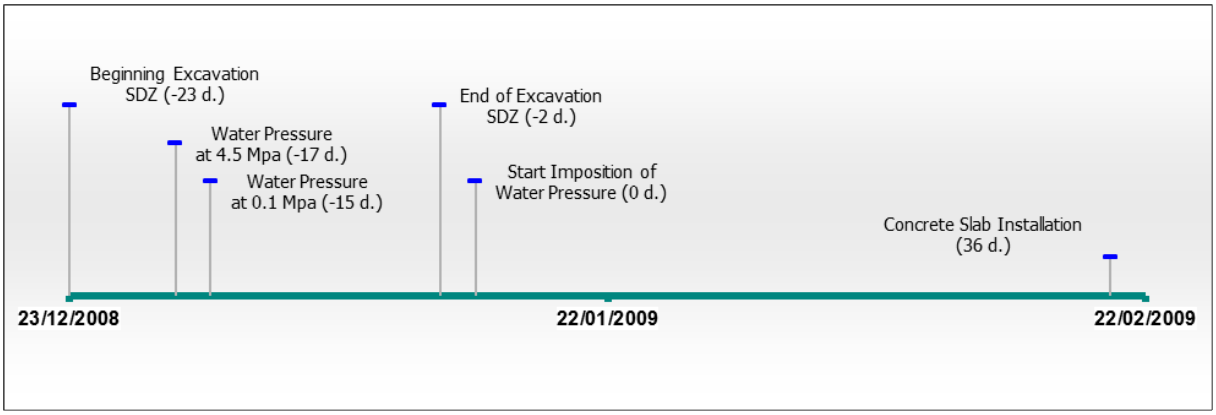

Figure 50: Timeline of the excavation phase.

D. Ventilation Test – Modelling

Let us remind beforehand that climatic measures (temperature and hygrometry) were taken in the sections SDZ1261 to SDZ1264 (i.e. uncoated SDZ zone, cf. section 2.5.3B, p.19). Appendix 8.1 details the positions of the sections, the temperature and hygrometry sensors, as well as the evolution of the measures with respect to time. Figure 51 represents the daily mean values of those measures.

The ventilation test consists in injecting an air flow with a certain degree of humidity H_r in the gallery. Numerically, it is achieved through the water pressure p_w. The latter is derived from Kelvin-s law – similarly to the triaxial tests modelling (cf. section 4.3.1, p.36) – but with the difference that this time, the parameters used to determine p_w (i.e. H_r and T) correspond to the experimental measures mentioned above. Therefore, although the model was described in isotherm conditions to avoid the consideration of thermal couplings, Figure 51 shows that the temperature variations are not as significant as those of the relative humidity. Moreover, as T is expressed in $[°K]$ in Kelvin's law, it can be pointed out that the gap between the maximal and the minimal values is less than 5%, whereas concerning relative humidity, the difference exceeds the 75%. As a result, the water pressure curve is much more similar to the curve of the latter. This is the reason why the model can consider isotherm conditions.

From a technical point of view, the imposed water pressure corresponding with the temperature and hydrometric measures (daily mean values, cf. Figure 51) is imposed at the rock wall of the gallery by means of an environmental node FMIVP (cf. Figure 39, section 3.4).

The test begins on the 15th of January 2009 and has lasted, as of now, 2217 days. The several phases listed in Table 8.

Time	Date	Phase
Day 0	15/01/2009	Beginning of the ventilation test
Day 36	20/02/2009	Installation of the concrete slab
Day 230	02/09/2009	Airlock closed
Day 2 217	15/02/2015	End of Simulation

Table 10: Major events during the ventilation test.

The graphs of Figure 51 show several tendencies. Before the airlock closing (represented as red dash line 1), the climatic conditions of the SDZ zone are those of the GED gallery: entries and exits of the workers, concrete casting, installation of instrumentation, etc. As a result, the temperature has increased. After the closing (day 230), the test zone is ventilated with random conditions resulting from transfers through the EDZ. Then, two campaigns of constant ventilation can be observed (red dash lines 2 and 3). The first one starts at the beginning of 2012 (day 1081) and the second one at mid-August 2013 (day 1673). The conditions aimed by these campaigns are shown on Figure 51. The data's show several fluctuations throughout the whole ventilation test, both at a daily scale and at a seasonal scale.

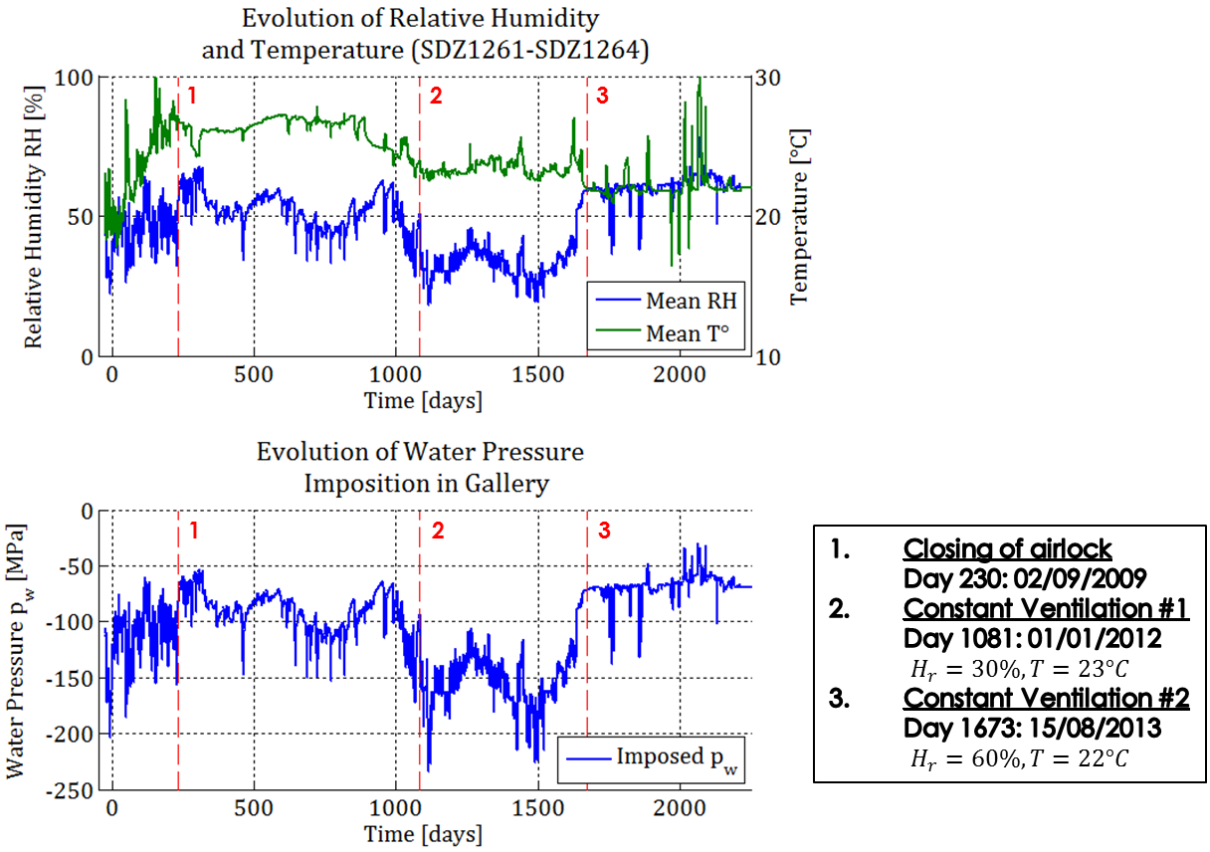

Figure 51: Up - Evolution of the relative humidity and the temperature in the uncoated SDZ zone. Daily mean values. Down – Evolution of the water pressure imposed in the gallery (SDZ zone).

5.2 Parameters of the Hydraulic and Mechanical Models

Among the parameters used in the starting simulation, there are the parameters which were calibrated in chapter 4, but also parameters with typical values (e.g. densities, viscosities) and others which are inspired from previous works (e.g. tortuosity, porosity, Biot's coefficient…) [GERARD, 2011] [CHARLIER, et al., 2013b].

Table 11 displays the numerical values of the several properties of water and air, which are the components of the gaseous phase. As a reminder, the properties are given for a temperature of $293°K$ and an air pressure of $0.1\ MPa$. Table 12 to Table 14 give the values of the parameters used in the hydraulic (biphasic transfers) and mechanical (internal friction with hardening) laws governing each material.

5.2.1 Water and Air

Symbol	Name	Unit	Value
μ_w	Water Dynamic Viscosity	$Pa.s$	0.001
ρ_w	Water Density	$kg.m^{-3}$	1000
$1/\chi_w$	Water Compressibility	Pa^{-1}	$5\ 10^{-10}$
μ_a^g	Air Dynamic Viscosity	$Pa.s$	$17.9\ 10^{-6}$
$\mu_{H_2O}^g$	Water Vapour Dynamic Viscosity	$Pa.s$	10^{-5}
ρ_{Air}^g	Air Density	$kg.m^{-3}$	1.1822
H_{Air}	Henry Constant	$-$	0.0234

Table 11: Water and Air properties.

5.2.2 Argillite

A. Hydraulic Parameters

Symbol	Name	Unit	Value
k	Intrinsic Permeability	m^2	$4\ 10^{-20}$
φ	Porosity	$-$	0.173
m	Van Genuchten Coefficient	$-$	0.33
n	Van Genuchten Coefficient	$-$	1.49
P_r	Air Entry Value (V.G. parameter)	MPa	15
S_{max}	Maximal Saturation	$-$	1
S_{res}	Residual Saturation	$-$	0.01
τ	Tortuosity	$-$	0.25

Table 12: Hydraulic parameters of the argillite.

B. Mechanical Parameters

Symbol	Name	Unit	Value
E	Young Modulus	MPa	4000
ν	Poisson Coefficient	$-$	0.3
c	Cohesion	MPa	4.5
ϕ_i	Initial Friction Angle	$°$	10
ϕ_f	Final Friction Angle	$°$	22
B_p	Hardening/Softening Coefficient	$-$	$9\ 10^{-4}$
b	Biot Coefficient	$-$	0.6
ρ	Density	$kg.m^{-3}$	2750

Table 13: Mechanical parameters of the argillite.

5.2.3 Concrete

A. Hydraulic Parameters

Symbol	Name	Unit	Value
k	Intrinsic Permeability	m^2	$1\ 10^{-18}$
φ	Porosity	$-$	0.20
m	Van Genuchten Coefficient	$-$	0.33
n	Van Genuchten Coefficient	$-$	1.49
P_r	Air Entry Value (V.G. parameter)	MPa	2
S_{max}	Maximal Saturation	$-$	1
S_{res}	Residual Saturation	$-$	0.01
τ	Tortuosity	$-$	0.25

Table 14: Hydraulic parameters of the concrete.

B. Mechanical Parameters

Symbol	Name	Unit	Value
E	Young Modulus	MPa	$30\ 000$
ν	Poisson Coefficient	$-$	0.3
b	Biot Coefficient	$-$	0.6
ρ	Density	$kg.m^{-3}$	$2\ 300$

Table 15: Mechanical parameters of the concrete.

5.2.4 Water and Vapour Exchanges at the Rock Wall

The parameters characterising the water and vapour exchanges are displayed in Table 16. The default value of the transfer coefficient is chosen according to previous works [CHARLIER, et al., 2013a] and [GERARD, 2011].

Symbol	Name	Unit	Value
K_{pen}	Penalty coefficient for seepage	$s.kg^{-1}$	10^{-10}
α_0	Transfer Coefficient	$m.s^{-1}$	10^{-3}

Table 16: Water Exchanges parameters – FMIVP elements (default values).

5.3 Simulations

When modelling the EDZ, one possible approach is to delimit a zone with fixed dimensions in which the properties are more critical [CHARLIER, et al., 2013b]. In this work, the aim of these simulations is to propose laws of behaviour that modify the hydraulic parameters on the basis of the mechanical variables. In particular, the work seeks to correlate the evolution of the intrinsic permeability of the medium with a variable that quantifies the rock damage. Consequently, the hydraulic behaviour of the medium evolves in the same way regardless of the orientation.

This section can thus be divided into 3 parts. The first one is devoted to describing the evolution of the permeability and ends with the determination of a numerical model that provides a good correspondence with the experimental measurements.

As the rock damage largely takes place during the excavation, this first part mainly focuses on that period. Nonetheless, in the interests of clarity and coherence, the calibration of the parameters used in these laws is not presented (although alternative results can be mentioned). Instead, this part is devoted to explaining the steps that lead to the enhancement of the mathematical model.

For this purpose, the numerical results are compared to the experimental data's. Among these measures, the evolution of the water pressure can be presented in several ways: with respect to time in the SDZ drills (or boreholes, cf. Figure 52) as well as at particular points located at the rock wall (Figure 53 left). They can also be shown along oriented sections across the gallery, i.e. with respect to the distance from the rock wall (Figure 53 right). More details about the water pressure measurements and the SDZ drills are given at appendix 8.2.

The second part analyses the several impacts of the ventilation test itself, and confronts the numerical results with other available experimental measurements, such as the water content and the convergence of the rock formation. Lastly, the third part introduces the concept of anisotropy of the mechanical parameters (elastic and plastic).

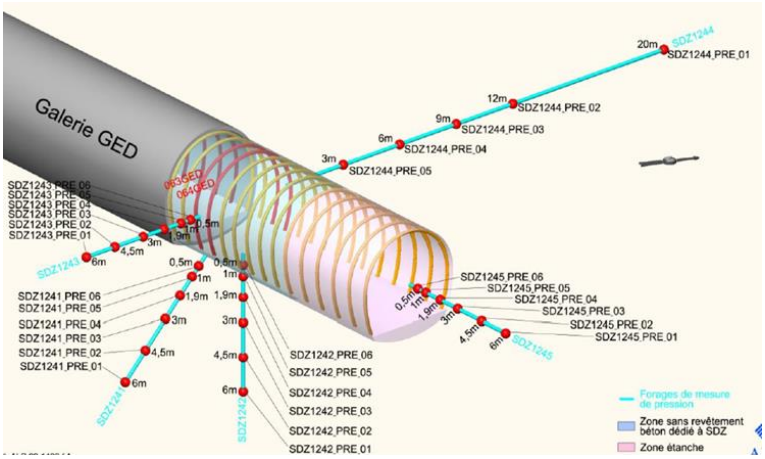

Figure 52: SDZ drills in which experimental water pressures are measured. [CRUCHAUDET, et al., 2010a]

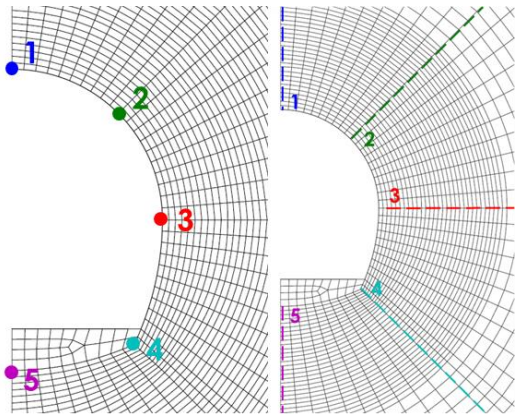

Figure 53: Points at the rock wall (left) and radial sections along which the numerical results are given (right).

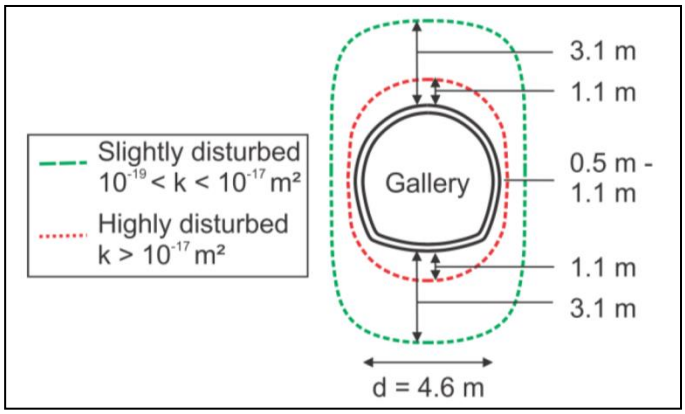

Figure 54: Sketch of the EDZ based on the variation of the intrinsic permeability measured on site. [CRUCHAUDET, et al., 2010a]

5.3.1 Description of the Evolution of Permeability

In section 3.2, the notion of effective stresses and the variation of the solid density of the medium were introduced as mechanical couplings. A third aspect can be added: the evolution of the intrinsic permeability k_{int}. In order to simplify the following tensor notations, the subscript '*-int*' is taken away.

The extension of the EDZ on the basis of permeability measurements is of $0.5\,m$ horizontally and of $1.1\,m$ vertically [CRUCHAUDET, et al., 2010a]. Within this zone, the permeability is highly disturbed ($k > 10^{-17}\,m^2$). Furthermore, an outer zone in which the permeability is slightly disturbed ($10^{-19} < k < 10^{-17}$) is surrounding the previous one: it extends up to $1.1\,m$ horizontally and $3.1\,m$ vertically (Figure 54). Thus, the EDZ is a zone in which the permeability is higher (by 2 to 3 orders of magnitude) compared to the undamaged zone. Section 2.5 gives further details about the EDZ as well as the measurements done.

In the aim to characterise the evolution of the EDZ and to reproduce the experimental data's, this first part tries to correlate the evolution of the intrinsic permeability of the medium with a variable that quantifies the rock damage, bearing in mind that the EDZ is around 3 times wider vertically than horizontally. In this aim, a first mechanical variable used to modify the permeability is the total equivalent strain.

A. Considering the Total Equivalent Strain (Formulation 1)

Referring to the advection of the liquid phase (Darcy's law, Equation 9), a first formulation suggests that the intrinsic permeability can vary according to the total equivalent strain ε_{eq}[17]:

FORMULATION 1

$$\begin{aligned} &if\ \varepsilon_{eq} \le \varepsilon_{eq}^{thr}:\ \ k_{ij} = k_{ij,0} \\ &if\ \varepsilon_{eq}^{thr} < \varepsilon_{eq}:\ \ k_{ij} = k_{ij,0}\left(1 + \theta\,.\left(\varepsilon_{eq} - \varepsilon_{eq}^{thr}\right)^{\beta}\right) \end{aligned} \qquad \textbf{(54)}$$

With $k_{ij,0}$ the initial intrinsic hydraulic permeability tensor, θ and β are two coefficients of the permeability evolution and ε_{eq}^{thr} the total equivalent strain threshold below which the permeability does not evolve.

The formalism of this equation is similar to the GDR MoMas formulation [Chavant, et al., 2005], with the difference that the permeability evolution depends on the porosity instead of the strain. Yet, the GDR MoMas equation requires a very deformable porous medium (or highly deformable grains) so that the difference of porosities would be noticeable. In contrast, Equation 26 allows a more flexible permeability modification since the threshold is chosen, regardless of the propensity of the medium to deform.

A typical law description consists in considering a cubic evolution of the parameter ($\beta = 3$). Regarding the multiplying coefficient θ, a first approximation[18] would be $\theta = 2\,.\,10^{10}$. Figure 10 shows the evolution tendency from a theoretical point of view.

---

[17] *The total equivalent strain ε_{eq} is defined using the strain tensor ε_{ij}:* $\varepsilon_{eq} = \sqrt{\frac{2}{3}\,\varepsilon_{ij}\varepsilon_{ij}}$.

[18] *Considering strain values to range between* $[10^{-4} - 10^{-2}]$.

A first estimation of $\hat{\varepsilon}_{thr}$ can be achieved by simulating a first time until the excavation phase only, using the parameters mentioned above, but without any threshold: $t = -2\,days$, $\hat{\varepsilon}_{eq}^{thr} = 0$. Referring to Figure 53 (right) for the position of each cross section, Figure 56 shows that the strain becomes higher vertically at approximately 1 m from the rock wall. At this distance, the value of $\hat{\varepsilon}_{eq}$ is around $2\,.10^{-3}$ to $3\,.10^{-3}$ [−]. Let us note that the differences between the vertical cross sections (1-1 and 5-5) are linked to the geometry of the gallery. Let us also remind that the concrete slab is only installed from day 36.

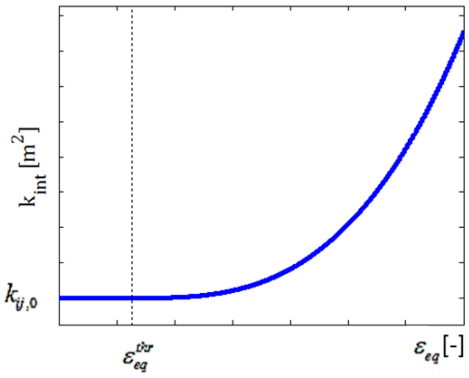

Figure 55: Theoretical evolution of the intrinsic permeability (Formulation 1).

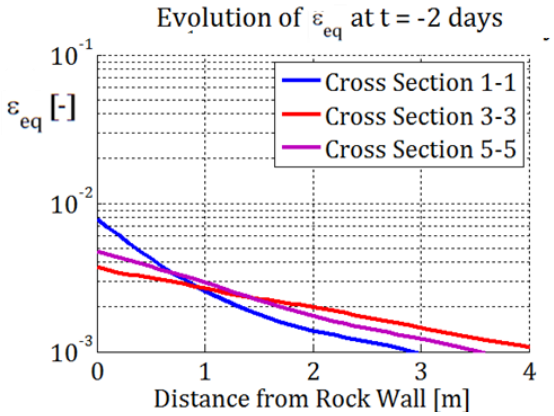

Figure 56: Evolution of the total equivalent strain at the end of excavation (day -2). Cross sections colours are in accordance with Figure 53 (right).

In addition to the threshold value, the main parameters of the simulation are listed in Table 17 here below.

$\boldsymbol{\theta}$ [−]	$\boldsymbol{\beta}$ [−]	$\hat{\boldsymbol{\varepsilon}}_{\boldsymbol{eq}}^{\boldsymbol{thr}}$ [−]
$2\,.10^{10}$	3	$2.7\,.10^{-3}$

Table 17: Evolution of permeability – Formulation 1: Set of main parameters #1.

Figure 56 confronts the numerical water pressures with the experimental measurements taken in the SDZ drills (positioned according to Figure 52). Nonetheless, since the sensors cannot measure negative values of water pressure, they are not able to characterise the desaturation of the rock. As a result, the experimental measures which should supposedly be negative (i.e. from sensors located close to the rock wall) are instead displayed with values close to 0 (cf. Appendix 8.2). This observation justifies the choice to not represent the negative values of water pressure obtained numerically. In this way, the comparisons are more conspicuous.

The numerical results exhibited on Figure 56 show pressures which are overestimated compared to the experimental data's, especially regarding the measurements close to the rock wall. In contrast, the values far from the gallery (i.e. beyond 9 m from the rock wall, cf. SDZ1244 drill) match quite well the experimental curves. This implies that the influence due to the variation of permeability does not (and does not need to) extend that far in the argillite.

The observed overestimation suggests the necessity to increase the coefficient θ of Formulation 1, so that the intrinsic permeability can further increase. However, bearing in mind that this property can evolve by up to 3 orders of magnitude only, we have to avoid obtaining too high values. This constraint leads to developing a new formulation with a limit value.

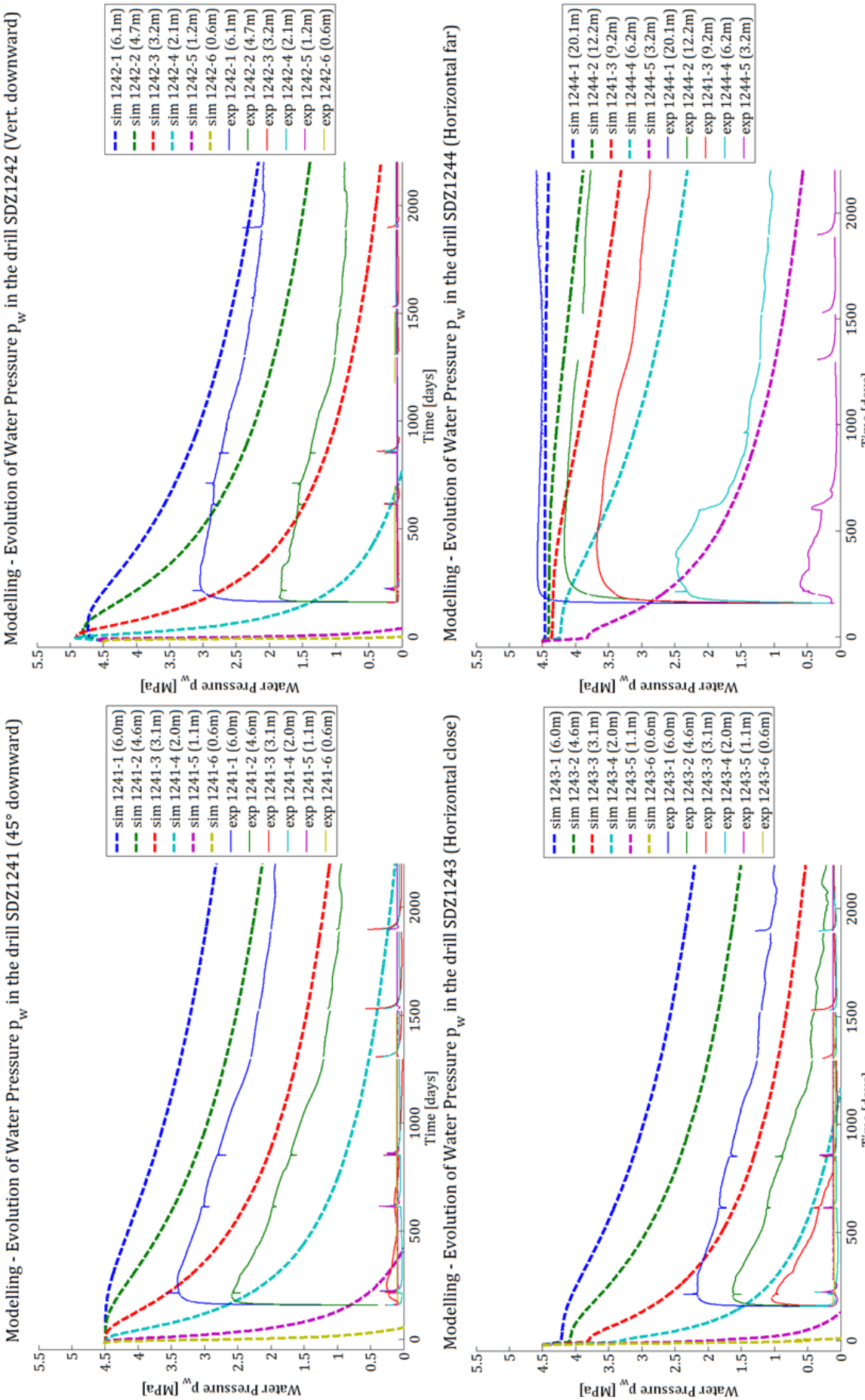

Figure 57: Modelling – Formulation 1: Evolution of Water Pressure in the SDZ drills (located in accordance to Figure 52). Comparison between the numerical results (dashed lines) and the experimental measures (solid lines). Set of parameters #1 (Table 17).

B. Considering the Total Equivalent Strain (Formulation 2)

The necessity of increasing the coefficient θ suggests imposing a limit value of the intrinsic permeability, thus avoiding too high values of that parameter. Formulation 2 is similar to the first one, but adds a second threshold ε_{eq}^{max} above which the permeability remains constant. The exponent '*-max*' is added to differentiate it from ε_{eq}^{thr}.

FORMULATION 2

$$\begin{aligned} &if\ \varepsilon_{eq} \le \varepsilon_{eq}^{thr}: && k_{ij} = k_{ij,0} \\ &if\ \varepsilon_{eq}^{thr} < \varepsilon_{eq} \le \varepsilon_{eq}^{max}: && k_{ij} = k_{ij,0}\left(1 + \theta\,.\left(\varepsilon_{eq} - \varepsilon_{eq}^{thr}\right)^{\beta}\right) \\ &if\ \varepsilon_{eq}^{max} < \varepsilon_{eq}: && k_{ij} = k_{ij,0}\left(1 + \theta\,.\left(\varepsilon_{eq}^{max} - \varepsilon_{eq}^{thr}\right)^{\beta}\right) \end{aligned} \qquad \textbf{(55)}$$

With $\varepsilon_{eq} = \sqrt{\frac{2}{3}\,\varepsilon_{ij}\varepsilon_{ij}}$.

The upper limit is chosen in such a way that the maximal value of the intrinsic permeability can be at most 1 000 times bigger than its initial value: $k_{max} = 1\,000 * k_{ij,0}$. The parameters used for the simulation are the same as the previous case (cf. Table 17), but with a higher value of the coefficient θ and the additional value of ε_{eq}^{max} (Table 18).

$\boldsymbol{\theta}$ [−]	$\boldsymbol{\beta}$ [−]	$\boldsymbol{\varepsilon_{eq}^{thr}}$ [−]	$\boldsymbol{\varepsilon_{eq}^{max}}$ [−]
$2\,.\,10^{12}$	3	$2.7\,.\,10^{-3}$	$3.5\,.\,10^{-3}$

Table 18: Evolution of permeability – Formulation 2: Set of main parameters #2.

The theoretical evolution of this formulation is given at Figure 58 and shows a horizontal plateau after the maximal value of strain ε_{eq}^{max}.

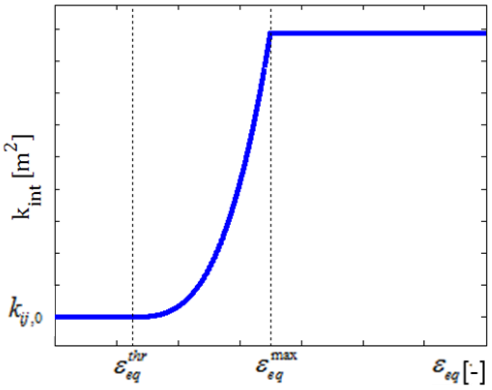

Figure 58: Theoretical evolution of the intrinsic permeability (Formulation 2).

Figure 59 compares the results of this second formulation with the ones belonging to Formulation 1. Let us remark that since the observations are valid for all the drills, the figure only displays the results at the horizontal drill (SDZ1243, cf. Figure 52). It shows that the water pressures close to the gallery are less important than in the previous case. Still, the numerical values remain overestimated and the observed decrease diminishes as we go further away from the gallery.

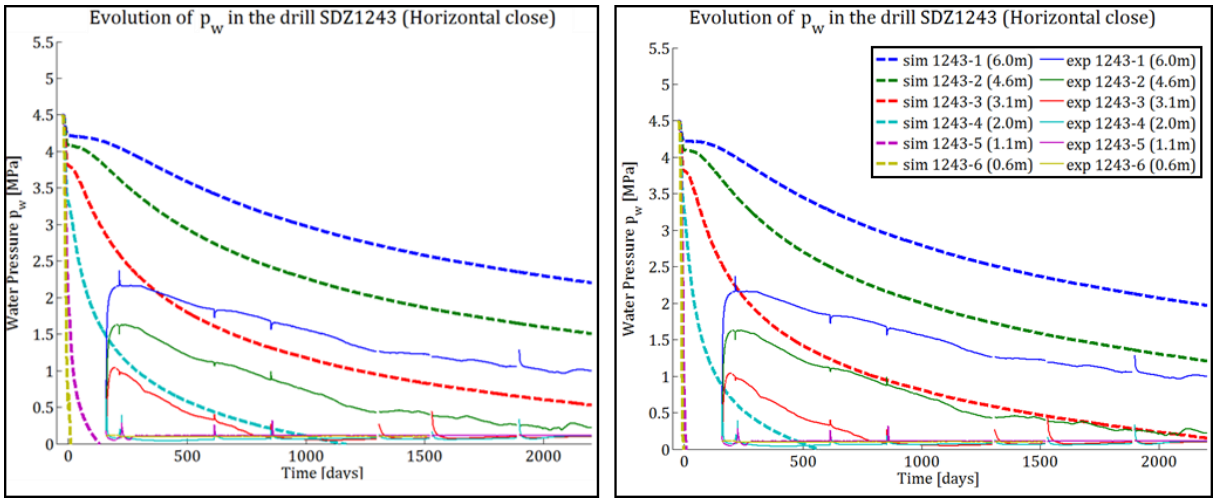

Figure 59: Modelling – Formulation 1 (left) and Formulation 2 (right): Evolution of Water Pressure in the SDZ1243 drill (horizontal close). The numerical results are represented in dashed lines and the experimental measures in solid lines.

The observations regarding Figure 59 are related to the EDZ. As a matter of fact, there are 2 major problems to this formulation. The first one is the decrease of the permeability profile with respect to time, while the second problem refers to the fact that the EDZ does not extend as desired. Rather than immediately tackling both problems simultaneously, the approach of this work is to deal with one aspect at first and to add afterwards the solution obtained for the second aspect. Therefore, this section only brings up the first problem, whereas the second one is reintroduced at the end of the next section.

As of now, the water pressures were confronted with the experimental results. Alternatively, to avoid showing numerous water pressure graphs, the following developments focus on permeability profiles (using radial sections, cf. Figure 53 right).

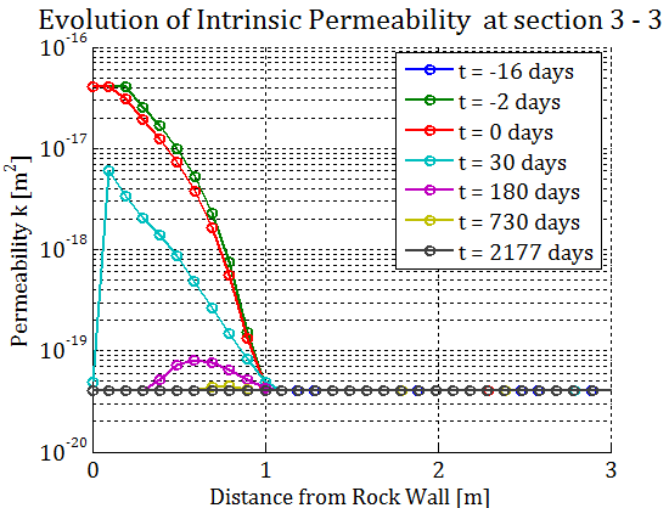

Figure 60: Modelling – Formulation 2: Evolution of the intrinsic permeability at several moments of the simulation, with respect to the horizontal radial distance (cross section 3-3).

According to [CRUCHAUDET, et al., 2010b], permeability measurement campaigns realised in August 2009, November 2009 and May 2010[19] concluded, among other things, that the permeability profile remains unchanged during this period. From the modelling point of view, the campaigns took place at approximatively 210, 300 and 500 days after the beginning of the ventilation test (day 0: 15/01/2009, cf. section 5.1.3D).

The results obtained with Formulation 2 are in contradiction with this observation. The several colour curves on Figure 60 show that the permeability starts decreasing right after the excavation (day -2). Indeed, the red curve (day 0) is already below the green one (end of excavation). This fall of permeability is even more noticeable at day 30 and it can also be observed that after day 180, the permeability through the whole section is almost brought back to its original value. This is caused by the progressive desaturation of the rock under the influence of the ventilation test. As a result, there is a necessity to impose an additional condition, which suggests proposing a new formulation.

C. Considering the Total Equivalent Strain (Formulation 3)

Following Equation 55, if ε_{eq} decreases, k_{ij} could decrease as well. To avoid that, we consider that the intrinsic permeability at a given time t is the maximum between the current value k_{ij}^{t} and the one at the previous time step $k_{ij}^{t-\Delta t}$. Formulation 3 is given as followed:

FORMULATION 3

$$\begin{aligned} &if\ \varepsilon_{eq} \le \varepsilon_{eq}^{thr}: && k_{ij} = k_{ij,0} \\ &if\ \varepsilon_{eq}^{thr} < \varepsilon_{eq} \le \varepsilon_{eq}^{max}: && k_{ij} = k_{ij,0}\left(1 + \theta\,.\left(\varepsilon_{eq} - \varepsilon_{eq}^{thr}\right)^{\beta}\right) \\ &if\ \varepsilon_{eq}^{max} < \varepsilon_{eq}: && k_{ij} = k_{ij,0}\left(1 + \theta\,.\left(\varepsilon_{eq}^{max} - \varepsilon_{eq}^{thr}\right)^{\beta}\right) \end{aligned} \qquad \textbf{(56)}$$

$$k_{ij}^{t} = \max\left(k_{ij}^{t-\Delta t}, k_{ij}^{t}\right) \qquad \textbf{(57)}$$

For this formulation, 2 sets of parameters are presented (Table 19). Although their calibration is skipped (to avoid redundancy), the key idea was to keep the values used in the previous case (Table 18) and vary one parameter. The set #3A changes the upper limit whereas the set #3B modifies the value of the lower limit.

	$\boldsymbol{\theta}$ [−]	$\boldsymbol{\beta}$ [−]	$\boldsymbol{\varepsilon_{eq}^{thr}}$ [−]	$\boldsymbol{\varepsilon_{eq}^{max}}$ [−]
A	$2\,.\,10^{12}$	3	$2.7\,.\,10^{-3}$	$4.5\,.\,10^{-3}$
B	$2\,.\,10^{12}$	3	$1.64\,.\,10^{-3}$	$3.5\,.\,10^{-3}$

Table 19: Evolution of permeability – Formulation 3: Sets of main parameters #3A and #3B.

Figure 61 shows the permeability profiles for the 5 radial sections that were detailed on Figure 53 (right). Let us remark that the horizontal section is represented by the red curve. Concerning the vertical section, it is represented upwards by the blue curve and downwards by the purple one. Because the EDZ is supposed to remain the same (or at least to vary slightly), we decide to look at the end of the simulation (day 2177). In order to avoid any influence of the concrete slab (casted on day 36) on the behaviour of the rock formation, we solely focus on the radial section going upwards (i.e. cross-section 1-1).

[19] *Further campaigns are not available.*

The black circles on the figure refer to the dimensions of the EDZ (inner and outer zones) determined experimentally in [CRUCHAUDET, et al., 2010b]. They indicate that the graphs corresponding to the sets #3A and #3B represent quite well the extension of the zone horizontally OR vertically (respectively), but not both at the same time.

This observation refers to the second major problem mentioned in the previous section, which is about the extension of the EDZ. Indeed, when matching the horizontal dimensions (Figure 61 left, set #3A), the EDZ simulated is too short vertically (nothing at 3.1 m from the gallery). Moreover, if we try to correspond the permeability profile vertically (Figure 61 right, set #3B), the EDZ is too stretched in the perpendicular direction, i.e. the red curves starts almost at 4.5 m away (which is much farther than the observed 1.1 m)[20].

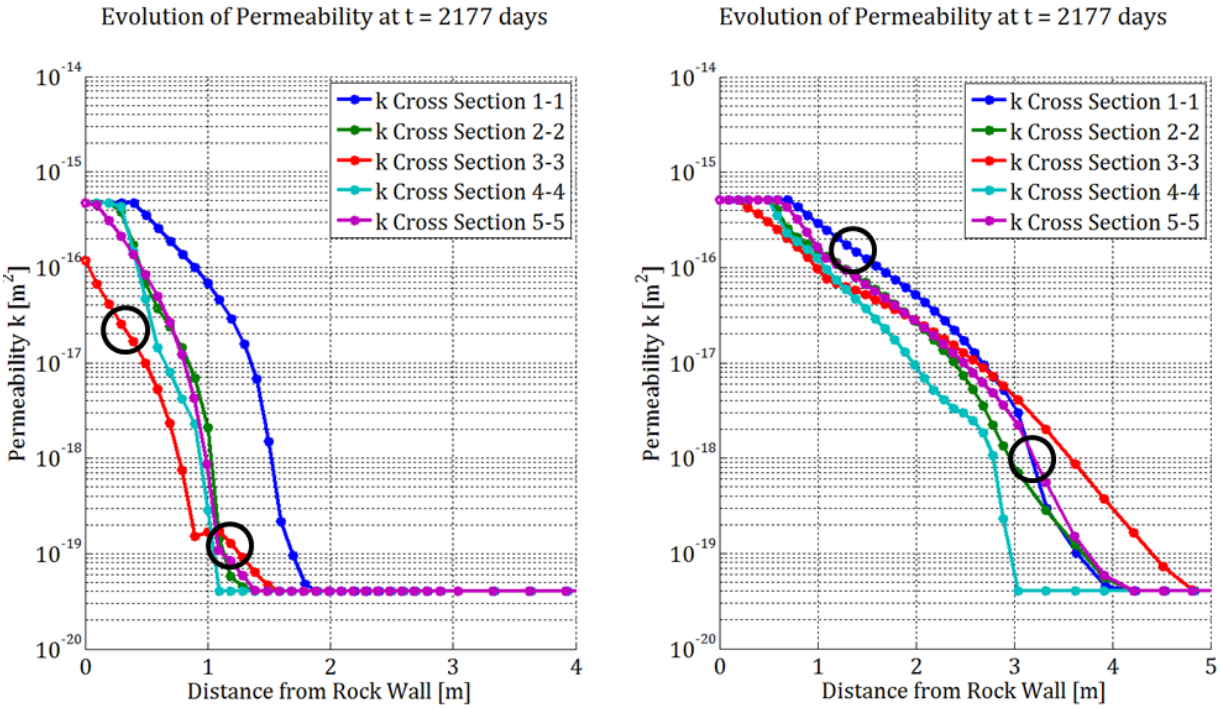

Figure 61: Modelling – Formulation 3: Evolution of the intrinsic permeability along the radial sections (cf. Figure 53 right) using sets of parameters #3A (left) and #3B (right). Black circles refer to the dimensions of the EDZ determined experimentally.

In fact, as the rock formation is supposed to be homogenous, the only aspect which could differentiate the development of the SDZ horizontally and vertically is related to the anisotropic initial stresses ($\sigma_{v;0} = 12.0\ MPa$ and $\sigma_{H;0} = 1.3\ \sigma_{v;0} = 15.6\ MPa$). The following section discusses the possibility to consider a parameter (other than the strain) that could quantify the damage of the rock and subsequently proposes a new formulation capable of correctly representing the EDZ.

[20] *This reasoning can be brought further. Indeed, Figure 56 actually shows that there is a distance beyond which the horizontal (total equivalent) strain becomes greater than the vertical one. Consequently, if the threshold value ε_{eq}^{thr} were to be lowered until a point where this inversion of tendency would be noticeable enough, it would result in having an EDZ wider horizontally. In other words, its shape would be in contradiction with what has been experimentally observed (cf. Figure 54). To support this explanation, we have thereby chosen to use the set of parameters #3B.*

D. Considering the Ratio of Plasticity (Formulation 4)

In the convergence/confinement theory (cf. section 5.1.3B), the orthoradial stress σ_θ increases as the deconfinement rate λ gets closer to 1, while the radial stress σ_ρ is lowered to 0. This may lead to the yielding of the rock surrounding the gallery. Referring to Figure 62, the rock located along the vertical axis (i.e. along $\hat{y}$) is more prone to yielding than the one positioned along the horizontal radial section (i.e. along $\hat{x}$).

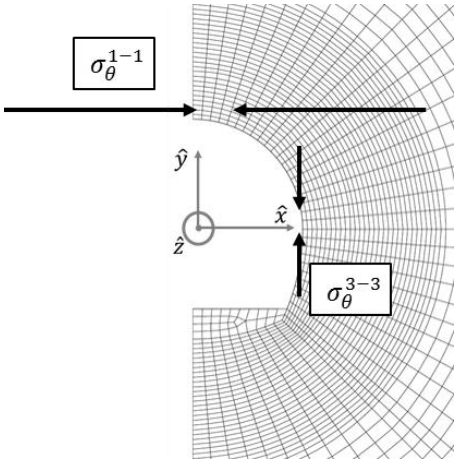

Figure 62: Qualitative representation of the stress state within the rock wall at the end of the excavation. The black arrows indicate the importance of the orthoradial stresses in the vertical and horizontal directions.

Therefore, we introduce the concept of yield index and define it as a logical value (0 or 1) which indicates whether the material has entered into plasticity or not. It is now possible to analyse the extent of the plastic zone.

This zone is the most critical right at the end of the excavation. Indeed, when the ventilation test begins, the subsequent fall of water pressure increases the effective stresses within the medium. As a result, the increase of the mean stress p suggests that the stress state is shifted to the right when referring to the $p-q$ plane (Figure 35, p.30). We are thus further from the yielding limit. In other words, the desaturation of the rock formation is unfavourable to the development of a yielding zone.

Using the set of parameters #3A (cf. Table 19), Figure 63 (left) shows the plastic zone at the end of the excavation (day -2) for a cohesion $c = 4.5\ MPa$ (which corresponds to the default value presented in Table 13, section 5.2.2B). The result supports the explanation made at the end of the previous section: because of the anisotropic initial stresses, the zone is more extended vertically than horizontally[21]. Yet, it does not develop as much as desired. The dimensions aimed are 3.1 m vertically and 1.1 m horizontally but in contrast the zone does not spread farther than approximately 1.5 m and 0.6 m (respectively).

A solution to this problem is to decrease the value of the cohesion, so that the yield limit of the material is lowered (cf. Drücker-Prager criterion, Equation 35). Figure 63 (right) shows that with $c = 4.0\ MPa$, the plastic zone has gotten bigger, but this difference is hardly noticeable. In order to reach the wanted dimensions, this method would require strongly decreasing the values of the mechanical parameters. This option is not conceivable in this work if we want to remain consistent with the parameters calibration realised in Chapter 4.

[21] *Some disparities are observable between the upper and lower half of the domain due to the geometry of the gallery.*

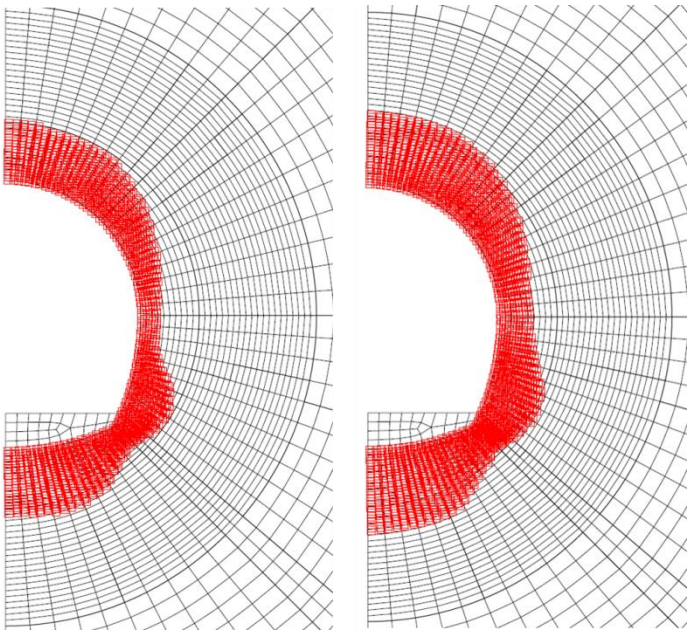

Figure 63: Modelling: Extent of the plastic zone at the end of the excavation.
Set of parameters #3A (Table 19), with c = 4.5 MPa *(default value, left) and* c = 4.0 MPa *(right).*

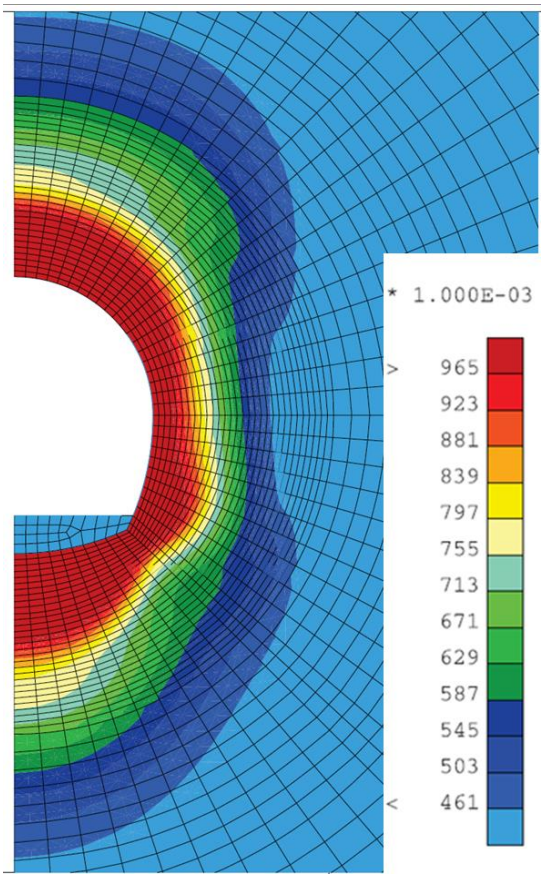

Figure 64: Modelling: Evolution of the ratio of plasticity at the end of the excavation (right).
Set of parameters #3A (Table 19), with c = 4.5 MPa *(default value).*

Alternatively, we introduce another concept: the ratio of plasticity Υ, also called the yield ratio or the reduced deviatoric stress. It is defined as the ratio between the current deviatoric stress q and the one corresponding to the yielding limit q^{pla}: $\Upsilon = \mathrm{q}/\mathrm{q}^{\mathrm{pla}}$.

Instead of displaying the yield index as on Figure 63 left, Figure 64 shows Υ with the same configuration, that is to say using the set of parameters #3A and the default value of the cohesion $c = 4.5\ MPa$. The several zones delimited by isolines of Υ have a similar shape to the EDZ described experimentally (cf. Figure 54). As a result, a new formulation consists in adapting Formulation 3 using the ratio of plasticity rather than the equivalent total strain.

FORMULATION 4

$$\begin{aligned} &if\ \Upsilon \le \Upsilon^{thr}: && k_{ij} = k_{ij,0} \\ &if\ \Upsilon^{\mathrm{thr}} < \Upsilon\ and\ \varepsilon_{eq} \le \varepsilon_{eq}^{max}: && k_{ij} = k_{ij,0}\left(1 + \theta\,.\left(\Upsilon - \Upsilon^{\mathrm{thr}}\right).\left(\varepsilon_{eq}\right)^{\beta}\right) \\ &if\ \Upsilon^{\mathrm{thr}} < \Upsilon\ and\ \varepsilon_{eq}^{max} < \varepsilon_{eq}: && k_{ij} = k_{ij,0}\left(1 + \theta\,.\left(\Upsilon - \Upsilon^{\mathrm{thr}}\right).\left(\varepsilon_{eq}^{max}\right)^{\beta}\right) \end{aligned} \quad \textbf{(58)}$$

$$k_{ij}^{t} = \max\left(k_{ij}^{t-\Delta t}, k_{ij}^{t}\right) \quad \textbf{(59)}$$

Equation 56 is modified in such a way that the lower limit (i.e. threshold value) is conditioned by the ratio of plasticity (noted Υ^{thr}), whereas the upper limit still takes into account a maximum value of strain ε_{eq}^{max}. The evolution of the intrinsic permeability k_{ij}remains cubic with respect to the total equivalent strain ε_{eq} (Figure 65).

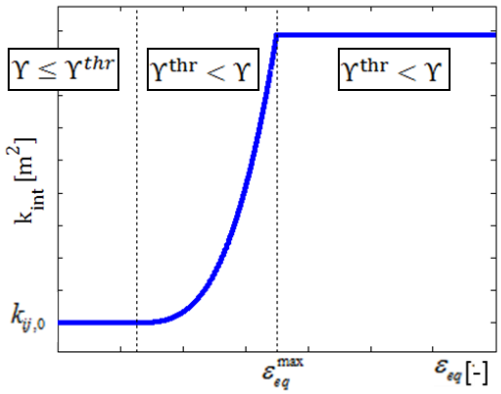

Figure 65: Theoretical evolution of the intrinsic permeability (Formulation 4).

Similarly to the first case (cf. section 5.3.1A), the value of the lower limit Υ^{thr} is estimated by looking at the results (at the end of the excavation phase, day -2) of a first simulation without any minimal threshold. Let us remark that the other parameters used for this first estimation are taken from Table 18 (set of parameters #2)[22].

[22] *Even though they are not relevant, since the main parameters that influence the behaviour of the rock during the excavation are likely to be mechanical.*

Figure 66 shows the evolution of the ratio of plasticity along the vertical and horizontal radial distances, at several moments of the excavation. The black lines delimit the dimensions of the EDZ (outer and inner zones) respectively for both directions. Referring to the solid black lines, the threshold value can be fixed when looking at their intersection with the curves of Υ (the green one). The intersection takes place a bit lower than 0.6 vertically, whereas it is a bit higher than 0.6 horizontally. Thus, the chosen default value of $\Upsilon^{\mathrm{thr}} = 0.6$ is a good compromise between what happens in both directions.

Let us note that almost all the rock located inside the inner zone of the EDZ (dashed lines) has reached the yielding limit. More specifically, the ratio of plasticity within this zone is approximately greater than 0.9 in both directions.

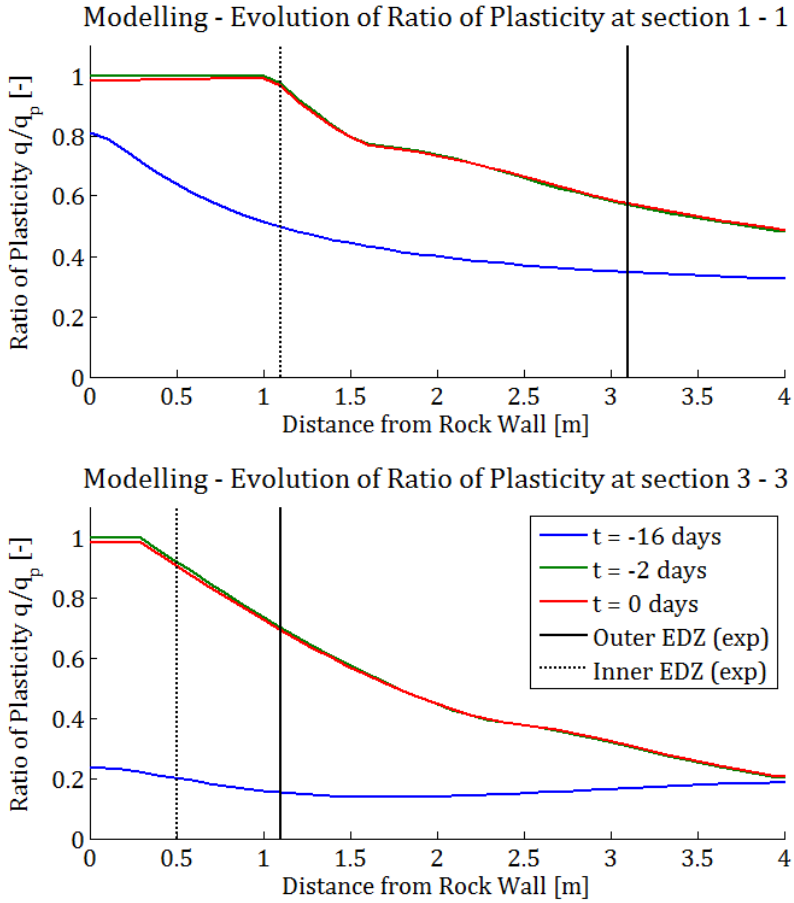

Figure 66: Modelling: Evolution of the ratio of plasticity at several moments of the excavation, with respect to the vertical (cross section 1-1, up) and to the horizontal radial distances (cross section 3-3, down).

The parameters used in this formulation are listed in Table 29 below.

$\boldsymbol{\theta}$ [−]	$\boldsymbol{\beta}$ [−]	Υ^{thr} [−]	ε_{eq}^{max} [−]
$2\,.\,10^{10}$	3	0.6	$3.5\,.\,10^{-3}$

Table 20: Evolution of permeability – Formulation 4: Set of main parameters #4.

Referring to the cross sections (1-1) and (3-3) on Figure 67 (which are placed respectively in the vertical and horizontal directions), the black circles highlight the fact that Formulation 4 gives us a good representation of the EDZ determined experimentally.

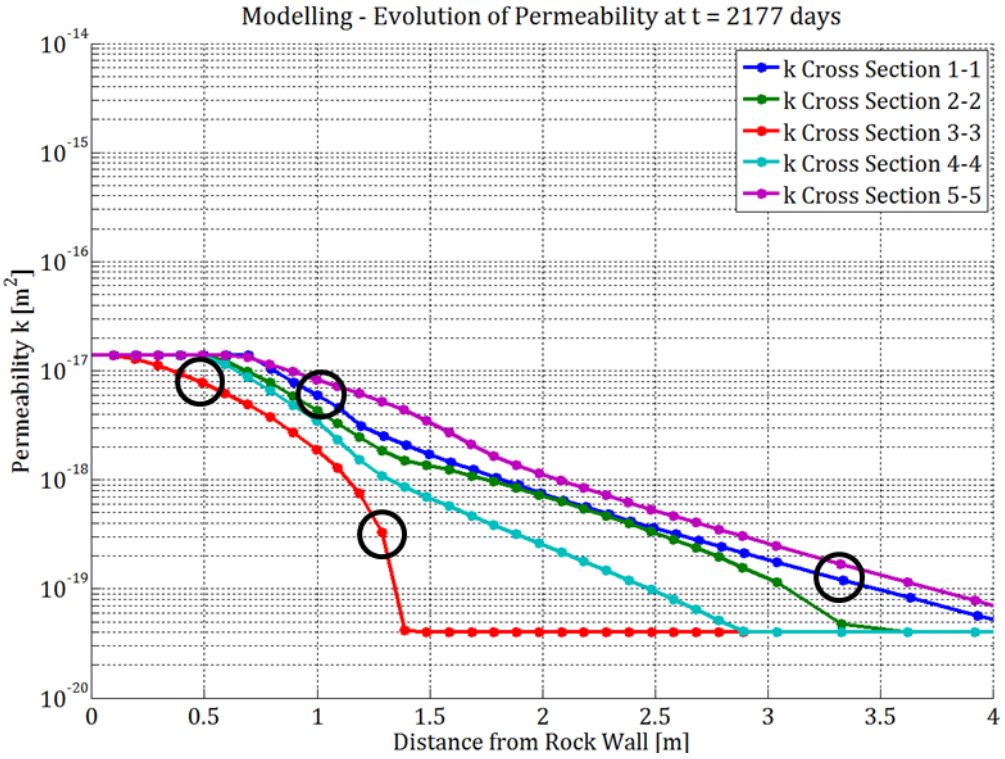

Figure 67: Modelling – Formulation 4: Evolution of the intrinsic permeability along the radial sections (cf. Figure 53 right) using set of parameters #4. Black circles refer to the dimensions of the EDZ determined experimentally.

As the proportions between the extent of the vertical and horizontal zones are respected, we can now confront the water pressure results (Figure 68). As expected, their values have greatly decreased compared to the first case (Formulation 1). Several observations can be made.

- The numerical values corresponding to the drill at 45° (SDZ1241) match the experimental measurements.
- Regarding the vertical drill (SDZ1242), the water pressures are this time far below the measured data's. An improvement has to be done.
- The horizontal close drill (SDZ1243) shows that the water pressures at the two farthest points are still a bit overestimated (green and blue curves).
- In the horizontal far drill (SDZ1244), the numerical results are well represented, with some disparities at certain points of the drills, notably the light blue curve in the SDZ1244 drill (at 6.2 m away from the gallery). This abnormality was also pointed out in previous reports [CHARLIER, et al., 2013b].

These observations mainly refer to the values after 500 days. Indeed, the values measured on site before that suggest a latency period of the sensors.

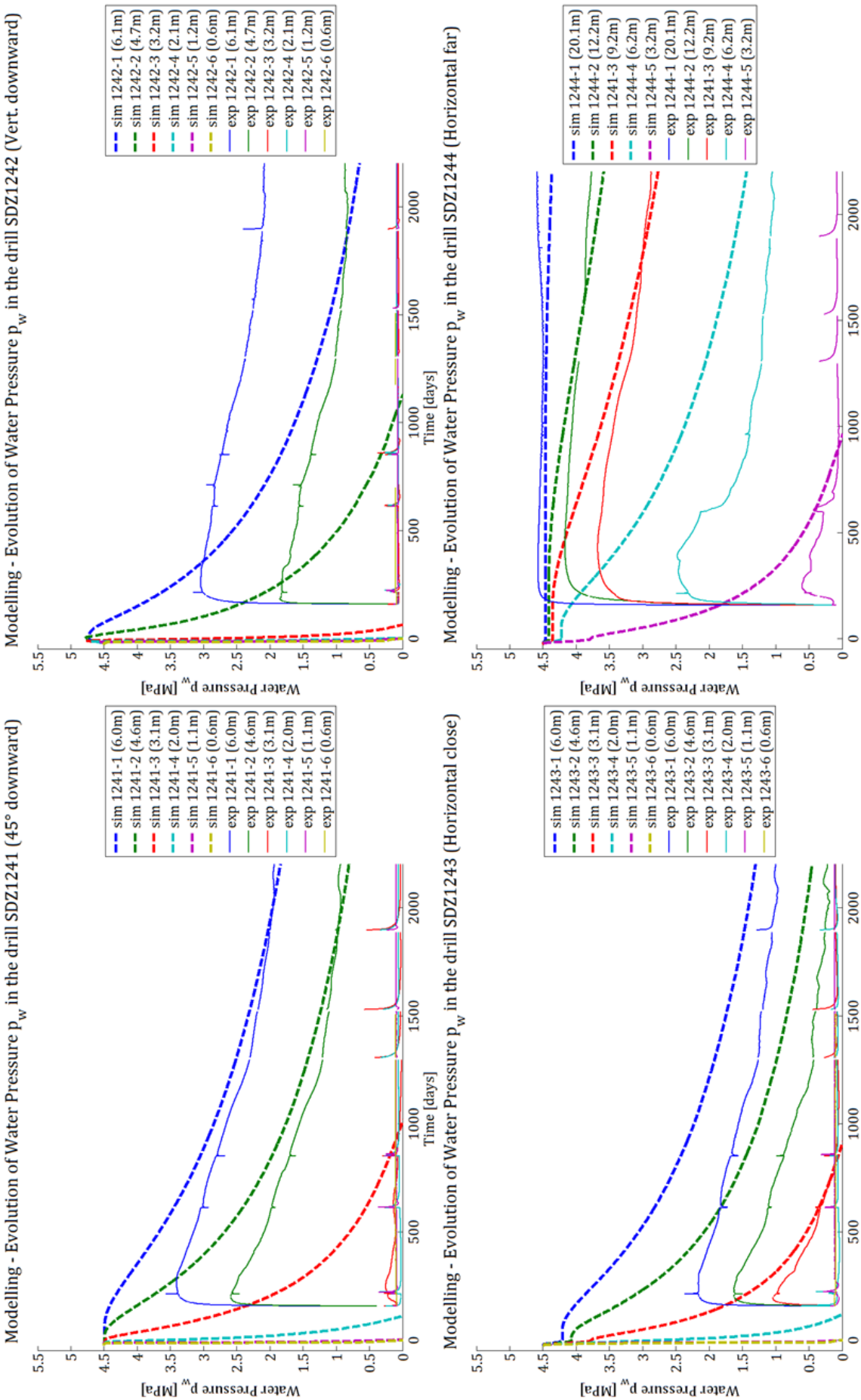

Figure 68: Modelling – Formulation 4: Evolution of Water Pressure in the SDZ drills (located in accordance to Figure 52). Comparison between the numerical results (dashed lines) and the experimental measures (solid lines). Set of parameters #4 (Table 20).

Aside from what happens in the vertical drift, this last formulation (Formulation 4) was able to solve the two major problems linked to Formulation 2 (section 5.3.1B), which were the decrease of the permeability profile with respect to time and the fact that the EDZ did not extend as desired[23].

Nonetheless, as mentioned in the observations, an improvement has to be done regarding the SDZ1242 drill. The literature actually proposes to distinguish the horizontal intrinsic permeability from the vertical one. Consequently, the next section briefly describes this modification before comparing the results.

E. Considering Anisotropy of the Initial[24] Permeability (Formulation 4)

In section *3.1.2A Advection of Liquid Phase*, Darcy's law (Equation 6) was described by means of a scalar value of the intrinsic permeability k_{int}. When introducing the concept of the anisotropy of this parameter, we use the general expression of the intrinsic permeability tensor $\underline{\boldsymbol{k}}_{int}$, given here below:

$$\underline{\boldsymbol{k}}_{int} = \begin{bmatrix} k_{xx} & k_{xy} & k_{xz} \\ k_{yx} & k_{yy} & k_{yz} \\ k_{zx} & k_{zy} & k_{zz} \end{bmatrix} \qquad (60)$$

As a reminder, the gallery is placed along the $\hat{z}$ axis (cf. Figure 46 and Figure 62). The reports of [CHARLIER, et al., 2013b] and [PARDOEN, et al., 2015] suggest the following values for the intrinsic permeability:

$$k_{hor} = k_{xx} = 4.00\ 10^{-20}$$
$$k_{ver} = k_{yy} = 1.33\ 10^{-20}$$

Thus, the vertical permeability is 3 times lower than the horizontal one. The will to decrease the vertical permeability is also justified by the underestimation of the water pressures in the vertical drill (SDZ1241 on Figure 68). The simulation is launched using the set of parameters #4 (Table 20), but this time, two values of intrinsic permeability are considered. Thus, Table 12 becomes:

Symbol	Name	Unit	Value
k_{hor}	Intrinsic Horizontal Permeability	m^2	$4\ 10^{-20}$
k_{ver}	Intrinsic Vertical Permeability	m^2	$1.33\ 10^{-20}$
φ	Porosity	–	0.173
m	Van Genuchten Coefficient	–	0.33
n	Van Genuchten Coefficient	–	1.49
P_r	Air Entry Value (V.G. parameter)	MPa	15
S_{max}	Maximal Saturation	–	1
S_{res}	Residual Saturation	–	0.01
τ	Tortuosity	–	0.25

Table 21: Hydraulic parameters of the argillite with anisotropy of the intrinsic permeability.

[23] *Both problems were respectively overcome by Equation 59 and Equation 58.*
[24] *We specify' initial' as we consider that the intrinsic permeability profiles can evolve with time.*

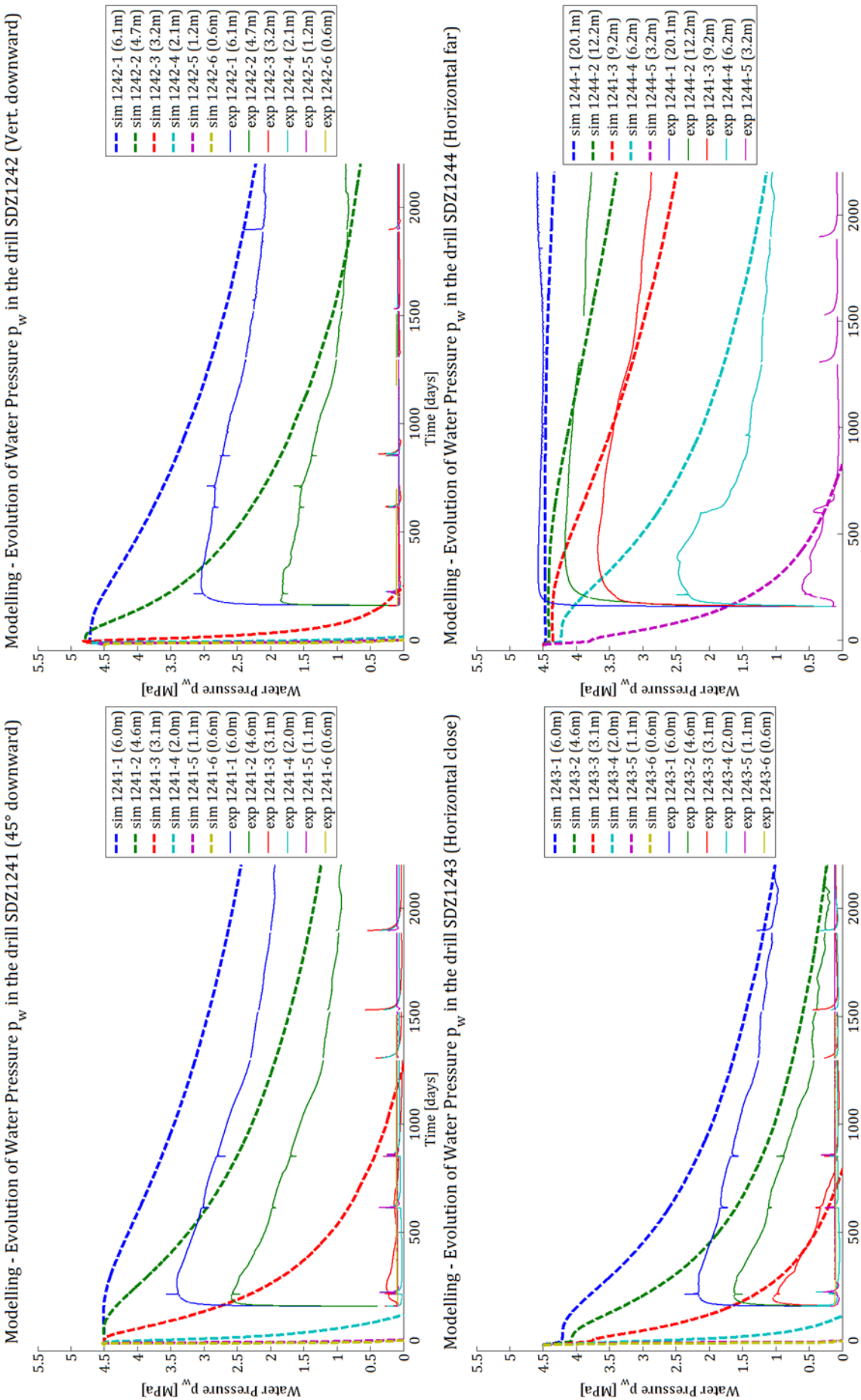

Figure 69: Modelling – Formulation 4 with $k_{xx} \neq k_{yy}$: Evolution of Water Pressure in the SDZ drills (located in accordance to Figure 52). Comparison between the numerical results (dashed lines) and the experimental measures (solid lines). Set of parameters #4 (Table 20).

Figure 69 shows the evolution of the water pressures in the SDZ drills. In comparison to Figure 68 and to the observations that were made, now it can be noted that:

- In the vertical drill (SDZ1242), the correspondence with the experimental measurements has been strongly improved.
- Horizontally (SDZ1243 and SDZ 1244), the water pressures have decreased a little more, which also improves the match.
- In contrast, in the drill at 45° (SDZ1241), the water pressures are slightly higher than the ones obtained using a unique value of permeability (section 5.1.3C). This will be discussed in section 5.3.3. In spite of that, the water pressures are still really close to the experimental data's.

Consequently, it can be concluded that Formulation 4 describes correctly the evolution of the permeability within the EDZ as well as the water pressures in the rock formation. Moreover, if the anisotropy of the intrinsic permeability is considered, the water pressures simulated give an even better correspondence with the experimental results.

Table 22 makes a recap of the parameters used in this last part (i.e. section *5.3.1E)*. The *final* set of parameters is named set #4.00 and is selected for the further developments.

Formulation	$\boldsymbol{\theta}$ $[-]$	$\boldsymbol{\beta}$ $[-]$	$\boldsymbol{\Upsilon^{thr}}$ $[-]$	$\boldsymbol{\varepsilon_{eq}^{max}}$ $[-]$	$\mathbf{k_{hor}}$ $[\mathbf{m^2}]$	$\mathbf{k_{ver}}$ $[\mathbf{m^2}]$
4	2.10^{10}	3	0.6	$3.5.10^{-3}$	$4 * 10^{-20}$	$1.33 * 10^{-22}$

Table 22: Evolution of permeability – FINAL set #4.00: Formulation 4 with anisotropy of the intrinsic permeability.

In the aim to characterise the EDZ, this part was essentially focused on what happens at the end of the excavation phase (day -2). The next section, dedicated to the analysis of the numerical results obtained from the final set #4.00 mentioned here above, concentrates more on the ventilation test.

5.3.2 Numerical Results Analysis – Ventilation Test

In continuity with the previous section devoted to the description of the evolution of permeability, the section 5.3.2 first treats about the hydraulic aspect. Additional remarks are made concerning the evolution of the EDZ and water pressures. After that, numerical results are compared to the experimental measures, alternately with the descriptions of several influences. This approach is also discussed in a part related to the mechanical parameters, and in one more focused on the water and vapour exchanges at the rock wall.

A. Hydraulic Parameters

Regarding the numerical results exposed so far, 3 main remarks need to be made. The first one is related to the water pressure measurements on the long term. Due to a continuous desaturation (with possible partial resaturation), the water pressure within the rock formation drops. This effect is directly (and thus strongly) felt when situated close to the gallery. With time, the desaturation should spread through the rock mass, and reach the far measure points. As a result, even the water pressures at those locations should also decrease (even if it starts in the long term).

However, the experimental curves do not seem to agree with this explanation (Figure 69). Instead, they tend to stabilise from around 1200 days onwards. This nearly horizontal progression affects the confrontation with the numerical results. Indeed, in some cases (SDZ1242 and SDZ1244), the numerical curves, which were originally higher than the measurements, can even go below the experimental ones.

This slope decrease occurs for all the curves, and is the most noticeable for far measures. In other words, the phenomenon also concerns the measure points located far away from the gallery (SDZ1244, horizontal far). This means that the calculated permeability profile inside the EDZ (which does not spread further than 2 m in that direction) is thus not the source causing the divergence between the experimental and the simulation results.

Alternatively, these differences suggest that the damaged rock close to the gallery can somehow avoid/limit the spread of the desaturation. This remark introduces the concepts of self-sealing and self-healing mentioned in other works ([BERNIER, et al., 2004], [CARIOU, 2010], [WANG, et al., 2013] and [CHARLIER, et al., 2013a]), but it is outside the scope of this work.

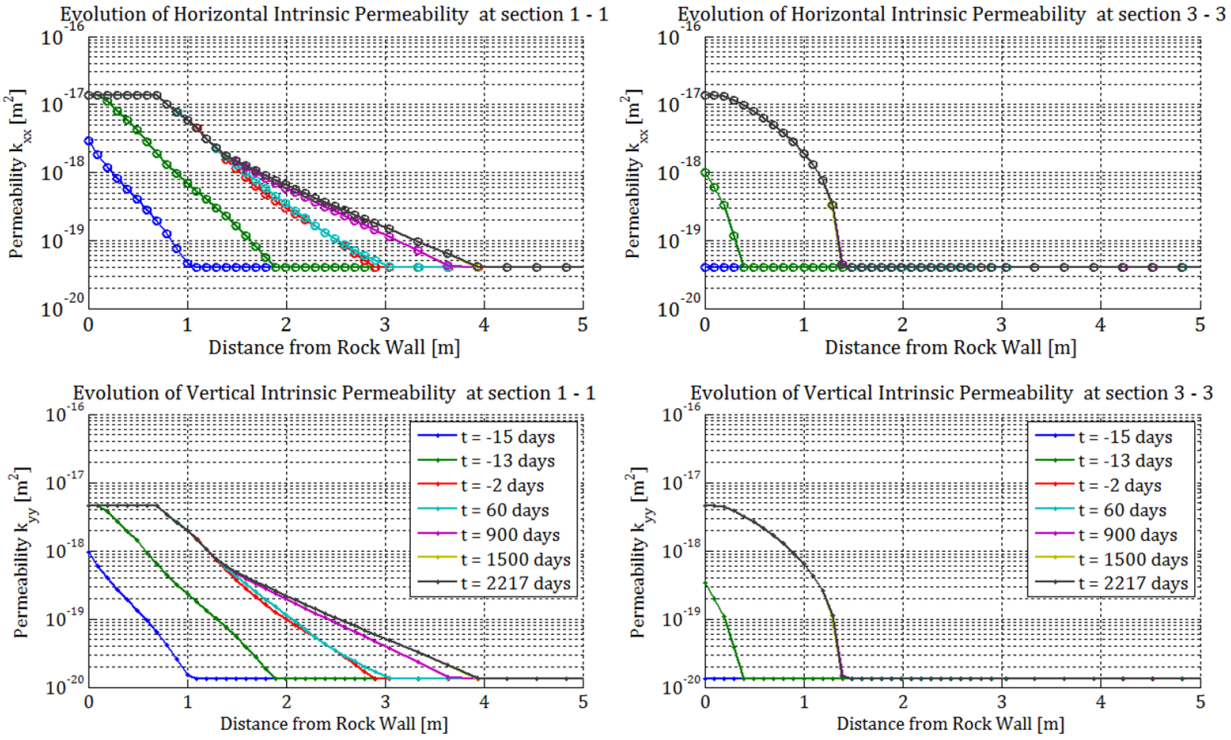

Figure 70: Modelling – Permeability profiles: Evolution of the intrinsic permeability along the vertical (left) and the horizontal (right) radial sections. Set of parameters #4.00. Colours refer to different moments of the simulation. Top figures correspond to k_{xx} *and bottom figures to* k_{yy}.

The second remark concerns the evolution of the EDZ. It was previously explained (cf. end of section 5.1.3B) that the zone is supposed to remain constant. Figure 70 shows that at the vertical radial section (1-1), the permeability profile can evolve up to 1 m farther from the gallery between the end of the excavation and the end of the simulation, whereas the profile does not change horizontally. Despite the fact that this extension is discussed in the following section 5.3.2B (as it is somehow linked to the stress state within the rock formation), let us point out the time scale in which this evolution took place. As a matter of fact, this period is much larger than the one of the experimental campaigns. Thus, in the case of a possible extension of the EDZ, Figure 70 highlights its progressive nature.

The last remark is related to the objectives of the work (cf. beginning of chapter 5). Indeed, one of the aims was to propose a formulation such that the hydraulic behaviour evolves in the same way regardless of the orientation. Actually, despite the introduction of the anisotropy of a hydraulic parameter, the objective is still valid since the evolution of the permeability does not depend on the initial values. Figure 70 shows that for a same radial section, the permeability profile is the same for both parameters k_{xx} and k_{yy}, except that the first one is shifted upwards compared to the second one.

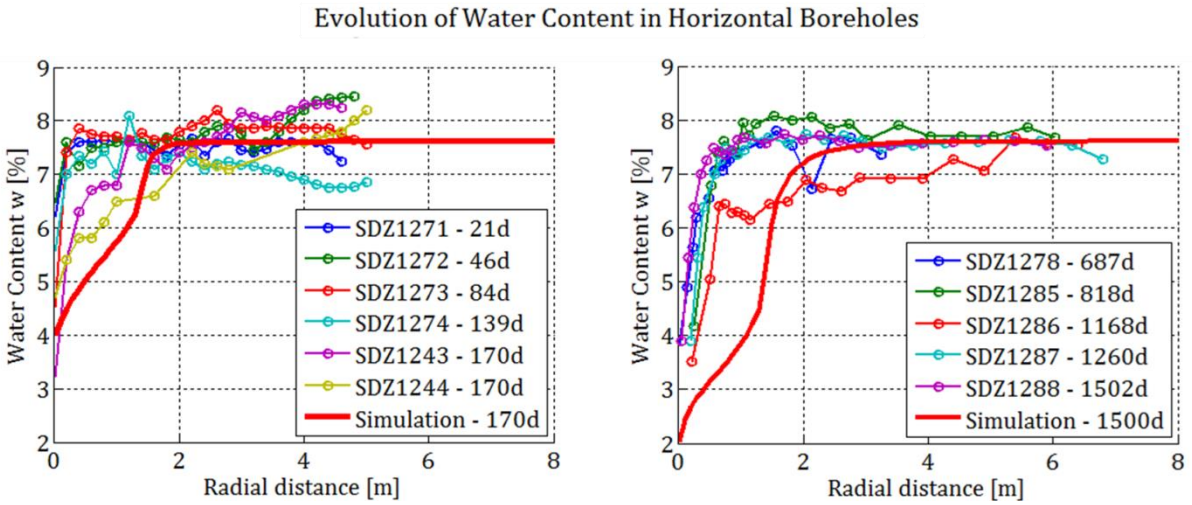

Figure 71: Modelling – Water Content: Evolution in horizontal drifts (or boreholes) on the short term (left) and on the long term (right). Set of parameters #4.00. Comparison with the experimental measures.

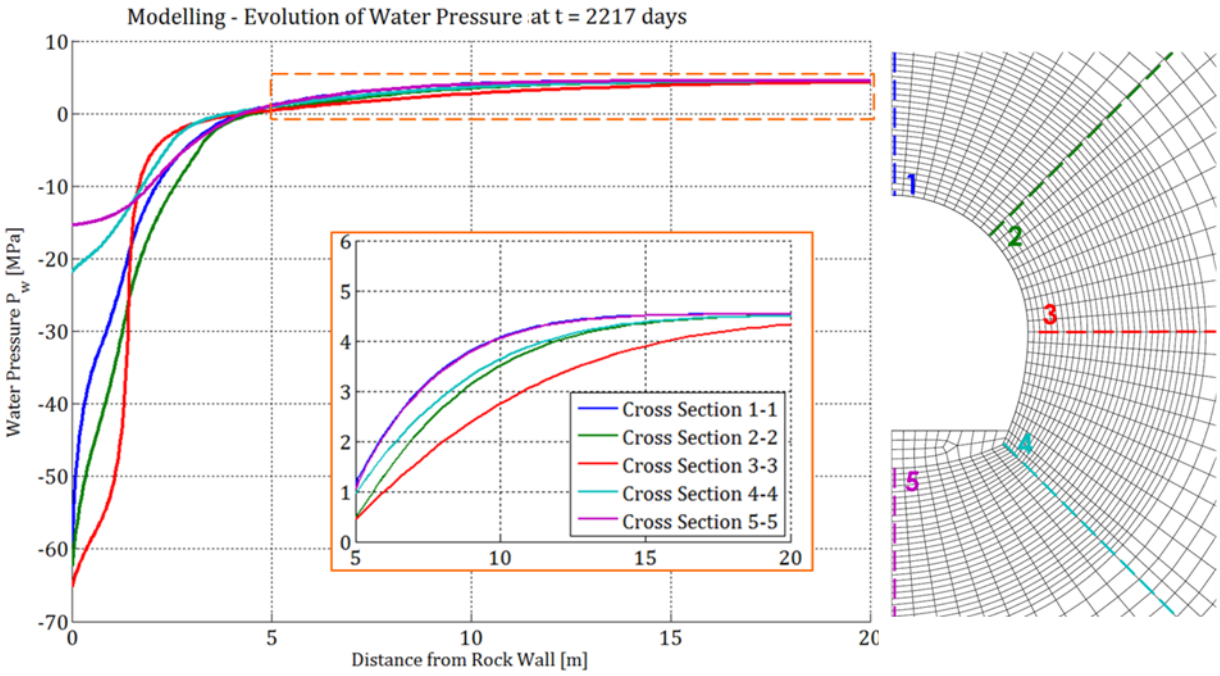

Figure 72: Modelling – Impact of the permeability profiles: Evolution of the water pressures along the radial sections. Set of parameters #4.00. Colours correspond to specific orientations. Zoom on the values beyond 5 m from the gallery.

Looking into the profiles of the water content (Figure 71) and the water pressure (Figure 73), let us first remark that the far boundary conditions do not influence what happens near the gallery, which means that the domain was correctly modelled.

Regarding the water content, Figure 71 compares the numerical profile with experimental data's (horizontally). The drainage within the EDZ seems to have been overestimated, since the water contents are much lower than the measurements. However, the argillite would normally be expected to become progressively unsaturated with time. This is actually not observed: short and long term experimental curves are quite similar. Moreover, a certain level of dispersion among the data's suggests that these results must be interpreted with care.

In addition to that, a desaturation front is noticeable in both figures. When zooming at the points beyond 5 m away from the gallery (Figure 73), we can see the impact of the drainage of the EDZ. Indeed, at the end of the simulation (day 2217), at a same distance from the gallery, the water pressures are lower horizontally (section 3-3). Furthermore, close to the rock wall, the drop of water pressure is more intense in that direction than elsewhere. As a result, the clearer the rupture between the damaged rock and the undamaged one (i.e. high difference of water pressure), the farther is the influence of the EDZ.

The curves corresponding to cross sections 4-4 and 5-5 are softer than the three others. This is due to the presence of the concrete slab. To highlight this effect, Figure 72 displays the evolution of water pressure at the rock wall with respect to time. Because the permeability of the concrete slab is lower than the one within the EDZ, this feature serves as a buffer zone. It limits the exchanges between the cavity of the gallery and the rock formation. Indeed, Figure 72 shows that once the concrete slab is casted, the water pressure at point 5 is varying much less than the other points located on an uncovered area of the rock wall. Consequently, it can easily be conceived that the water flows below the concrete are directed towards the uncovered zone, i.e. a little bit higher than point 4.

However, let us note that the permeability of concrete was fixed as such at the beginning of the simulation. More precise numerical results would require on site measurements of the concrete slab.

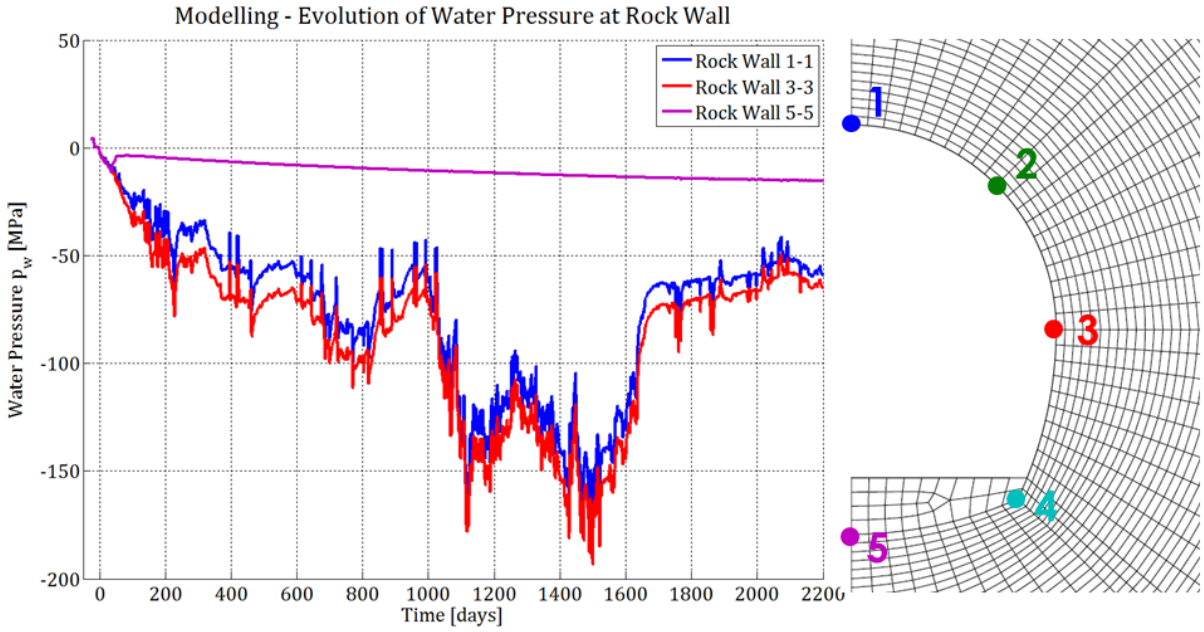

Figure 73: Modelling – Concrete Slab Effect: Evolution of the water pressures at the rock wall. Set of parameters #4.00. Colours correspond to specific locations on the wall.

These observations were briefly discussed in section 5.3.1C. As a matter of fact, they justify our choice to focus solely on the other directions for the following analyses.

B. Mechanical Parameters

The extension of the EDZ during the ventilation test that was noticed in section 5.3.2A is linked to the evolution of the stresses within the rock formation (Figure 74).

It was previously remarked that due to the progressive desaturation of the host formation, the effective stress increased subsequently (thus the need to prevent the permeability to decrease, cf. Equation 59). However, referring to the climatic conditions imposed in the gallery (Figure 51), the fluctuations[25] are such that partial resaturation may be possible. Therefore, the opposite effect to the one we prevented can occur, which is: a possible increase of the permeability.

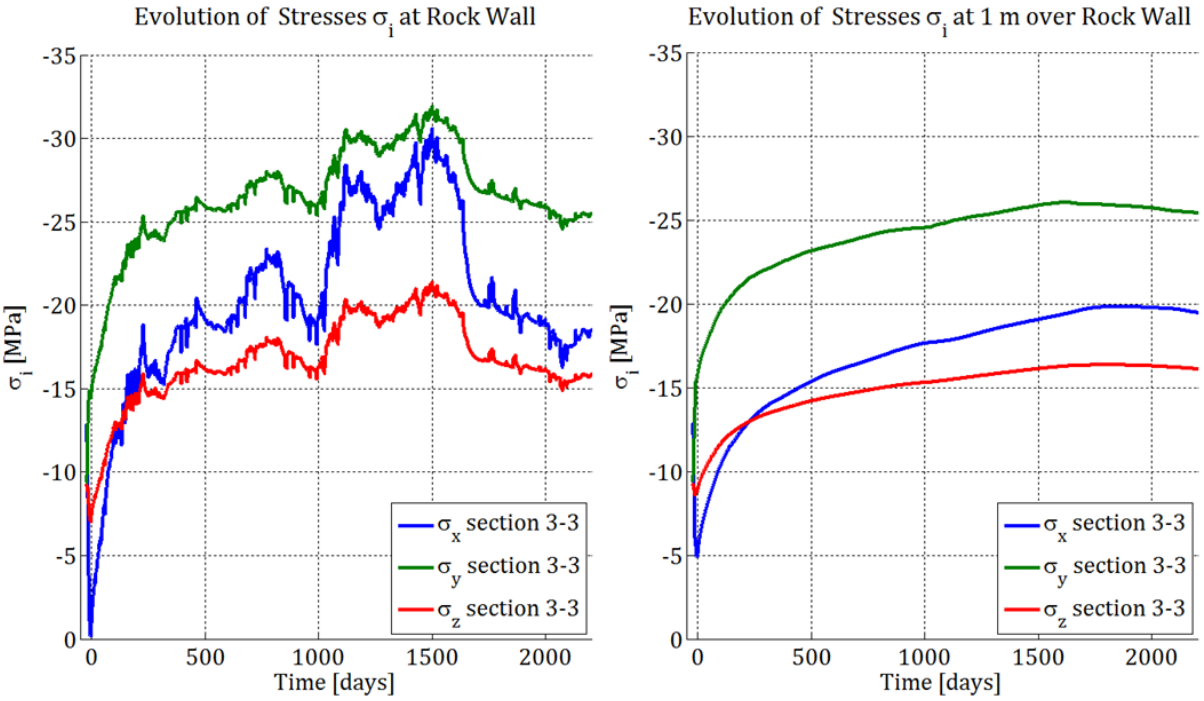

Figure 74: Modelling – Extent of the influence of the EDZ: Evolution of the stresses at the rock wall (left) and at 1 m over it (right). Set of parameters #4.00. Section 3-3- refers to the horizontal direction (cf. Figure 72, right).

As of why this phenomenon is noticeable vertically but not horizontally (Figure 70), let us briefly remind that Formulation 4 correlates the evolution of permeability with the ratio of plasticity. Also, the threshold value above which the permeability can vary is determined on the basis of Figure 66. Because the value chosen ($\Upsilon^{thr} = 0.6$, cf. set #4.00, Table 22) was slightly overestimated vertically[26], this allowed the fluctuations to affect the evolution of the EDZ in that direction. In other words, defining a higher threshold would avoid the further extension of the SDZ. Nevertheless, the water pressures would not correspond as well as in the original case.

[25] *They can be split into two categories: daily and seasonal fluctuations. Here we refer to the latter.*
[26] *But it was underestimated horizontally.*

Figure 74 shows that the stresses within the rock formation are indeed fluctuating and highlights that these variations become less important as we go further in the rock mass.

Referring to Figure 75, the horizontal convergence of the gallery is well represented on the long term, despite being a little overestimated on the short term. In contrast, the vertical convergence hardly corresponds to the experimental data's. The displacement of the gallery can be increased if the material enters in plasticity sooner. However, this method is not conceivable in this work for 2 reasons. Firstly, decreasing the parameters would be in contradiction with the parameters calibration (chapter 4); but most importantly, if the rock were to be weakened in the vertical directions, this would strongly affect the characteristics of the EDZ. As a matter of fact, this would stretch the zone vertically since the ratio of plasticity would be higher along this orientation.

This confrontation shows the limitations of the proposed law (Formulation 4). Indeed, as mentioned in section 2.5, fracturing networks were observed in the gallery, which are the reasons why the vertical convergence is so important although the horizontal initial stress is bigger than the vertical one. One possible way to tackle this problem is to enhance the mechanical model, such as representing the fractures by means of shear bands localisation [PARDOEN, et al., 2014].

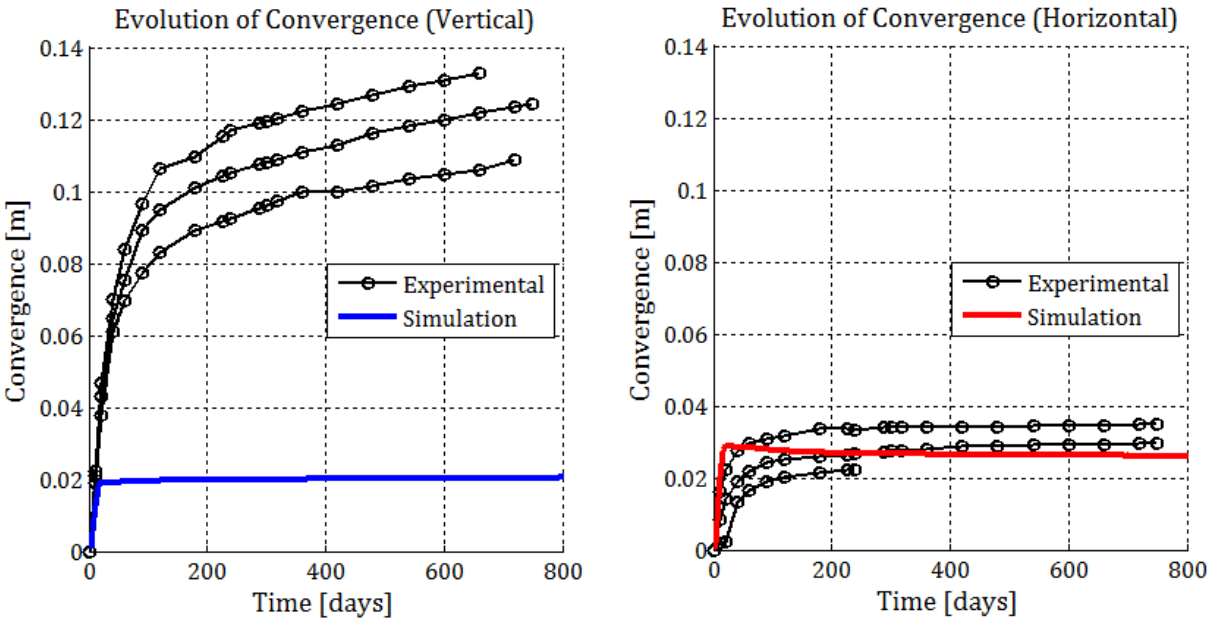

Figure 75: Modelling – Convergence: Evolution of the gallery convergence vertically (left) and horizontally (right). Set of parameters #4.00. Comparison with the experimental measurements.

C. Water and Vapour Exchanges at the Rock Wall

In this part, we analyse the aspects related to the water and vapour exchanges at the rock wall. As a reminder, a non-classical hydraulic boundary condition is used to model these flows, which has 2 components: the seepage flow S (which prevents unphysical water inflows) and the evaporation flow E (which allows a thermodynamical equilibrium between the air of the gallery and the rock formation).

As a result, during the excavation phase, water seepage flows are dominant and start when the water pressures are lowered due to the advancement of the excavation front. Once the ventilation test begins (day 0), the imposed water pressures are negative, such that the seepage stops (since they are lower than the atmospheric pressure). In parallel, this marks the beginning of the evaporation.

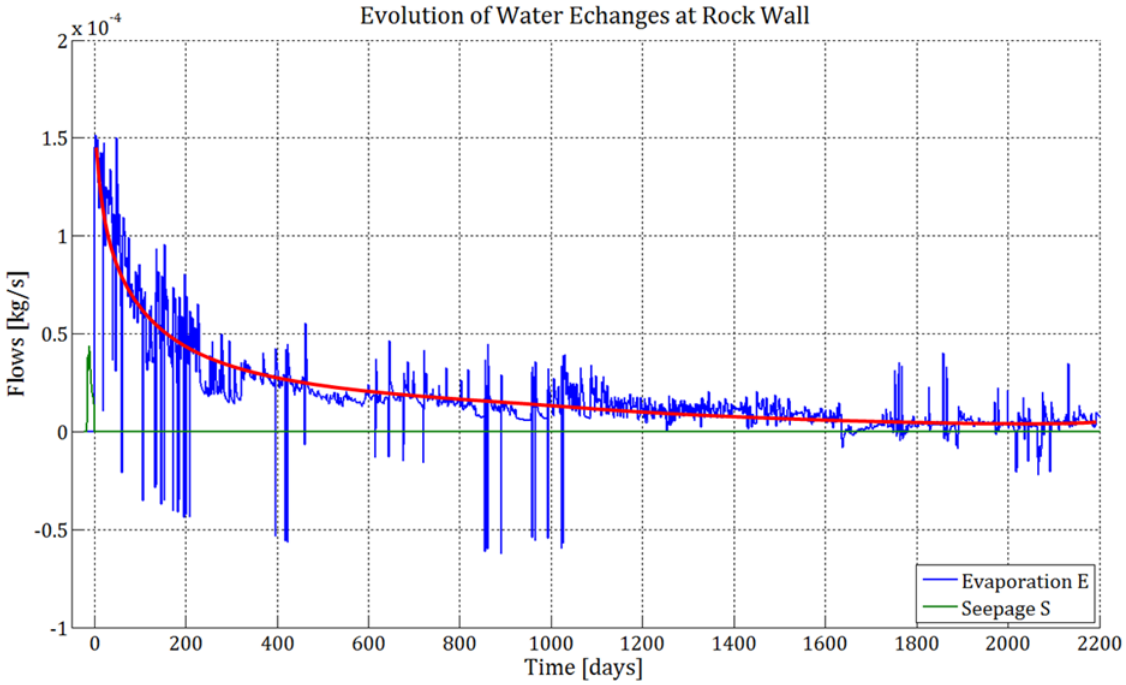

Figure 76: Modelling – Water Exchanges: Evolution of the evaporation and the seepage flows (daily values). Set of parameters #4.00 ($\alpha_0 = 10^{-3}$m/s). Red curve highlights the decreasing evaporation flow.

.

On Figure 76, the evolution of both phenomena is depicted in terms of daily flows. The red curve highlights the decreasing tendency of the evaporation, despite the presence of fluctuations. Thus, this suggests that there is time after which an equilibrium is reached, i.e. the contribution of water exchanges becomes negligible.

Consequently, when confronting water content results with the on-site measurements (Figure 77, right), we can see that the green curve (corresponding to the set#4.00, cf. Table 22) matches the data's on the short term, but gradually goes below. We could interpret this underestimation as choice of α_0 too high.

The default value adopted is $\alpha_0 = 10^{-3}\, m/s$ and is lower than those determined experimentally. Indeed, this coefficient is determined in practice through drying tests [LEONARD, et al., 2002]. In his PhD thesis, [GERARD, 2011] studied the behaviour of the Awans silt and the Boom clay (both from Belgium). The latter has similar properties to the Callovo-Oxfordian argillite. It has been concluded (among other things) that the mass transfer coefficient ranges from 2.10^{-2} to 5.10^{-2} $[m/s]$ for the Boom Clay.

The aim thus consists in trying to use a higher value of the coefficient and correspond correctly to the experimental measures at the same time. An alternative formulation proposed by [GERARD, et al., 2010], considers that the evaporation flow depends on the degree of saturation at the boundary limit: $E = f(\alpha_0, S_{rw}^f) = \alpha_0 . S_{rw}^f . (\rho_v^f - \rho_v^{cav})$.

The numerical result is presented in red on Figure 77 (right). This formulation shows that the evolution of the water content is higher than the first case. However, after 1000 days, this correspondence is deteriorated.

In fact, referring to Figure 77 (left), we can see that even for smaller values of the coefficient, there also comes a moment when the curves (blue or green) follow the tendency of the imposed values[27] (in red). The difference between the two parameters only resides in the speed at which this phenomenon takes place. Therefore, Figure 77 (left) proves that underestimating the water content on the long-term is inevitable (the measurements seem to have a horizontal asymptotic behaviour, while the numerical results continuously decrease).

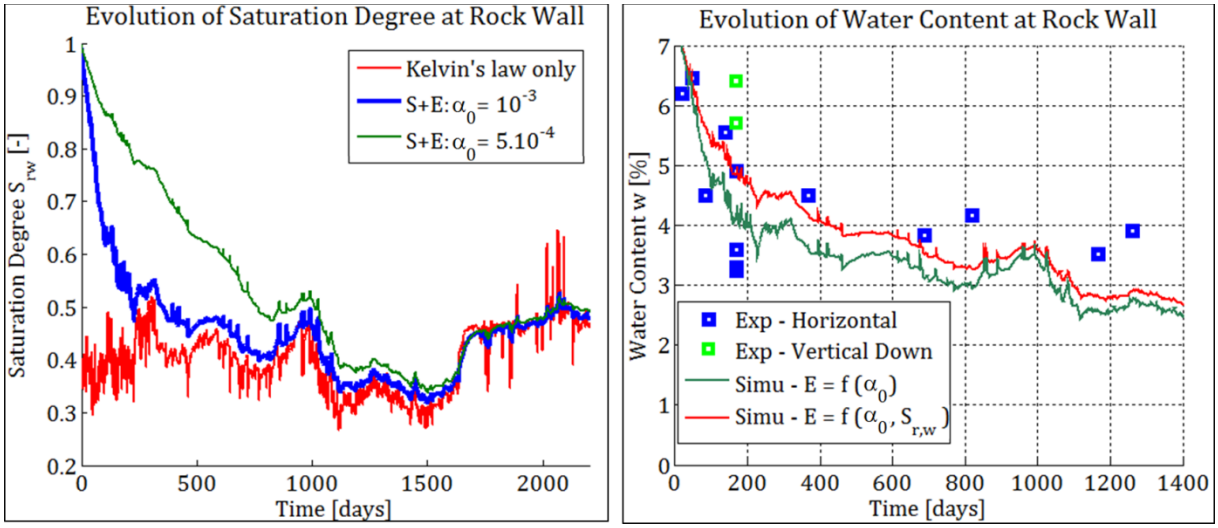

Figure 77: Modelling – Evaporation flow: Evolution of the saturation degree at the rock wall (left). Influence of α_0. Evolution of water content at the rock wall (right). Influence of the formulations and comparison with experimental measurements. Horizontal numerical results.

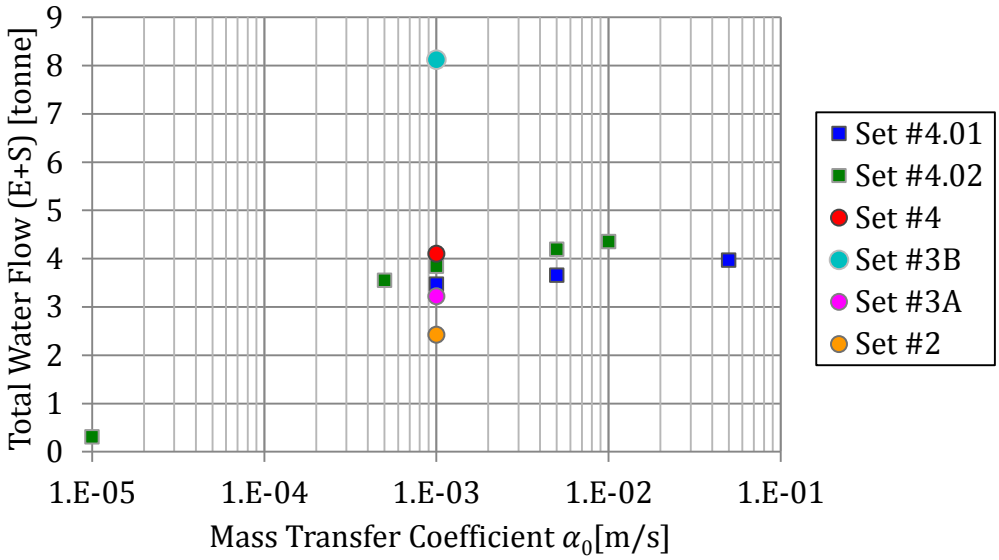

Figure 78: Modelling – Influence of the mass transfer coefficient on the water and vapour exchanges at the rock wall. The total water flow corresponds to the cumulative value taken at the end of the simulation. Circles refer to the single sets of parameters introduced in section 5.3.1, while squares are varying the coefficient α_0.

[27] *This curve is obtained by applying Kelvin's law to the imposed water pressures at the gallery.*

In fact, we want to demonstrate that as long as the EDZ is well defined, the value of the mass transfer coefficient is not as restraining as previously suggested. To support this idea, we integrate with respect to time the curve of total flow (i.e. the sum of the green and the blue curves of Figure 76). This gives us the cumulative water flow (in tonne). The final value of that variable represents the total amount of water that left the host formation (mainly by means of evaporation).

If we represent this calculated value as a function of the mass transfer coefficient, we obtain Figure 78 for different combinations of parameters. This method allows us to have a general idea of the hydraulic conditions within the rock formation. Indeed, a high water output would suggest a high desaturation, whereas a low value would imply the opposite.

The sets of parameters Set #2, Set #3A, Set #3B and Set #4 were determined in the previous section, and are respectively listed here below:

$\boldsymbol{\theta}$ [−]	$\boldsymbol{\beta}$ [−]	$\boldsymbol{\varepsilon_{eq}^{thr}}$ [−]	$\boldsymbol{\varepsilon_{eq}^{max}}$ [−]
2.10^{12}	3	$2.7.10^{-3}$	$3.5.10^{-3}$

Table 23: Numerical Results Analysis – Formulation 2: Set of main parameters #2.

	$\boldsymbol{\theta}$ [−]	$\boldsymbol{\beta}$ [−]	$\boldsymbol{\varepsilon_{eq}^{thr}}$ [−]	$\boldsymbol{\varepsilon_{eq}^{max}}$ [−]
$\boxed{A}$	2.10^{12}	3	$2.7.10^{-3}$	$4.5.10^{-3}$
$\boxed{B}$	2.10^{12}	3	$1.64.10^{-3}$	$3.5.10^{-3}$

Table 24: Numerical Results Analysis – Formulation 3: Sets of main parameters #3A and #3B.

$\boldsymbol{\theta}$ [−]	$\boldsymbol{\beta}$ [−]	$\boldsymbol{\Upsilon^{thr}}$ [−]	$\boldsymbol{\varepsilon_{eq}^{max}}$ [−]
2.10^{10}	3	0.6	$3.5.10^{-3}$

Table 25: Evolution of permeability – Formulation 4: Set of main parameters #4.

Set #4.01 is the same as set #4.00, but uses several values of α_0:

Formulation	$\boldsymbol{\theta}$ [−]	$\boldsymbol{\beta}$ [−]	$\boldsymbol{\Upsilon^{thr}}$ [−]	$\boldsymbol{\varepsilon_{eq}^{max}}$ [−]	$\mathbf{k_{hor}}$ $[\mathbf{m^2}]$	$\mathbf{k_{ver}}$ $[\mathbf{m^2}]$
4	2.10^{10}	3	0.6	$3.5.10^{-3}$	$4*10^{-20}$	$1.33*10^{-22}$

Table 26: Evolution of permeability – FINAL set #4.01:
Formulation 4 with anisotropy of the intrinsic permeability.

Regarding #4.02, the set is similar to #4.01, but now without any upper limit value:

Formulation	$\boldsymbol{\theta}$ [−]	$\boldsymbol{\beta}$ [−]	$\boldsymbol{\Upsilon^{thr}}$ [−]	$\boldsymbol{\varepsilon_{eq}^{max}}$ [−]	$\mathbf{k_{hor}}$ $[\mathbf{m^2}]$	$\mathbf{k_{ver}}$ $[\mathbf{m^2}]$
4	2.10^{10}	3	0.6	/	$4 * 10^{-20}$	$1.33 * 10^{-22}$

Table 27: Evolution of permeability – FINAL set #4.02: Formulation 4 with anisotropy of the intrinsic permeability.

From Figure 78, we see that varying the mass transfer coefficient in a range of $3.5\ 10^{-3}$ to $5\ 10^{-2}\ m/s$ does not have an impact on the total water flows as significant as modifying the dimensions of the EDZ. Indeed, referring to Figure 61, the dimensions of the EDZ using Set #3B are around 5 meters in all directions (in contrast to the zone of 3.1m X 1.1 m). If we compare that value to the final set of parameters used #4.00 (with or without considering the anisotropy of the hydraulic parameters), we have at least doubled the quantity of water outflow.

Furthermore, putting aside this extreme scenario, as the mass transfer coefficient is acting at the rock wall of the gallery only (through the term of evaporation flow E), and since the evaporation effect is decreasing with time for any 'reasonable' values of α_0 (interval mentioned here above), varying it does not have a significant impact either on the water pressures in the far locations of the SDZ drills.

These observations are supported by what has been observed in [CHARLIER, et al., 2013b]. Indeed, the report explained that for values of mass transfer coefficient higher than$10^{-5}\ m/s$, the water pressures were not correctly represented. As a matter of fact, the EDZ simulated in that first part did not correspond to the experimental measurements of permeability realised by [CRUCHAUDET, et al., 2010a]. However the second part of the work shows that if the EDZ is defined correctly (i.e. 3.1 m vertically and 1.1 m horizontally), considering $\alpha_0 = 10^{-3} m/s$ would give good results. Our conclusion goes further than that: *if the EDZ is correctly represented, even the experimental values can be used.*

These observations end the second part of the simulations. The last one explores the concept of the anisotropy of mechanical parameters. To remain consistent with the previous parts, we decide to keep the default value of the mass transfer coefficient, but keeping in mind that its influence is quite limited for our case.

5.3.3 Anisotropy of the Mechanical Parameters

As of now, the material considered had isotropic mechanical parameters in both elasticity and plasticity. This part explores the concept of anisotropy and studies its influence on the simulations. Indeed, it was pointed out in the previous sections, notably the parameters calibration (chapter 4) and the description of the evolution of the permeability (section 5.3.1), that the behaviour of the rock was not the same in all the directions.

In particular, regarding the confrontation with the water pressures (final results on Figure 69, section 5.3.1), we observed that the simulated water pressures at 45° (SDZ1241) were slightly higher than the experimental measurements. Despite the fact that the correspondence is still good, there is a will to improve the numerical representation.

As the hydraulic anisotropy has previously been introduced (by considering 2 different values of intrinsic permeability), this last part focuses on the mechanical aspect. It first explains the main theoretical concepts, describes the parameters used and proceeds to the simulation results.

A. Theoretical Concepts

ELASTICITY

From Figure 16 (p.14), the rock formation can be seen as isotropic along the horizontal bedding planes (sedimentary materials). This leads to the notion of orthotropy and cross-anisotropy (also called transversal isotropy). The former means that the properties of the rock are symmetric with respect to three orthogonal planes, whereas the latter refers to parallel isotropic planes [LEKHNITSKII, 1963].

In the further statements, the following reference frame is considered (Figure 46): $(\hat{x}, \hat{z})$ is the isotropic planes orientation, and $\hat{y}$ is the normal to these planes (Figure 45).

While the elastic behaviour of an isotropic material is defined by two parameters (E and ν), anisotropy is characterised by 21 parameters. In the case of orthotropy, the symmetry reduces their number to 9. Defining Coulomb's modulus G,

$$G = \frac{E}{2(1+\nu)} \tag{61}$$

the compliance tensor D_{ijkl} from Equation 32 can be rewritten:

$$D_{ijkl} = \begin{bmatrix} \frac{1}{E_x} & -\frac{\nu_{yx}}{E_y} & -\frac{\nu_{zx}}{E_z} & 0 & 0 & 0 \\ -\frac{\nu_{xy}}{E_x} & \frac{1}{E_y} & -\frac{\nu_{zy}}{E_z} & 0 & 0 & 0 \\ -\frac{\nu_{xz}}{E_x} & -\frac{\nu_{yz}}{E_y} & \frac{1}{E_z} & 0 & 0 & 0 \\ 0 & 0 & 0 & \frac{1}{2G_{xy}} & 0 & 0 \\ 0 & 0 & 0 & 0 & \frac{1}{2G_{xz}} & 0 \\ 0 & 0 & 0 & 0 & 0 & \frac{1}{2G_{yz}} \end{bmatrix} \tag{62}$$

We obtain the expression of the stiffness tensor C_{ijkl} by inversing D_{ijkl}. To describe the elasticity of a material characterised by cross-anisotropy, 5 independent parameters are needed: $E_{\parallel}$, $E_{\perp}$, $\nu_{\parallel\parallel}$, $\nu_{\parallel\perp}$, $G_{\parallel\perp}$, where ∥ and ⊥ stand for the directions parallel and perpendicular to the bedding (respectively). Indeed, following this formalism, the parameters become:

$$\begin{cases} E_x = E_z & = E_{\parallel} \\ E_y & = E_{\perp} \\ \nu_{xz} = \nu_{zx} & = \nu_{\parallel\parallel} \\ \nu_{yz} = \nu_{yx} & = \nu_{\perp\parallel} \\ \nu_{zy} = \nu_{xy} & = \nu_{\parallel\perp} \\ G_{xz} & = G_{\parallel\parallel} \\ G_{xy} & = G_{\parallel\perp} \\ G_{yz} & = G_{\perp\parallel} \end{cases} \quad \textbf{(63)}$$

The symmetry of the compliance tensor D_{ijkl} implies that

$$\frac{\nu_{\parallel\perp}}{E_{\parallel}} = \frac{\nu_{\perp\parallel}}{E_{\perp}} \quad \textbf{(64)}$$

Similarly, the symmetry of the stress and strain tensors leads to the following equality:

$$G_{\parallel\perp} = G_{\perp\parallel} \quad \textbf{(65)}$$

Lastly, the shear modulus in the isotropic planes $G_{\parallel\parallel}$ is derived from Equation 61.

$$G_{\parallel\parallel} = \frac{E_{\parallel}}{2(1+\nu_{\parallel\parallel})} \quad \textbf{(66)}$$

As a result of these three equations, five independent equations remain from Equation 63. Let us remark that a change of reference system can be realised if the reference frame in which is defined the anisotropy is not the same as the one used to describe the stress state. In that case, the change is computed by means of a rotation matrix [CHARLIER, 2000], [CESCOTTO, 2011], [PARDOEN, et al., 2015].

In addition to the Young modulus and Poisson's coefficient, anisotropic elasticity also affects the compressibility of the solid grains skeletons. Biot's tensor b_{ij} used in Equation 24 is symmetric and defined as followed [CHENG, 1997]:

$$b_{ij} = \delta_{ij} - \frac{C_{ijkk}}{3\,K_s} \quad \textbf{(67)}$$

Where C_{ijkl} is the stiffness tensor in anisotropic elasticity, and K_s the bulk modulus of the solid phase. For orthotropic materials, the tensor is reduced to a diagonal matric. Furthermore, regarding cross-anisotropy, Biot's tensor is written:

$$b_{ij} = \begin{bmatrix} b_{\parallel} & 0 & 0 \\ 0 & b_{\perp} & 0 \\ 0 & 0 & b_{\parallel} \end{bmatrix} \quad with \quad \begin{cases} b_{\parallel} = 1 - \dfrac{1+\nu_{\parallel\parallel}+\nu_{\parallel\parallel}\nu_{\perp\parallel}+\nu_{\perp\parallel}}{E_{\parallel}E_{\perp}.\eta\ 3\mathrm{K_s}} \\ b_{\perp} = 1 - \dfrac{1-\nu_{\parallel\parallel}^2+2\nu_{\parallel\perp}+2\nu_{\parallel\perp}\nu_{\parallel\parallel}}{E_{\parallel}E_{\parallel}.\eta\ 3\mathrm{K_s}} \\ \eta = \dfrac{1-\nu_{\parallel\parallel}^2-2\nu_{\perp\parallel}\nu_{\parallel\perp}.(1+\nu_{\parallel\parallel})}{E_{\parallel}E_{\parallel}E_{\perp}} \end{cases} \quad \textbf{(68)}$$

PLASTICITY

The anisotropy of a material can be taken into account towards its plastic behaviour, notably through the cohesion c. The material cohesion anisotropy can be defined by means of the microstructure fabric tensor a_{ij}, which is a measure of the material fabric. The principal material axes $(\hat{x}, \hat{y}, \hat{z})$ (cf. Figure 46) are related to the eigenvectors of this tensor. In addition to that, let us define a generalised loading vector $\underline{l}$ (Equation 69), on which the projection of a_{ij} corresponds to the cohesion. In that sense, the cohesion characterises the loading direction relative to the material axes (Equation 70).

$$l_i = \sqrt{\frac{\sigma_{i1}^2 + \sigma_{i2}^2 + \sigma_{i3}^2}{\sigma_{ij}\sigma_{ij}}} \quad \textbf{(69)}$$

$$c = a_{ij} l_i l_j \quad \textbf{(70)}$$

Where σ_{ij} is expressed in reference to the material axes. The cohesion can be expressed as:

$$c = c_0.\left(1 + A_{ij} l_i l_j\right) \quad \textbf{(71)}$$

With $c_0 = a_{ii}/3$ a microstructure parameter and $A_{ij} = a_{ij}/c_0 - \delta_{ij}$ a traceless symmetric tensor $(A_{ii} = 0)$. The above expression can be generalised by considering higher order tensors. Considering a second-order polynomial, Equation 71 becomes:

$$c = c_0.\left(1 + A_{ij} l_i l_j + b_1\left(A_{ij} l_i l_j\right)^2\right) \quad \textbf{(72)}$$

Where b_1 is a constant. In the case of cross-anisotropy, the non-diagonal terms of A_{ij} are equal to zero and $A_{22} = -2A_{11}$ (where A_{11} is the component in the isotropic plane). As a result,

$$A_{ij} l_i l_j = A_{11}.[1 - 3.(l_2)^2] \quad \textbf{(73)}$$

Injecting Equation 73 into Equation 72, the final expression of the transversal isotropic cohesion is obtained:

$$c = c_0.(\ 1\ +\ A_{11}.[1 - 3.(l_2)^2]\ +\ b_1.(A_{11})^2.[1 - 3.(l_2)^2]^2\ ) \quad \textbf{(74)}$$

For uniaxial compression, $l_2 = \cos\alpha$ with α being the angle between the compression direction and the normal to the bedding plane (to differentiate from α_0). In other words, $\alpha = 0°$ if the loading is perpendicular to the bedding plane, and $\alpha = 90°$ if parallel [AMADEI, 1983].

The next section describes the several parameters used for the simulation and explains how their values were chosen.

B. Parameters Used

In the following simulations, the evolution of the intrinsic permeability is characterised by set #4.00 (obtained in section 5.3.1, cf. Table 22). The other hydraulic parameters are still the ones listed in section 5.2. Regarding the mechanical parameters, let us first define the set of parameters 'SET 0' when referring to the isotropic case, which is also presented in section 5.2 and reminded in Table 7. Among the values, let us remind the values subjected to modification:

- Elastic parameters: $E = 4\,000\ [MPa]$ and $\nu = 0.30\ [-]$
- Plastic parameter: $c = 4.50\ [MPa]$

The work of [PARDOEN, et al., 2015] proposes a set of parameters (determined on the basis of experimental campaigns) that can describe the evolution of the cohesion of the COX. Referring to Equation 74, the values of this set (noted SET1 in this work) are:

$$c = f(c_0, A_{11}, b_1, l_2) \quad with \quad \begin{cases} c_0 = 4.10\ [MPa] \\ A_{11} = 0.1171\ [-] \\ b_1 = 14.236\ [-] \end{cases}$$

From there, we decide to develop two sets of parameters (SET2 and SET3) used in the simulations and displayed at Table 28. Indeed, SET1 needs to be adapted to our case.

The values showed here above suggest that the initial cohesion for isotropic loading is at $4.10\ MPa$. To remain consistent with both [PARDOEN, et al., 2015] and our work (chapter 4), we modify 'SET1'; on one hand because the initial loading is actually not isotropic, on the other hand so that the value of the initial cohesion corresponds to the one calibrated (i.e. $c = 4.50\ MPa$). However, we have to keep in mind that the tendency of the curve has to remain the same. Consequently, the evolution curve is simply shifted upwards.

The initial cohesion corresponds to the initial stress state of the rock formation. Thus, considering the initial stresses ($\sigma_{11} = \sigma_{33} = 12MPa$ and $\sigma_{22} = 15.6\ MPa$), the initial value of l_2 is $l_{2;0} = 0.52$. The resulting shifted curve (solid line) is displayed along with the original one (dashed line) on Figure 79. Further explanations and details of calculation are given at Appendix 8.7.

In parallel, we propose another set (SET3) which is based on the curve corresponding to the parameters of SET2, but with the difference that the extreme values (i.e. for $l_2 = 0$ and $l_2 = 1$) are the same. In other words, there is a certain degree of symmetry with respect to the starting point (represented by a cross on Figure 80). For clarity reasons, this choice is justified in the part devoted to the simulations.

Lastly, we also consider anisotropic elastic parameters [PARDOEN, et al., 2015] and [CRUCHAUDET, et al., 2010b] taken from SET1 and used in for SET2 and SET3.

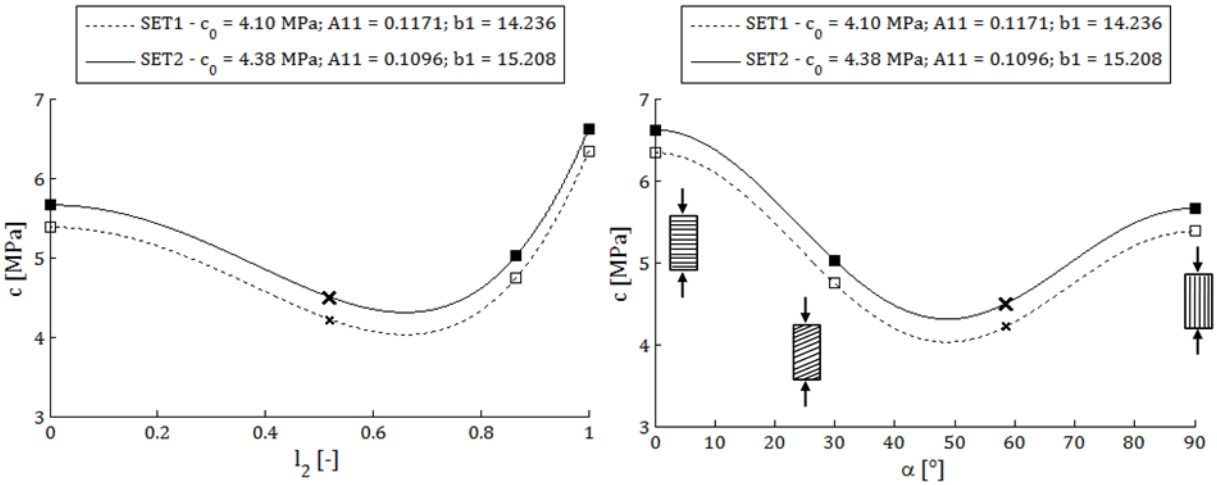

Figure 79: Evolution of the cohesion with respect to the loading vector (left) and with respect to the angle between the normal to bedding planes and the direction of loading (right). The empty squares represent the data's of simple compression tests carried out on samples with different orientations (0°, 30° and 90°) [PARDOEN, et al., 2015]. The filled squares correspond to the results shifted. The crosses refer to the initial stress tensor ($\sigma_{11} = \sigma_{33} = 12$MPa and $\sigma_{22} = 15.6$ MPa).

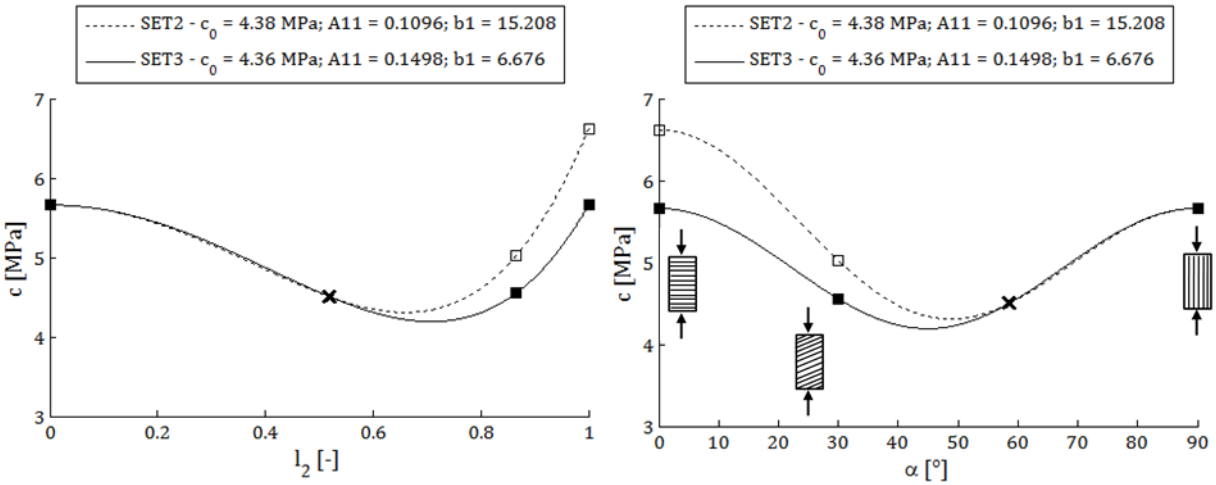

Figure 80: Evolution of the cohesion with respect to the loading vector (left) and with respect to the angle between the normal to bedding planes and the direction of loading (right). SET 2 and SET3 are respectively represented in dash and solid lines.

Table 28 regroups the several values from SET0 to SET3. Let us remind that to describe the elasticity of a material characterised by cross-anisotropy, only 5 independent parameters are needed: $E_{\parallel}$, $E_{\perp}$, $\nu_{\parallel\parallel}$, $\nu_{\parallel\perp}$, $G_{\parallel\perp}$ (or in the current notations: E_1, E_2, ν_{13}, $\nu_{12}$and G_{12}).

Symbol	Name	Unit	Component	SET0	SET1	SET2	SET3
$\boldsymbol{E}$	Young Modulus	MPa	E_1	4 000	5 000	5 000	5 000
			E_2	4 000	4 000	4 000	4 000
			E_3	4 000	5 000	5 000	5 000
$\boldsymbol{\nu}$	Poisson Coefficient	–	ν_{12}	0.3	0.325	0.325	0.325
			ν_{13}	0.3	0.24	0.24	0.24
			ν_{23}	0.3	0.26	0.26	0.26
$\boldsymbol{G}$	Coulomb Modulus	MPa	G_{12}	1 538	1 630	1 630	1 630
			G_{13}	1 538	2 016	2 016	2 016
			G_{23}	1 538	1 630	1 630	1 630
$\boldsymbol{c_0}$	Cohesion in isotropic loading	MPa	/	4.50	4.10	4.38	4.36
$\boldsymbol{A_{11}}$	Cohesion Parameter	–	/	0	0.12	0.11	0.15
$\boldsymbol{b_1}$	Cohesion Parameter	–	/	0	14.24	15.21	6.68

Table 28: Anisotropy of the mechanical parameters – parameters of the several sets used. Subscripts '-1' and '-3'refer to the component in the isotropic plane (bedding).

C. *Numerical Results*

The aim of such model enhancement is to improve the correspondence between the numerical and experimental water pressures located in the SDZ1241 drill (45° upwards). As a matter of fact, Figure 81 shows that thanks to SET2, the previously overestimated water pressures (left) are now (right) closer to the experimental measurements.

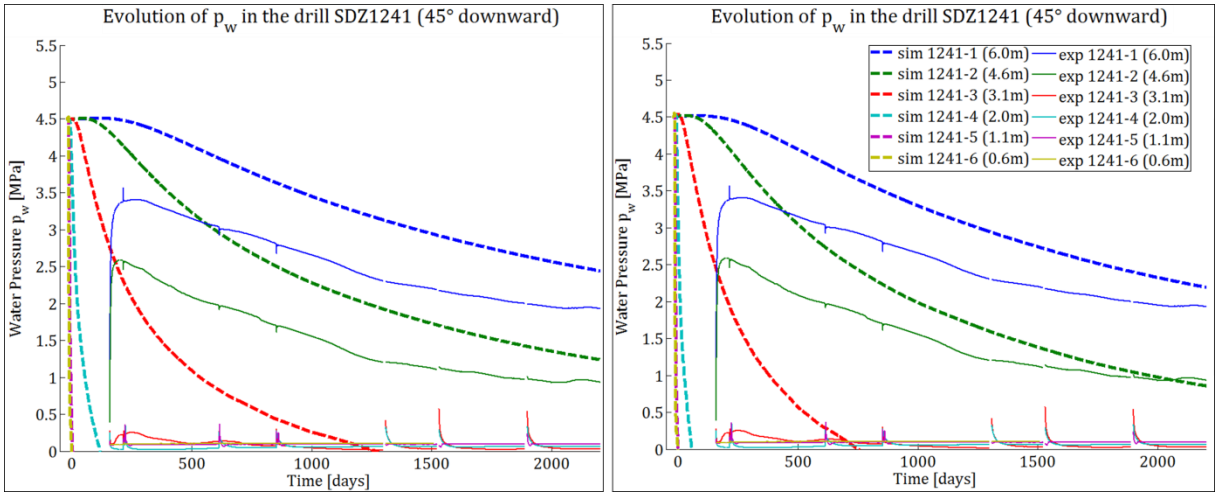

Figure 81 Modelling –Contribution of the anisotropy of mechanical parameters: Evolution of the water pressures in the SDZ1241 drill (45° downwards) using SET0 (left) and SET2 (right). Numerical results are represented in dashed lines and the experimental measures in solid lines.

Such modification on the behaviour of the argillite also implies that the plastic zone develops differently. Indeed, referring to Figure 79, the curve suggests that while the cohesion has been deteriorated for $\alpha = 45°$, it also became higher in the other directions, compared to the isotropic case (SET0). Consequently, the plastic zone stretches 'diagonally' but is shortened elsewhere (Figure 82). This shrinkage is strongly felt horizontally: the rock does not even yield.

The major inconveniency of SET2 resides therefore in the misrepresentation of the EDZ. Indeed, Formulation 4 correlates the evolution of the intrinsic permeability with the ratio of plasticity. Thus, even if the threshold value Υ^{thr} were to be lowered (cf. Equation 58), the zone in which the permeability evolves might get wider, but the shape would still be in conflict with the experimental measurements.

To tackle this problem, the value of the cohesion needs to be decreased at these orientations (or at least, horizontally). On Figure 79 (left), c is higher for $\alpha = 0°$than for $\alpha = 90°$. A quite intuitive solution consists therefore in lowering the evolution curve such that the cohesion is the same at both extremities. The parameters found give us SET3.

The evolution curves of SET2 and SET3 are shown on Figure 80. Referring to the left graph, let us note that after the excavation, l_2 becomes approximately equal to 0 vertically, and to 0.74 horizontally[28]. As result, starting from $l_{2;0}$ (cross marker), we go all the way to the left when looking at the rock in the vertical sections. In contrast, regarding the horizontal section, we go towards the right extremity, but stop much sooner. This phenomenon limits the effects caused by modifying the curve: the decrease of the cohesion horizontally is not as strong as expected since we are not at the extremity of the curve.

[28] *This was calculated analytically, considering that the radial stress goes down to 0 and neglecting the non-diagonal terms of* σ_{ij}.

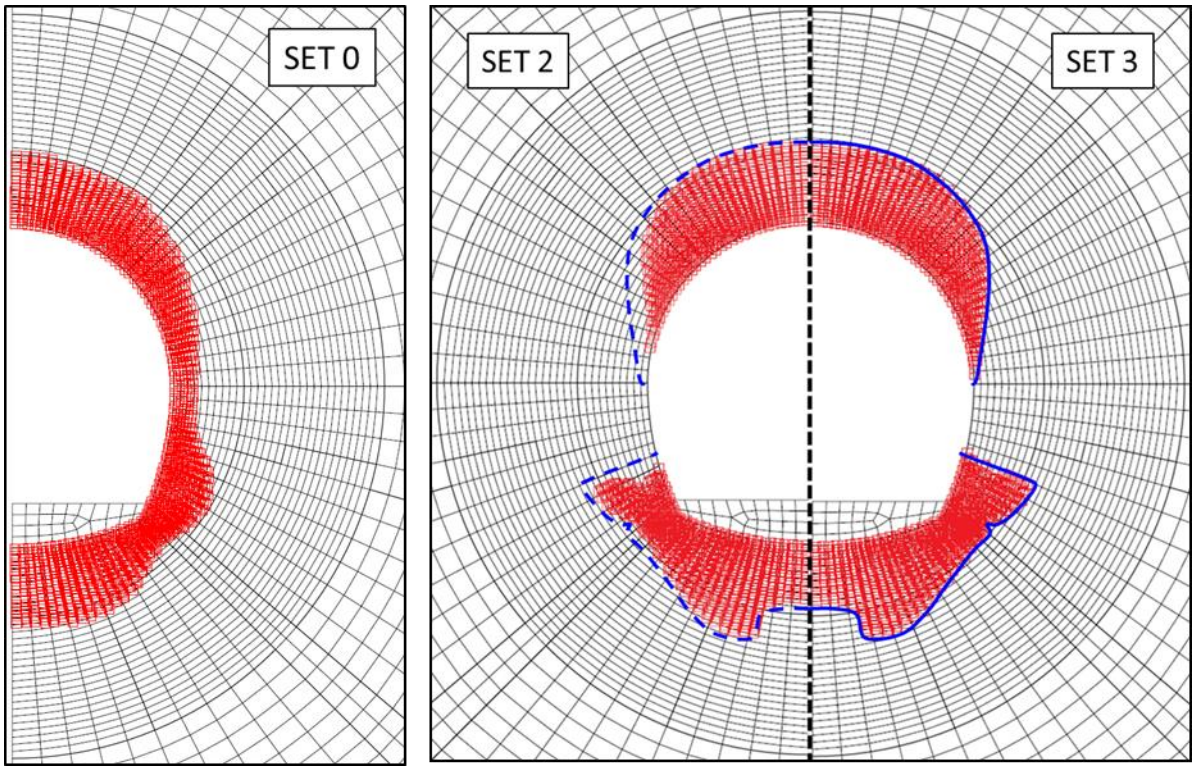

Figure 82: Modelling – Anisotropy of mechanical parameters: Extent of the plastic zone at the end of the excavation. Comparison between the isotropic case (SET0, left) and the enhanced models (SET2 and SET3). Blue lines highlight the difference between SET2 (middle) and SET3 (right).

Still, the blue lines on Figure 80 highlight an extension of the plastic zone (from SET2 to SET3) in the desired direction. This shows that the EDZ could theoretically be modified at will, and thus be correctly reproduced (in cross-anisotropy) if we further modify the evolution curve (Figure 78 and Figure 79). However, because the modified curves are not supported by any experimental data's, continuing in that direction would be inappropriate (and would also contradict previous works).

5.4 Conclusion

This chapter is focused on the modelling of the ventilation test in the GED gallery. The simulations are carried out in 2D plane strain with hydromechanical couplings, in isotherm conditions and with a constant gas pressure. The starting configuration considers an isotropic material governed by the mechanical and hydraulic models described in chapter 3.

Before entering into the main subject, this chapter first presents the conditions in which the simulations are realised: the geometry of the meshing, the initial and the boundary conditions. The values of the several parameters used in the modelling are also specified.

The modelling itself can be divided into 3 parts. The first one explains the main steps leading to a law of behaviour that modifies the hydraulic parameters on the basis of the mechanical variables. In particular, we develop a formulation able to describe correctly the EDZ by correlating the intrinsic permeability of the medium with the ratio of plasticity. To validate the results, the water pressures are confronted with the experimental measurements.

As the rock damage largely takes place during the excavation, the first part mainly focuses on that period. The second part analyses the several impacts of the ventilation test itself, and confronts the numerical results with other available experimental measurements. The aspects discussed can be split into 3 categories following their nature (hydraulic, mechanical and water-vapour exchanges at the rock wall). In particular, the comparisons with the experimental measurements showed good results concerning the hydraulic aspect. In contrast, due to the presence of fracturing, which is not taken into account by the presented model (homogenous medium), the convergence are underestimated vertically, although they quite match the data's horizontally. Lastly, the analysis of the influence of water and vapour exchanges at the rock wall (notably by means of the mass transfer coefficient) shows that using different values of the coefficient has an impact which is not as significant as describing correctly the EDZ.

The third part introduces the concept of anisotropy of the mechanical parameters (elastic and plastic). Two sets of parameters, inspired from previous works, are used for the simulations. We observe that the shape of the EDZ is modified and stretched differently, due to the development of the plastic zone. As a result, exploring this concept allows us to discover the limitations of the formulation proposed at the end of the first part. By using the ratio of plasticity to make the permeability vary, it is concluded that the zone can theoretically be modified at will, for instance by changing the evolution of the cohesion with respect to the loading orientation. However, no further attempts were made because of the lack of available experimental data's to support any further developments. Despite all that, considering anisotropic mechanical parameters has improved the correspondence of the water pressures with the experimental data's,

6 Conclusion

When producing electricity, nuclear energy plays an important role in our modern societies: more than 13 % of the world electricity production comes from nuclear sources. This share rises up to 75 % in France. With its 58 nuclear reactors among the 439 operational around the world, it is the country the most dependent on nuclear electricity. However, these nuclear wastes can be extremely harmful to man and nature, in such a way that it is crucial to isolate them. Deep geological storage was thus selected as a potential solution for the most critical wastes. Yet, the feasibility of such task is still under study. In France, ANDRA runs scientific research programs that investigate the storage possibilities in the Callovo-Oxfordian argillite, located at a depth between 400 and 600 m in the Meuse/Haute-Marne region.

An underground research laboratory (URL) was installed in the rock formation. It carries out series of experiments to study the thermal, hydraulic and mechanical behaviours of the rock formation following the disposal phase (excavation, wastes storage and sealing). Among these, the Saturation Damaged Zone (SDZ) experiment investigates the impact of the exploitation phase in the argillite through saturation/desaturation cycles (i.e. ventilation test). In particular, the excavation damaged zone (EDZ) and its evolution has to be characterised.

In this context, one of the main contributions of this work is to propose laws of behaviour that modify the hydraulic parameters on the basis of the mechanical variables, such that the hydraulic behaviour of the medium evolves in the same way regardless of the orientation. In particular, we developed a formulation able to describe correctly the EDZ by correlating the intrinsic permeability of the medium with the ratio of plasticity. Then, the influence of the ventilation test itself was examined in further details. Among the aspects discussed, the analysis of the influence of the mass transfer coefficient suggested that using values determined through drying tests was possible. In addition to that, the work also introduced the concept of anisotropy of the mechanical parameters. As a result, exploring this concept allowed us to discover the limitations of the newly proposed formulation. Moreover, considering anisotropic mechanical parameters has improved the correspondence of the water pressures with the experimental data's,

In addition to what has been achieved in this work, some leads requiring further investigations can be proposed. For instance, modelling the problem in 2D axisymetrical or in 3D could improve the correspondence with the experimental results, as these modelling would reproduce the axial flows. These flows might greatly influence the simulations when the airlock is closed. Another solution would be to consider enhanced models. Indeed, this work mentioned the concepts of self-sealing and self-healing [BERNIER, et al., 2004] [BASTIAENS, et al., 2007] which could explain the asymptotic behaviour of the measurements of water pressure. Lastly, the formulation proposed in this work could be enriched considering the orientations in which the solicitation occurs.

7 Bibliography

AMADEI, B. (1983). *Rock anisotropy and the theory of stress measurements* (Vol. 2). New York: Springer-Verlag. Lecture Notes in Engineering Series.

ANDRA. (2005). *Dossier 2005 Argile - Synthesis: Evaluation of the feasibility of a geological repository in an argillaceous formation, Meuse/Haute-Marne site.* ANDRA Report.

ANDRA. (2009a). *La radioactivité*. Retrieved from Agence Nationale pour la gestion des Déchets Radioactifs: http://www.andra.fr/pages/fr/menu1/les-dechets-radioactifs/la-radioactivite-7.html

ANDRA. (2009b). *Intermediate-level long-lived waste*. Retrieved from French National Radioactive Waste Management Agency: http://www.andra.fr/international/pages/en/menu21/waste-management/waste-classification/intermediate-level-long-lived-waste-1641.html

ANDRA. (2009c). *High-level waste*. Retrieved from French National Radioactive Waste Management Agency: http://www.andra.fr/international/pages/en/menu21/waste-management/waste-classification/high-level-waste-and-long-lived-intermediate-level-1610.html

ANDRA. (2012a). *Qu'est-ce qu'un déchet radioactif ?* Retrieved from Agence Nationale pour la gestion des Déchets Radioactifs: http://www.andra.fr/pages/fr/menu1/les-dechets-radioactifs/qu-est-ce-qu-un-dechet-radioactif-r-8.html

ANDRA. (2012b). *Rapport de synthèse: Inventaire national des matières et déchets radioactifs.* Retrieved from ANDRA: Les volumes de déchets radioactifs: http://www.andra.fr/download/site-principal/document/editions/467.pdf

ANDRA. (2012c). *En résumé: Inventaire national des matières et déchets radioactifs.* Retrieved from ANDRA: Les volumes de déchets radioactifs: http://www.andra.fr/download/site-principal/document/editions/466.pdf

ANDRA. (2012d). *Les étapes clés du Centre de Meuse/Haute-Marne*. Retrieved from ANDRA: https://www.andra.fr/andra-meusehautemarne/pages/fr/menu18/l-andra-en-meuse-et-haute-marne/les-etapes-cles-du-centre-de-meuse-haute-marne-6871.html

ANDRA. (2014a). *Waste Classification*. Retrieved from French National Radioactive Waste Management Agency: http://www.andra.fr/international/pages/en/menu21/waste-management/waste-classification-1605.html

ANDRA. (2014b). *Les expérimentations souterraines*. Retrieved from ANDRA: http://www.andra.fr/andra-meusehautemarne/pages/fr/menu18/le-laboratoire-souterrain/les-experimentations-1514.html

Areva. (2015a). *Réacteur EPR - Comment ça marche*. Retrieved from Areva.

Areva. (2015b). *Réacteur EPR - Réacteur durable*. Retrieved from Areva: http://www.areva.com/FR/activites-1705/racteur-epr-et-dveloppement-durable-rduction-des-dchets-radioactifs.html

Areva. (2015c). *Réacteur EPR - Un réacteur économiquement compétitf*. Retrieved from Areva: http://www.areva.com/FR/activites-1707/racteur-epr-conomique-et-comptitif.html

ARMAND, G., LEVEAU, F., NUSSBAUM, C., de La VAISSIERE, R., NOIRET, A., JAEGGI, D., LANDREIN, P., & RIGHINI, C. (2014). Geometry and properties of the excavation-induced fractures at the Meuse/Haute-Marne URL drifts. *Rock Mechanics and rock engineering*, pp. 21-41.

BARNICHON, J. D. (1998). *Finite Element Modelling in Structural and Petroleum Geology*. Faculté des Sciences Appliquées, Université de Liège.

BASTIAENS, W., BERNIER, F., & LI, X. (2007). SELFRAC: Experiments and conclusions on fracturing, self-healing and self-sealing processes in clays. *Physics and Chemistry on Earth, 32*, pp. 600-615.

BERNIER, F., & BASTIAENS, W. (2004). *Fracturation and Self-Healing Processes in Clays, The SELFRAC Project*. Community Research and Development Information Service (CORDIS).

BOSSART, P., MEIER, P., MOERI, A., TRICK, T., & MAYOR, J. (2002). Geological and hydraulic characterisation of the excavation disturbed zone in the Opalinus Clay of the Mont Terri Rock Laboratory. *Engineering Geology, 66 (1-2)*, pp. 19-38.

BOURDEAU, C., DEDECKER, F., & BILLAUX, D. (2007). Discrete modelling of drift behaviour in the meuse/haute-marne url (France). *Clays in natural and engineered barriers for radioactive waste confinement, International Meeting.* Lille, France.

BP. (2012). *BP Statistical Review of World Energy*. British Petroleum.

BP. (2013). *BP Statistical Review of World Energy*. British Petroleum.

BP. (2014). *BP Statistical Review of World Energy*. British Petrolium.

Britannica. (2013). *Nuclear Power - Pressurized-water reactor*. Retrieved from Encyclopædia Britannica: http://www.britannica.com/EBchecked/topic/421749/nuclear-power

Britannica. (2015). *Nuclear Reactor - Types of Reactors*. Retrieved from Encyclopædia Britannica: http://www.britannica.com/EBchecked/topic/421763/nuclear-reactor/307271/Containment-systems-and-major-nuclear-accidents#toc45776

CARIOU, S. (2010). *Couplage hydro-mécanique et transfert dans l'argilite de Meuse/Haute-Marne: approches expérimentale et multi-échelle. Materials and structures in mechanics.* Ecole des Ponts Paris.

CEA. (2014a). *Réacteurs nucléaires à caloporteur sodium - Pourquoi des réacteurs refroidis au sodium ?* Retrieved from Commissariat à l'énergie atomique et aux

énergies alternatives: http://www.cea.fr/content/download/147248/2694803/file/reacteurs-nucleaires-sodium-pourquoi-reacteurs-rapides-sodium.pdf

CEA. (2014b). *Réacteurs nucléaires à caloporteur sodium - La Technologie des RNR-Na.* Retrieved from Commissariat à l'énergie atomique et aux énergies alternatives: http://www.cea.fr/content/download/147251/2694812/file/reacteurs-nucleaires-sodium-technologie-RNR-Na.pdf

CEA. (2014c). *Le choix français : une recherche orientée sur la technologie des réacteurs à neutrons rapides (2/4)*. Retrieved from Commissariat à l'énergie atomique et aux énergies alternatives: http://www.cea.fr/energie/astrid-une-option-pour-la-quatrieme-generation/le-choix-francais-une-recherche-orientee-sur-l

CESCOTTO, S. (2011). *Cours de Mécanique du Solide.* Université de Liège.

CHARLIER, R. (2000). *Cours de Modélisation du comportement des géomatériaux.* Université de Liège.

CHARLIER, R. (2013). *Cours de Géotechnique et Infrastructures.* Université de Liège.

CHARLIER, R., COLLIN, F., GERARD, P., RADU, J.-P., & PARDOEN, B. (2013b). *Modélisation numérique de l'expérience SDZ pour l'Andra - Résultats de simulations.* Université de Liège - ArGEnCo.

CHARLIER, R., COLLIN, F., PARDOEN, B., TALANDIER, J., RADU, J.-P., & GERARD, P. (2013a). An unsaturated hydro-mechanical modelling of two in-situ experiments in Callovo-Oxfordian argillite. *Engineering Geology, 165*, pp. 46-63.

Chavant, C., & Fernandez, R. (2005). Evaluating the reliability of hydro-mechanical simulation : A benchmark of numerical techniques carried out by Research Group of MoMas. *2nd International Meeting Clays in Natural and Engineering Barriers for Radioactive Waste Confinement* (pp. 14-18). Tours, France: ANDRA.

CHENG, A. H.-D. (1997). Material coefficients of anisotropic poroelasticity. *International Journal of Rock Mechanics and Mining Sciences, 34*(2), pp. 199-205.

CHOPPIN, G. R., LILJENZIN, J.-O., & RYDBERG, J. (2002). *Radiochemistry and Nuclear Chemistry.* Butterworth-Heinemann.

COLLIN, F. (2013). *Cours de Géotechnique Expérimentale.* Université de Liège.

COLLIN, F. (2014). *Cours de Mecanique des Roches.* Université de Liège.

COLLIN, F. (2015). *Environmental Geotechnics.* University of Liège.

COLLIN, F. (2015). *Environmental Geotechnics Course.* University of Liège.

COPPOLANI, P. (2004). *La Chaudière des Réacteurs à Eau sous Pression.* EDP Sciences.

COUSSY, O. (2004). *Poromechanics.* New York: John Wiley.

CRUCHAUDET, M., NOIRET, A., TALANDIER, J., & ARMAND, G. (2010a). *Expérimentation SDZ—Bilan de la mise en place de l'instrumentation et des premières mesures à fin mars 2010.* Centre de Meuse/Haute-Marne: Tech. Rep. D.RP.AMFS.09.0087, ANDRA.

CRUCHAUDET, M., NOIRET, A., TALANDIER, J., GATMIRI, J., & ARMAND, G. (2010b). *OHZ en GED: EDZ initiale et évolution.* Centre de Meuse/Haute-Marne: Tech. Rep. D.RP.AMFS.11.0016, Andra.

DIEUDONNE, A.-C. (2011). *Stockage géologique du CO2: l'étanchéité des puits.* Université de Liège.

DUCHENE, L. (2013). *Cours de Méthodes Numériques Linéaires.* Université de Liège.

EDF. (2015). *EPR - Flamanville 3*. Retrieved from EDF: http://energie.edf.com/nucleaire/carte-des-centrales-nucleaires/presentation-48324.html

ENS. (2015). *Nuclear Fission*. Retrieved from European Nuclear Society.

EURIDICE. (2015). *HADES dans le contexte européen*. Retrieved from European Underground Research Infrastructure for Disposal of nuclear waste in Clay Environment (EURIDICE): http://www.euridice.be/fr/content/hades-dans-le-contexte-europ%C3%A9en

FRANCOIS, B., LABIOUSE, V., DIZIER, A., MARINELLI, F., CHARLIER, R., & COLLIN, F. (2012). Hollow cylinder tests on boom clay : Modelling of strain localization in the Anisotropic Excavation Damaged Zone. *Rock Mechanics and rock engineering, 47:71-86*.

Georgia State University. (2015). *Nuclear Binding Energy*. (Department of Physics and Astronomy) Retrieved from HyperPhysics: http://hyperphysics.phy-astr.gsu.edu/hbase/nucene/nucbin.html#c1

GERARD, P. (2011). *Impact des transferts de gaz sur le comportement poro-mécanique des matériaux argileux.* Université de Liège.

GERARD, P., CHARLIER, R., CHAMBON, R., & COLLIN, F. (2008). Influence of evaporation and seepage on the convergence of a ventilated cavity. *Water Resources Research, 44*(W00C02), pp. 1-16.

GERARD, P., LEONARD, A., MASEKANYA, J.-P., CHARLIER, R., & COLLIN, F. (2010). Study of the soil-atmosphere moisture exchanges through convective drying tests in non-isothermal conditions. *International Journal for Numerical and Analytical Methods, 34*(12), pp. 1297-1320.

GUILLON, T. (2011). *Comportement hydromécanique des argilites du Callovo-Oxfordien lors de cycles de desaturation-resaturation.* Instity National Polytechnique de Lorraine (INPL).

IAEA. (2015a). *Power Reactor Information System*. Retrieved from International Atomic Energy Agency: https://www.iaea.org/pris/

IAEA. (2015b). *Power Reactor Information System - Details of France*. Retrieved from International Atomic Energy Agency: https://www.iaea.org/PRIS/CountryStatistics/CountryDetails.aspx?current=FR

IEA. (2014). *Key World Energy Statistics.*

IEA. (2015). *Faqs : Nuclear*. Retrieved from International Energy Agency: http://www.iea.org/aboutus/faqs/nuclear/

JEWETT, J. W., & SERWAY, R. A. (2010). *Physics for Scientists and Engineers with Modern Physics* (8th ed.). Belmont, CA: International Edition.

LADEPECHE. (2008). *Tournemire. Un labo géant sous terre pour la sûreté nucléaire*. Retrieved from LADEPECHE.fr: http://www.ladepeche.fr/article/2008/09/27/478102-tournemire-un-labo-geant-sous-terre-pour-la-surete-nucleaire.html

LE FIGARO. (2013). *Nucléaire : un tunnel d'étude au Larzac*. Retrieved from Le Figaro.fr: http://www.lefigaro.fr/sciences/2013/04/23/01008-20130423ARTFIG00641-nucleaire-un-tunnel-d-etude-au-larzac.php

Le Monde. (2015). *Le Sénat fait revenir en force le nucléaire dans la loi de transition énergétique*. Retrieved from Le Monde: http://www.lemonde.fr/energies/article/2015/02/09/plan-le-senat-fait-revenir-en-force-le-nucleaire-dans-la-loi-de-transition-energetique_4572915_1653054.html

LEKHNITSKII, S. G. (1963). *Theory of Elasticity of an Anisotropic Elastic Body*. San Francisco: Holden-Day.

LEONARD, A., BLACHER, S., MARCHOT, P., & CRINE, M. (2002). *Use of X-Ray Microtomography to follow the convective heat drying of wastewater sludges.* Université de Liège.

LÉONARD, O. (2012). Course of Thermodynamique appliquée et introduction aux machines thermiques. ULg.

L'Express. (2014). *La loi sur la transition énergétique sera votée au Sénat début février*. Retrieved from L'Express: http://www.lexpress.fr/actualites/1/politique/la-loi-sur-la-transition-energetique-sera-votee-au-senat-debut-fevrier_1625521.html

MAGNENET, V., GIRAUD, A., & AUVRAY, C. (2011). About the effect of relative humidity on the indentation response of Meuse/Haute-Marne argillite. *Acta Geotecnica,* 6(3), pp. 155-166.

Ministère de France. (2014). *Les Installations Nucléaires en France*. Retrieved from Site officiel du Ministère de l'écologie, du développement durable et de l'énergie : http://www.developpement-durable.gouv.fr/Les-installations-nucleaires-en.html

Miny, L. (2013). *Etude expérimentale et numérique du comportement anisotrope de l'argile de Boom.* Université de Liège.

Panet, M., & Guellec, P. (1974). Contribution à l'étude du soutènement d'un tunnel à l'arrière du front de taille. *Advances in rock mechanics, Proceedings of the 3rd International Congress on Rock Mechanics. II.* Denver: International Society Rock Mechanics.

PARDOEN, B., LEVASSEUR, S., & COLLIN, F. (2014). Using Local Second Gradient Model and Shear Strain Localisation to Model the Excavation Damaged Zone in Unsaturated Claystone. *Rock Mechanics & Rock Engineering, 48*, pp. 691-714.

PARDOEN, B., SEYEDI, D. M., & COLLIN, F. (2015). *Shear banding modelling in cross-anisotropic rocks.* University of Liège.

PHAM, Q., VALES, F., MALINSKY, L., MINH, D. N., & GHARBI, H. (2007). Effects of desaturation–resaturation on mudstone. *Physics and Chemistry of the Earth, 32*, pp. 646-655.

SCF. (2015). *Matières Premières*. Retrieved from Société Chimique de France: http://www.societechimiquedefrance.fr/extras/donnees/metaux/ura/texura.htm

Siemens. (2012). *Factsheet : One year after Fukushima – Germany's path to a new energy policy* . Retrieved from Siemens Global Website: http://www.siemens.com/press/pool/de/feature/2012/corporate/2012-03-energiewende/factsheet-e.pdf

Texas State Energy Conservation Office. (2015). *Nuclear Energy*. Retrieved from Energy Education Programs: http://www.energyeducation.tx.gov/energy/section_1/topics/forms_of_energy/nuclear_energy.html

The Guardian. (2011). *Berlusconi's nuclear power plans crushed*. Retrieved from The Guardian: http://www.theguardian.com/world/2011/jun/13/berlusconi-nuclear-power

USNRC. (2014). *Stages of the Nuclear Fuel Cycle*. Retrieved from United States Nuclear Regulatory Commission: http://www.nrc.gov/materials/fuel-cycle-fac/stages-fuel-cycle.html

WAN, M., DELAGE, P., MENACEUR, H., TANG, A., & TALANDIER, J. (2014). Water Retention Properties of the Callovo-Oxfordian Claystone. *Journées Nationales de Géotechnique et de Géologie de l'Ingénieur*.

WANG, J.-J., ZHANG, H.-P., ZHANG, L., & LIANG, Y. (2013). Experimental study on self-healing of crack in clay seepage barrier. *Engineering Geology, 159*, pp. 31-35.

Wikipedia. (2015). *Heap Leaching*. Retrieved from Wikipedia: http://en.wikipedia.org/wiki/Heap_leaching

WILEVEAU, Y., & BERNIER, F. (2008). Similarities in the hydromechanical response of Callovo-Oxfordian clay and Boom Clay during gallery excavation. *Physics and Chemistry of the Earth, 33*(1).

WNA. (2012). *Uranium Mining Overview*. Retrieved from World Nuclear Association: http://www.world-nuclear.org/info/Nuclear-Fuel-Cycle/Mining-of-Uranium/Uranium-Mining-Overview/

WNA. (2014a). *The many uses of nuclear technology*. Retrieved from World Nuclear Association: http://www.world-nuclear.org/info/Non-Power-Nuclear-Applications/Overview/The-Many-Uses-of-Nuclear-Technology/

WNA. (2014b). *Nuclear Power in the World Today*. Retrieved from World Nuclear Association: http://www.world-nuclear.org/info/Current-and-Future-Generation/Nuclear-Power-in-the-World-Today/

WNA. (2014c). *The Nuclear Fuel Cycle*. Retrieved from World Nuclear Association: http://www.world-nuclear.org/info/Nuclear-Fuel-Cycle/Introduction/Nuclear-Fuel-Cycle-Overview/

WNA. (2014d). *Uranium production figures, 2003-2013*. Retrieved from World Nuclear Association: http://www.world-nuclear.org/info/Facts-and-Figures/Uranium-production-figures/

WNA. (2015a). *Nuclear Power Reactors*. Retrieved from World Nuclear Association: http://www.world-nuclear.org/info/Nuclear-Fuel-Cycle/Power-Reactors/Nuclear-Power-Reactors/

WNA. (2015b). *Nuclear Power in France*. Retrieved from World Nuclear Association: http://www.world-nuclear.org/info/Country-Profiles/Countries-A-F/France/

8 Appendix

The following sections give more details on the experimental measures, which the numerical results are compared to. The descriptions and figures are based on the internal reports of ANDRA [CRUCHAUDET, et al., 2010a] and [CRUCHAUDET, et al., 2010b].

8.1 Appendix 1: Climatic Measures in the SDZ Zone

The measures of temperature and hygrometry were realised in the SDZ1261 to SDZ1264 sections, located in the uncoated SDZ zone (i.e. the first 7.2 m cf. FIG). The characteristics of the sensors are given in Table 29.

Units Measured	Range	Precision
Temperature	-30°C to +70°C	±0.3°C
Relative Humidity	0% to 100%	±2%

Table 29: Characteristics of the climatic sensors

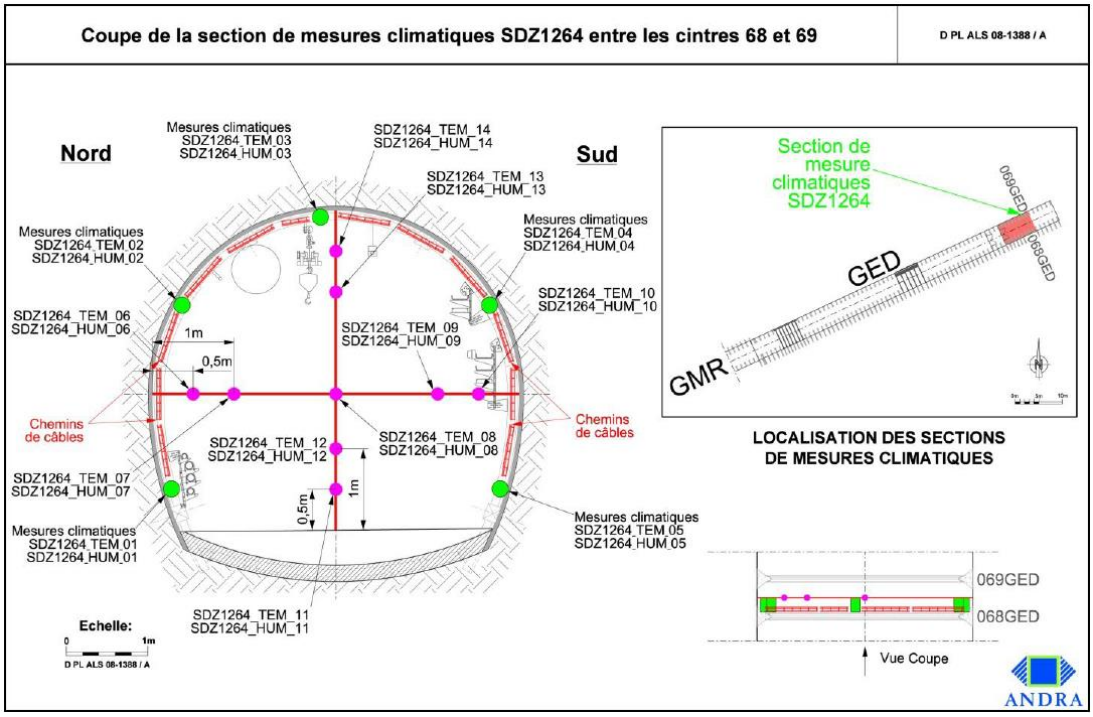

Figure 83: Position of the climatic sensors at the SDZ1264 section.

Figure 83 shows how the several sensors are placed in the SDZ1264 section. There are 5 sensors (01 to 05 in green) located at the rock wall and 9 others (06 to 14 in fuchsia) located on metallic bars transversal to the rock wall. More precisely, the 9 sensors located in the cavity of gallery can be found at the centre, at 0.5 m or at 1 m from the rock wall. The SDZ1261 section has a similar profile.

In the same way, Figure 84 shows how the several sensors are placed in the SDZ1263 section. Only the first 5 sensors (01 to 05 in green) located at the rock wall are present. The SDZ1262 section has a similar profile.

Sensors 01 to 05 were installed on 09/01/2009, whereas sensors 06 to 14 were put in place on 06/08/2009.The data's are available until 10/02/2015. Figure 85 to Figure 88 display the time evolution of the temperature and Figure 89 to Figure 92 display the time evolution of the hygrometry for the 4 climatic sections. Their trend is explained at SECTION

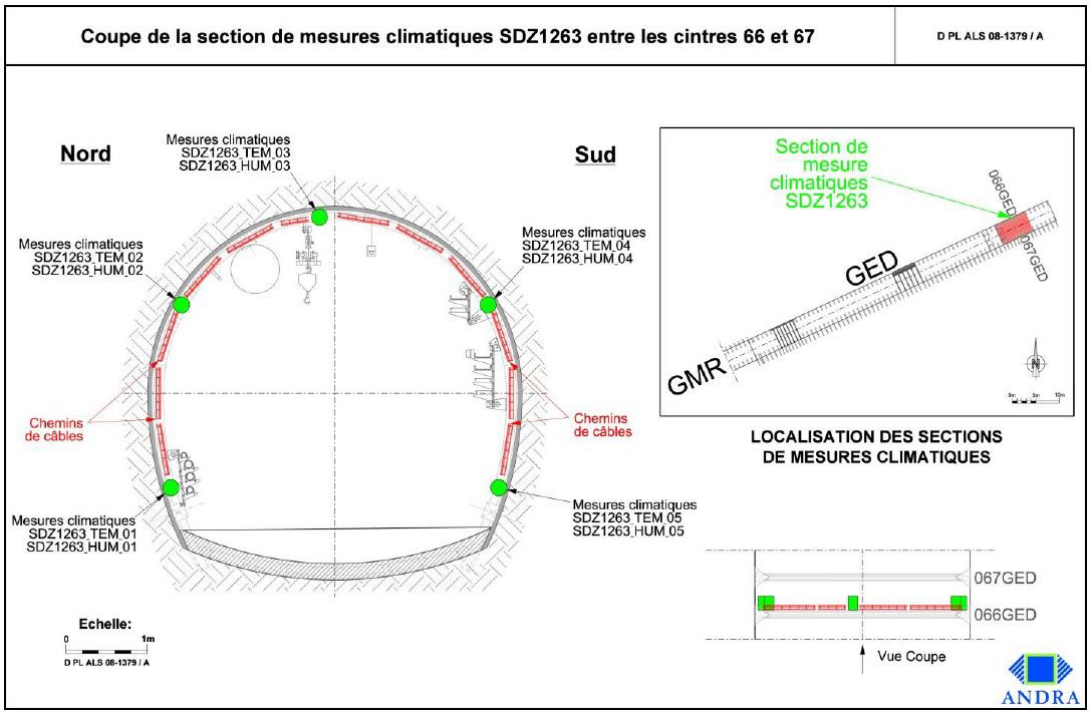

Figure 84: Position of the climatic sensors at the SDZ1263 section.

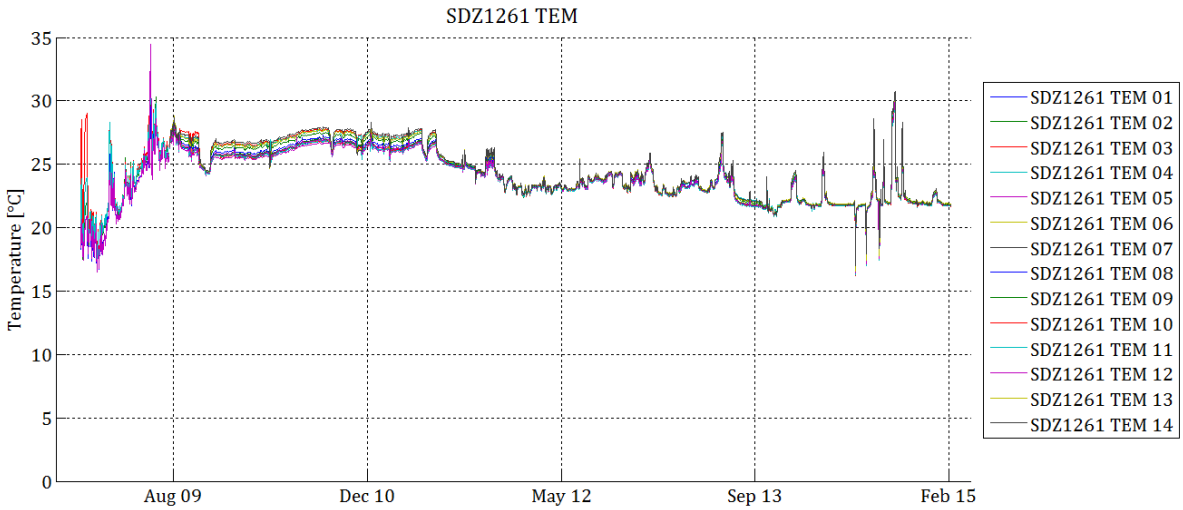

Figure 85: Evolution of the temperature at the SDZ1261 climatic section.

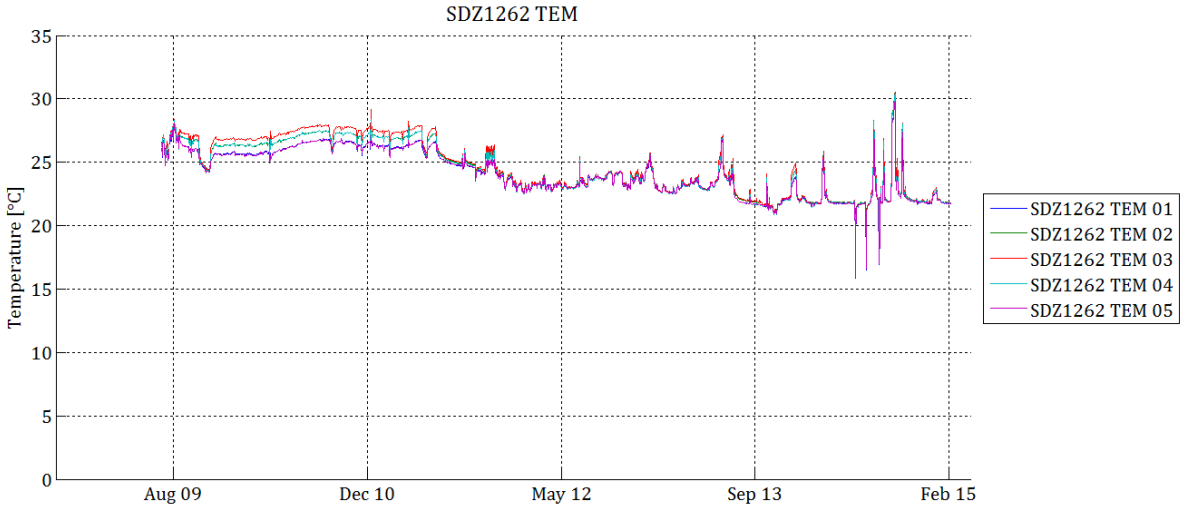

Figure 86: Evolution of the temperature at the SDZ1262 climatic section.

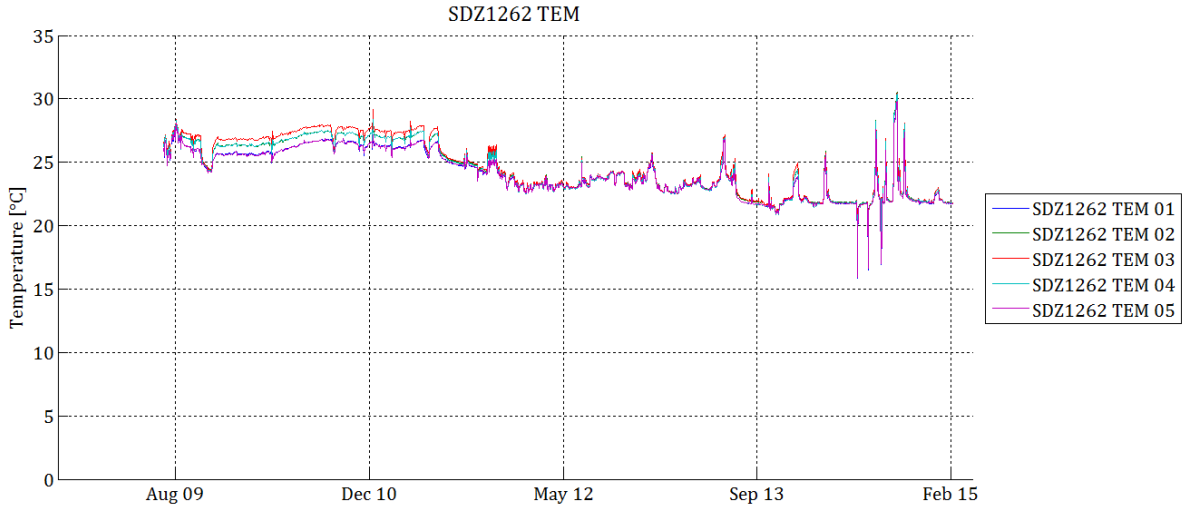

Figure 87: Evolution of the temperature at the SDZ1263 climatic section.

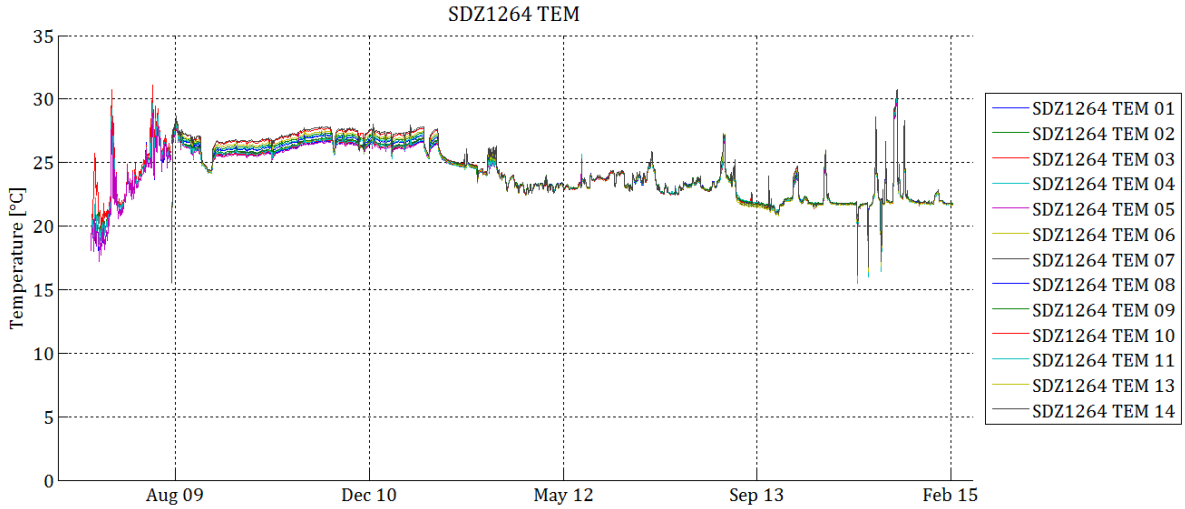

Figure 88: Evolution of the temperature at the SDZ1264 climatic section.

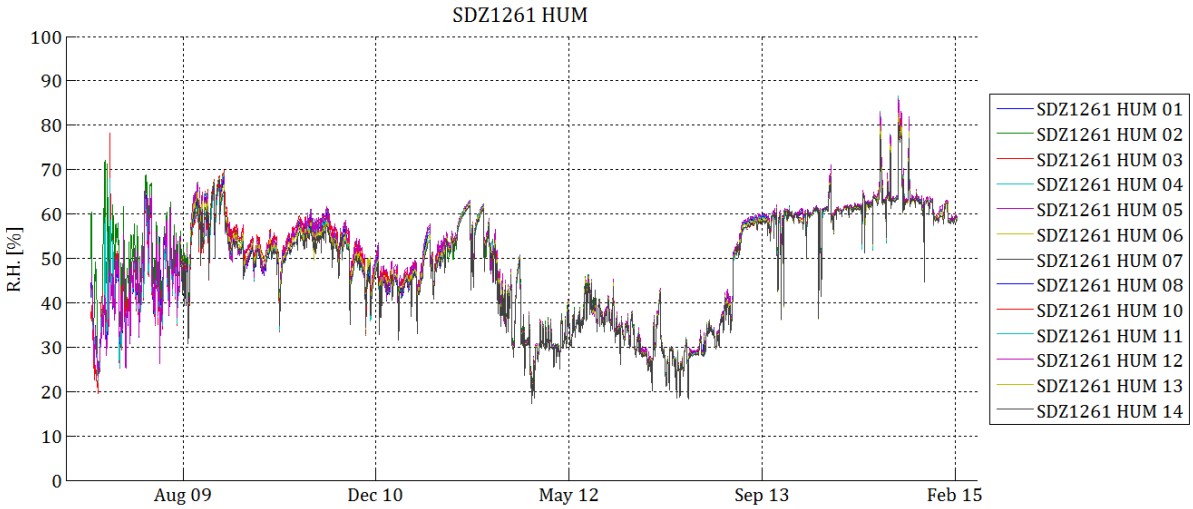

Figure 89: Evolution of the relative humidity at the SDZ1261 climatic section.

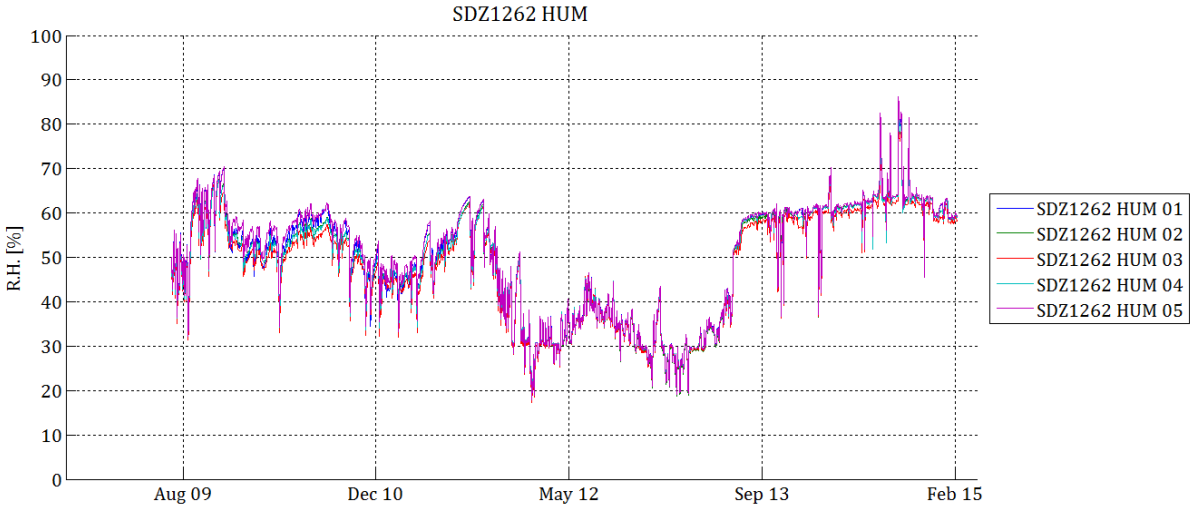

Figure 90: Evolution of the relative humidity at the SDZ1262 climatic section.

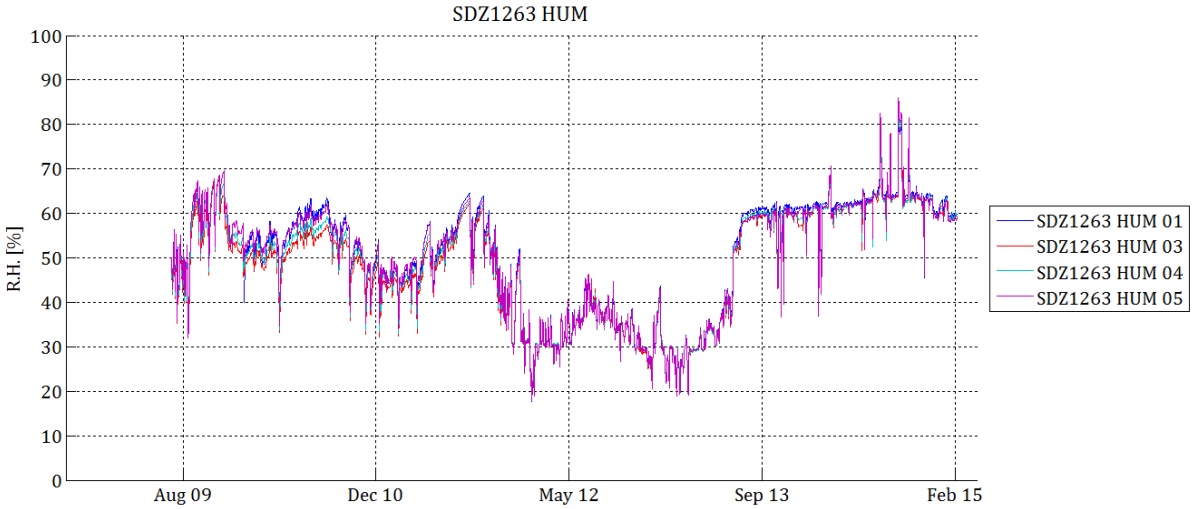

Figure 91: Evolution of the relative humidity at the SDZ1263 climatic section.

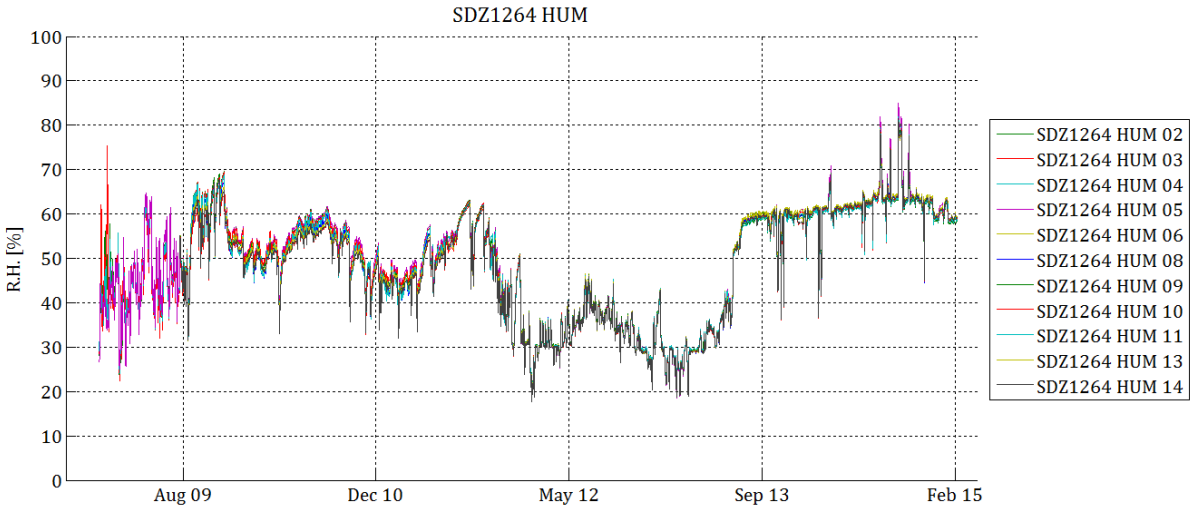

Figure 92: Evolution of the relative humidity at the SDZ1264 climatic section.

8.2 Appendix 2: Pressure Measures in the SDZ Drills

Water pressure measures were taken in the drills located in the uncoated zone of the gallery. The section has 4 drills: SDZ1241 to SDZ1244 (Figure 93). The first 3 drills have each 6 points of measurement which are placed from 0.5 to 6 m from the gallery. The SDZ1244 drill is dedicated to monitoring water pressure further away. It has 5 points of measurements and the farthest is at 20 m.

Figure 94 to Figure 97 display the time evolution of the water pressure for the 4 drills. The first measures were taken on 23/06/2009. The sensors are not able to measure negative values of the interstitial pressure. Thus, they cannot characterise the desaturation phenomenon within the rock. As a result, the experimental measures which should supposedly be negative (i.e. from sensors located close to the rock wall) are instead displayed with values close to 0.

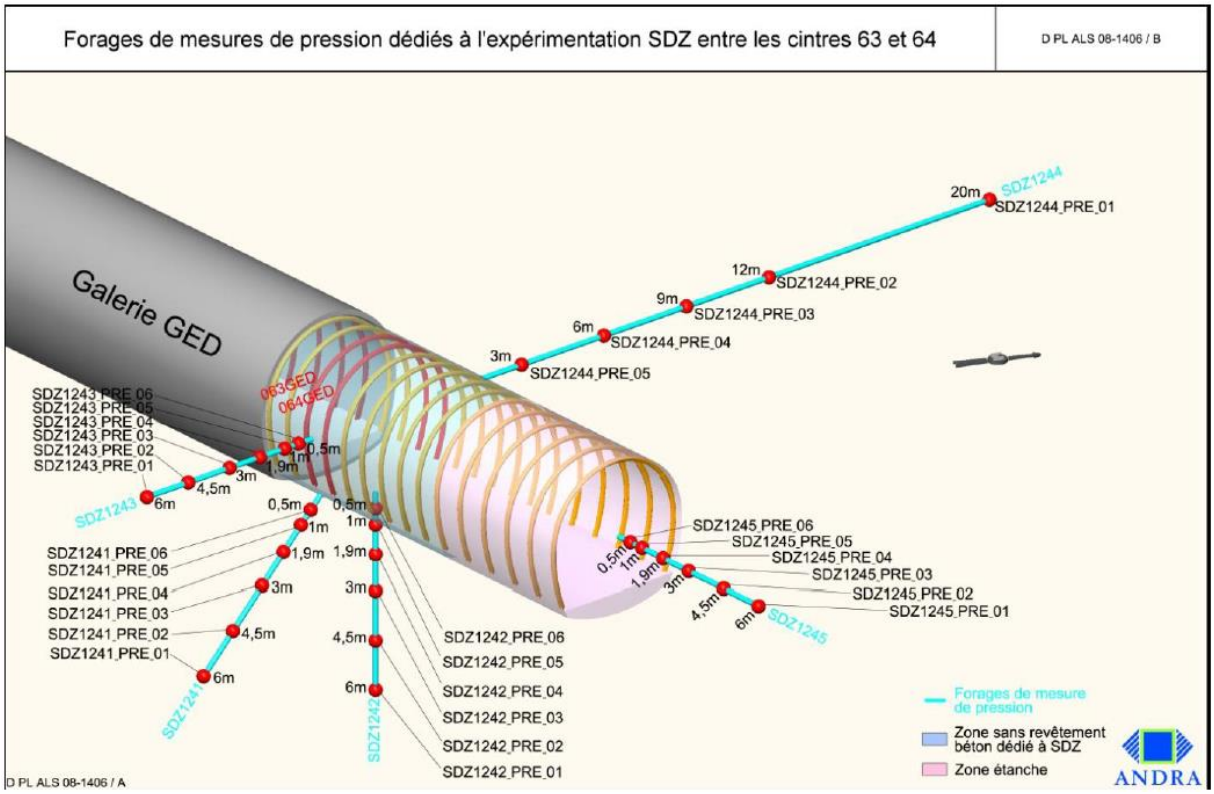

Figure 93: Location of the SDZ drills dedicated to pressure measures.

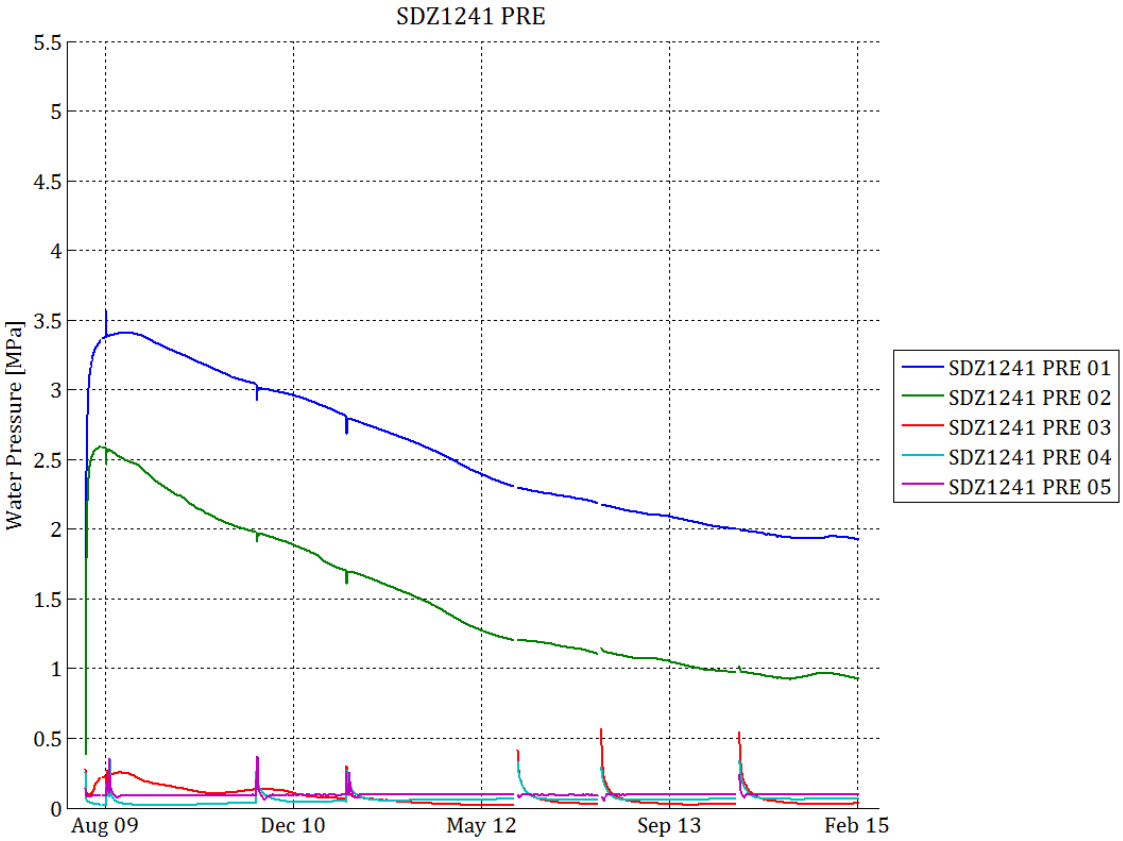

Figure 94: Evolution of the water pressure in the SDZ1241 drill, 45° downwards.

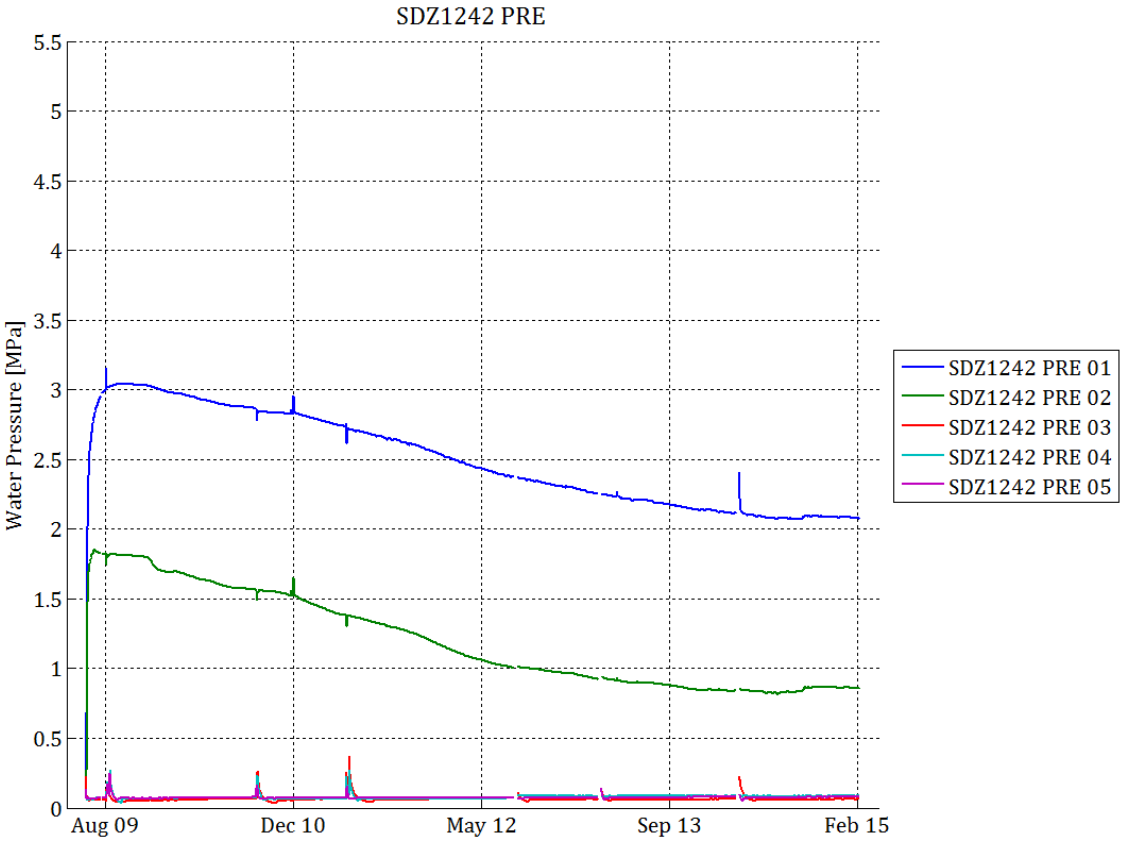

Figure 95: Evolution of the water pressure in the SDZ1242 drill, vertically downwards.

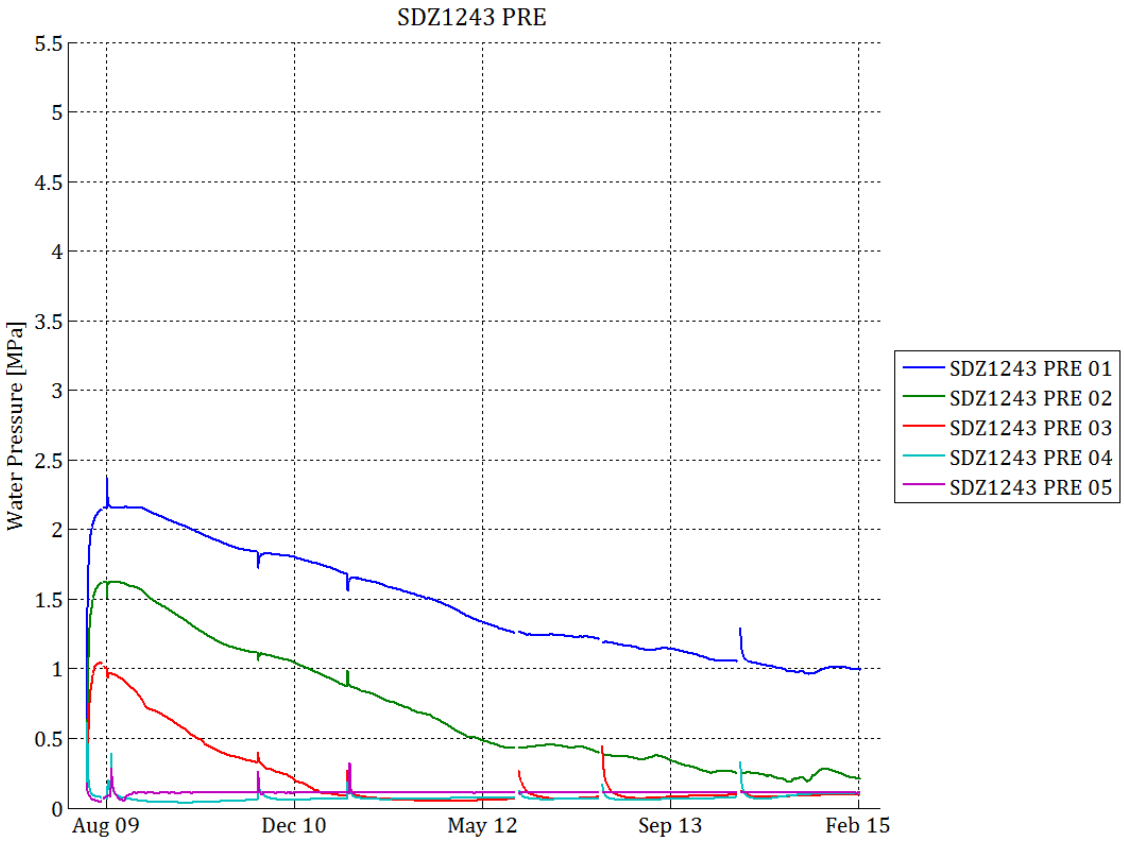

Figure 96: Evolution of the water pressure in the SDZ1243 drill, horizontal.

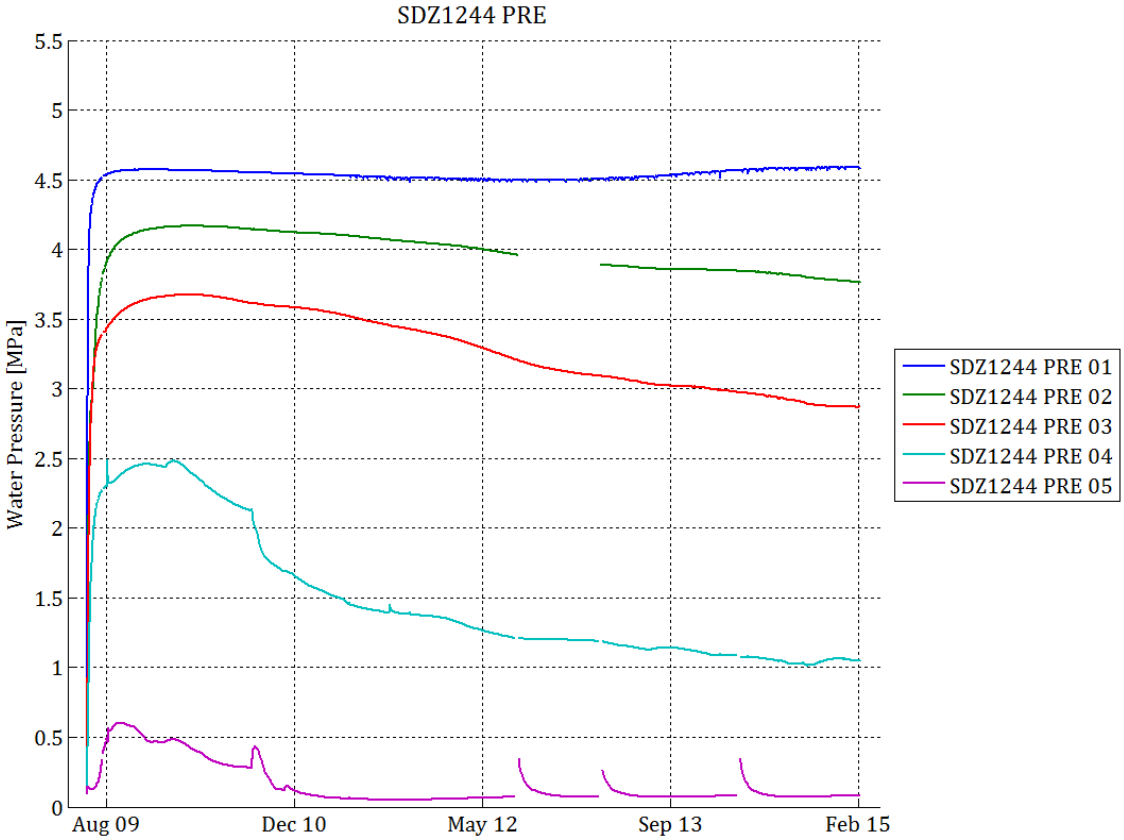

Figure 97: Evolution of the water pressure in the SDZ1244 drill, horizontal 'far'.

8.3 Appendix 3: Water Content Measures in the SDZ Drills

Measures of water content were taken on samples of Callovo-Oxfordian argillite. These samples were taken from the drills in the uncoated zone of the SDZ gallery (Figure 98). Table 2 describes the characteristics of those drills. The results are available at Figure 99 to Figure 102.

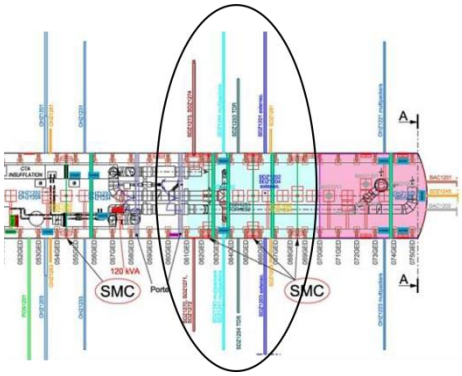

Figure 98: Water content: location of the drills in the SDZ zone.

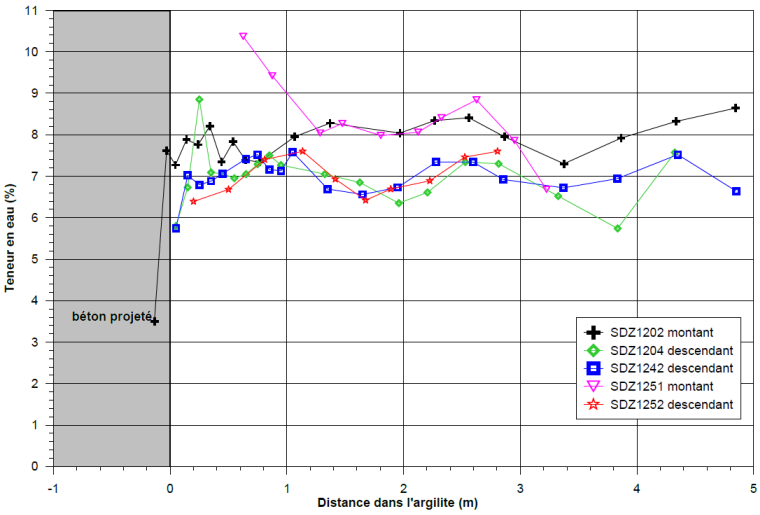

Figure 99: Water content in the vertical direction.

Drill	Orientation	Date	Length [m]	Time since excavation
SDZ1270	Horizontal	22-23/12/2008	5.6	15 days
SDZ1271	Horizontal	04-05/02/2009	5.05	2 months
SDZ1272	Horizontal	02/03/2009	4.8	3 months
SDZ1273	Horizontal	09/04/2009	5.05	4 months
SDZ1274	Horizontal	03/06/2009	5	6 months
SDZ1275	Horizontal	19/01/2010	6.05	13 months
SDZ1201	Horizontal	07/2009	5.1	7 months
SDZ1203	Horizontal	07/2009	4.6	7 months
SDZ1243	Horizontal	07/2009	4.6	7 months
SDZ1244	Horizontal	07/2009	5	7 months
SDZ1253	Horizontal	07/2009	2.6	7 months
SDZ1254	Horizontal	07/2009	2.6	7 months
SDZ1202	Vertical upwards	07/2009	4.85	7 months
SDZ1204	Vertical downwards	07/2009	4.3	7 months
SDZ1242	Vertical downwards	07/2009	4.85	7 months
SDZ1251	Vertical upwards	07/2009	3.2	7 months
SDZ1252	Vertical downwards	07/2009	2.8	7 months
SDZ1278	Horizontal	03/12/2010	3.25	24 months
SDZ1279	Horizontal	06/01/2011	4.4	25 months
SDZ1285	Horizontal	13/04/2011	6.05	29 months
SDZ1286	Horizontal	28/03/2012	6.4	40 months
SDZ1287	Horizontal	28/06/2012	6.8	43 months
SDZ1288	Horizontal	25/02/2013	5.9	51 months

Table 30: Characteristics of the drills measuring water content in the uncoated zone of the SDZ gallery.

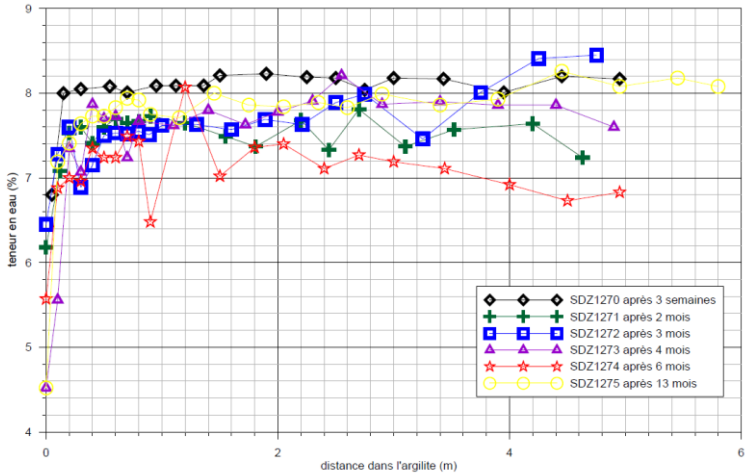

Figure 100: Water content in the horizontal direction (1).

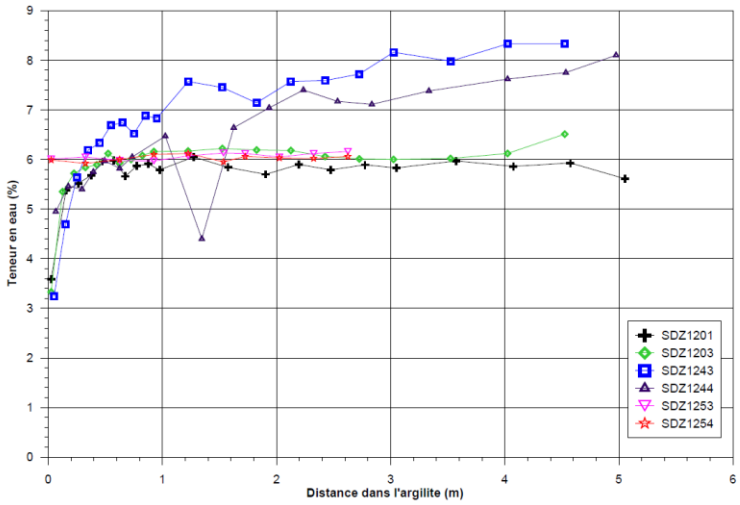

Figure 35 Mesures de teneur en eau en forages horizontaux

Figure 101: Water content in the horizontal direction (2).

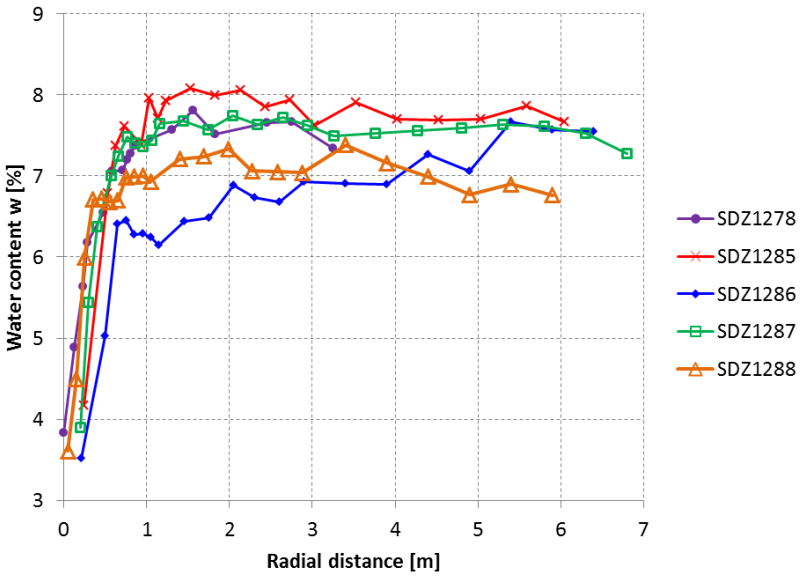

Figure 102: Water content in the horizontal direction (3).

8.4 Appendix 4: Convergence Measures in SMC sections

The convergence of the gallery is monitored at 3 sections (Section de Mesure de Convergence, SMC), each located in the SDZ zone (Figure 103). The measurements are realised by means of convergence measuring devices. Each section has two of them, placed transversally to the rock wall as shown on Figure 105. The subscripts '01' and '02' correspond respectively to the horizontal and vertical positions of the devices (Figure 104).

In addition to the convergence measuring devices, manual measures of the convergence were taken at these sections (D, E and F) and at 3 others (A, B and C) located in the GED gallery (i.e. out of the SDZ test zone). Table 31 sums up the details of those convergence measurements.

Figure 106 displays the results for the convergence measures obtained manually. Figure 107 and Figure 108 show respectively the vertical and horizontal convergence measured manually. We see major differences between the measures taken manually (which last until around 800 days) and the ones taken with the devices (which last until around 1200 days). Let us note that some data's (OHZ120C to OHZ120F) were interrupted before others due notably to the installation of the ventilation duct and the closing of the SDZ zone.

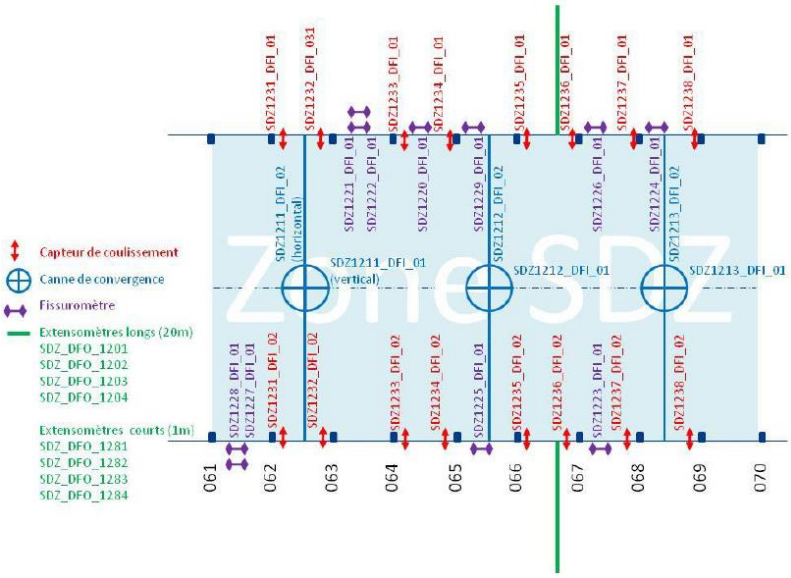

Figure 103: Location of the mechanical measures in the SDZ zone. The convergence measuring devices are labelled in blue.

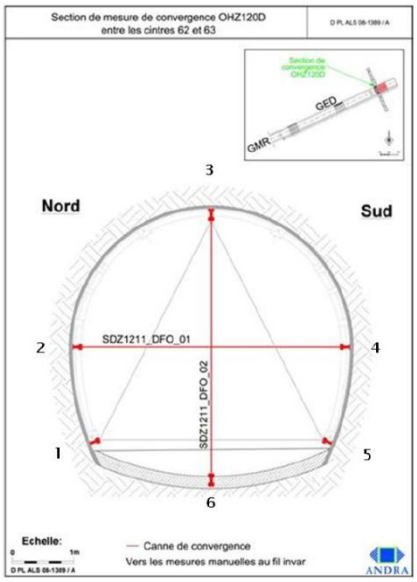

Figure 104: Sketch of the section and positions of de devices dedicated to the convergence measurements.

Figure 105: Convergence measuring devices in the gallery.

Name	Section	Location	Measurement Type
OHZ120A	SMC OHZ120A	GED Gallery	Manual
OHZ120B	SMC OHZ120B	GED Gallery	Manual
OHZ120C	SMC OHZ120C	GED Gallery	Manual
OHZ120D	SMC OHZ120D	SDZ Zone	Manual
OHZ120E	SMC OHZ120E	SDZ Zone	Manual
OHZ120F	SMC OHZ120F	SDZ Zone	Manual
SDZ1211_DFO_01	SMC OHZ120D	SDZ Zone	Conv. Measuring Device
SDZ1211_DFO_02	SMC OHZ120D	SDZ Zone	Conv. Measuring Device
SDZ1212_DFO_01	SMC OHZ120E	SDZ Zone	Conv. Measuring Device
SDZ1212_DFO_02	SMC OHZ120E	SDZ Zone	Conv. Measuring Device
SDZ1213_DFO_01	SMC OHZ120F	SDZ Zone	Conv. Measuring Device
SDZ1213_DFO_02	SMC OHZ120F	SDZ Zone	Conv. Measuring Device

Table 31: Characteristics of the drills measuring water content in the uncoated zone of the SDZ gallery.

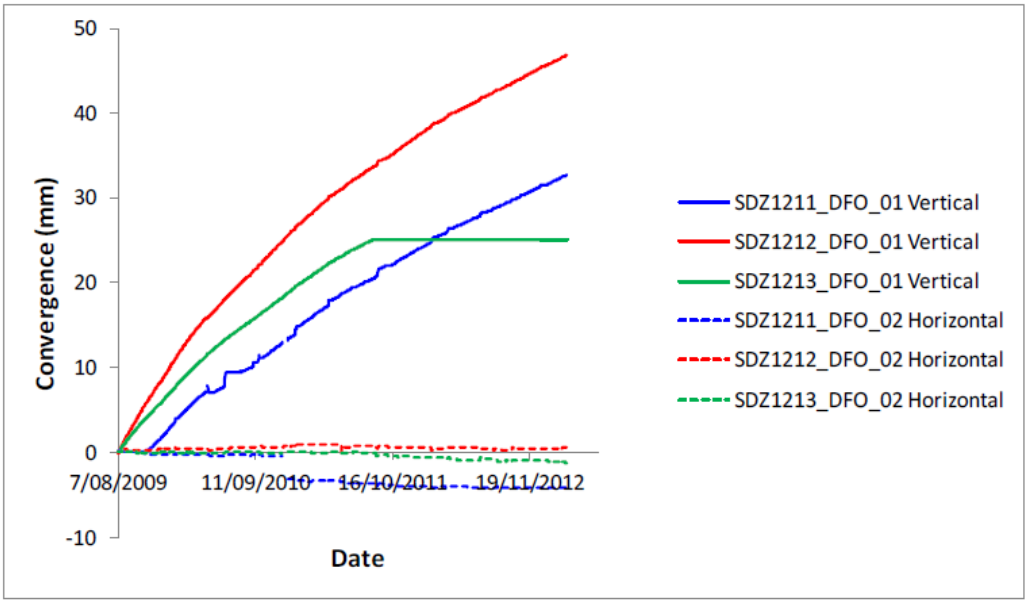

Figure 106: Measures obtained from the convergence measuring devices since 07/08/2009.

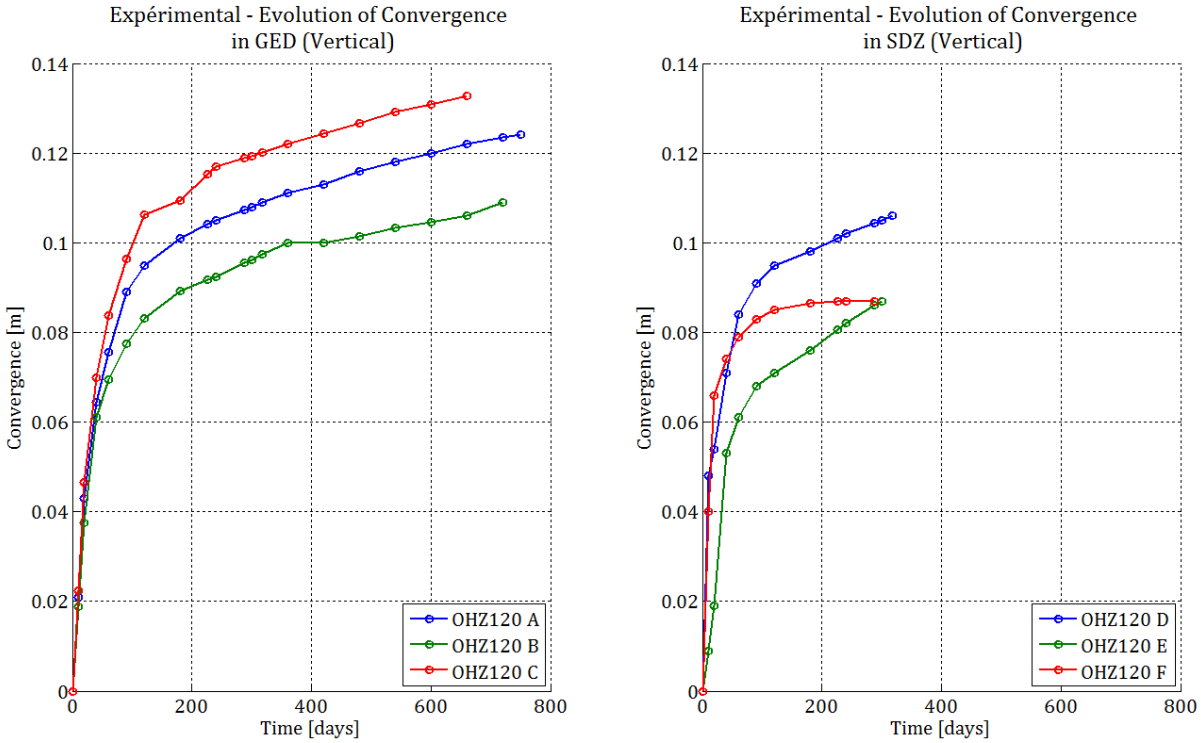

Figure 107: Measures of the vertical convergence obtained manually.

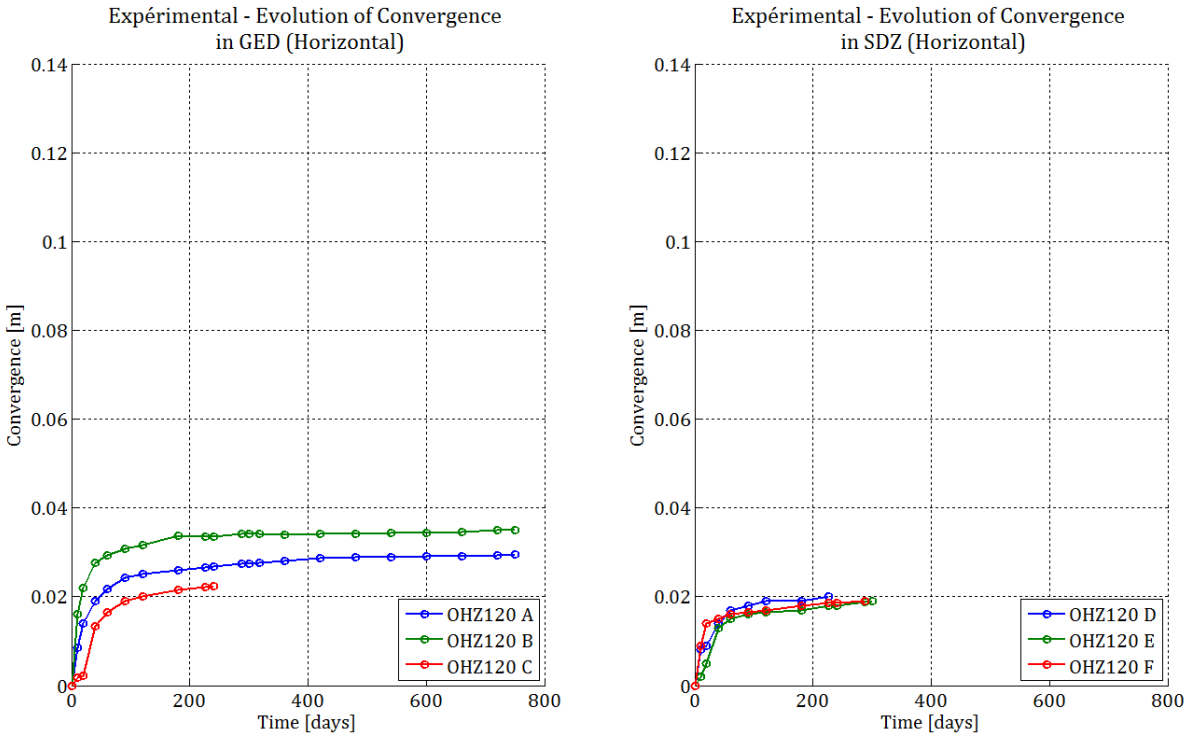

Figure 108: Measures of the horizontal convergence obtained manually.

8.5 Appendix 5: Convergence Measures in SDZ drills

The convergence of the gallery is also monitored in SDZ1201 to SDZ1204 drills by means of extensometers. Each extensometer has 7 points of measurement anchored at 1, 2, 3.5, 5, 8, 15 and 20 m from the rock wall (Figure 109).

The principle of these measures is displayed at Figure 110. The head of the extensometer (point 0) located at the rock wall is considered to be the reference point. The distance between point 0 and one of the points of measures (from 1 to 7) gives the displacement of the rock formation. For instance, the notation '04' corresponds to the measure between point 0 and point 4.

Figure 111 to Figure 114 give the time evolution of the convergence of the rock formation horizontally (SDZ1201 and SDZ1203) and vertically (SDZ1202 and SDZ1204). The values available last from 18/06/2009 until 10/02/2015 (i.e. about 2200 days).

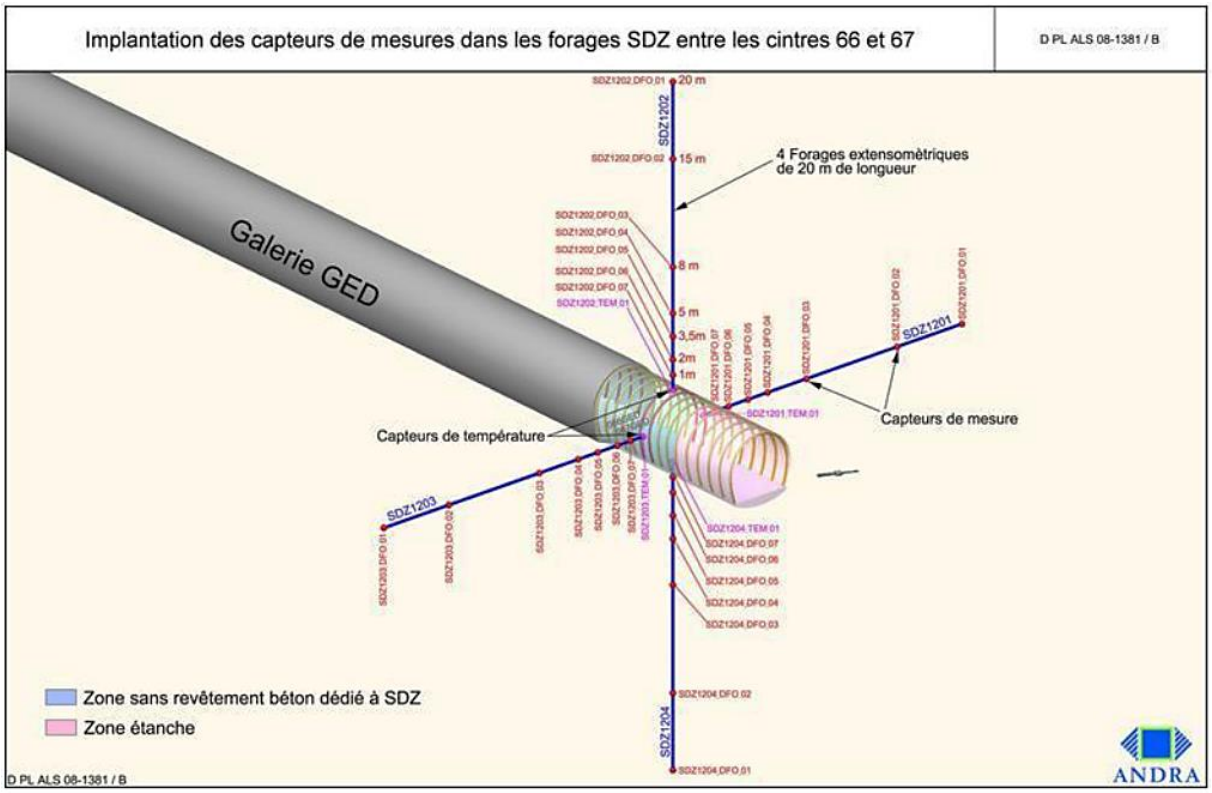

Figure 109: Location of the drills measuring the convergence in the SDZ zone.

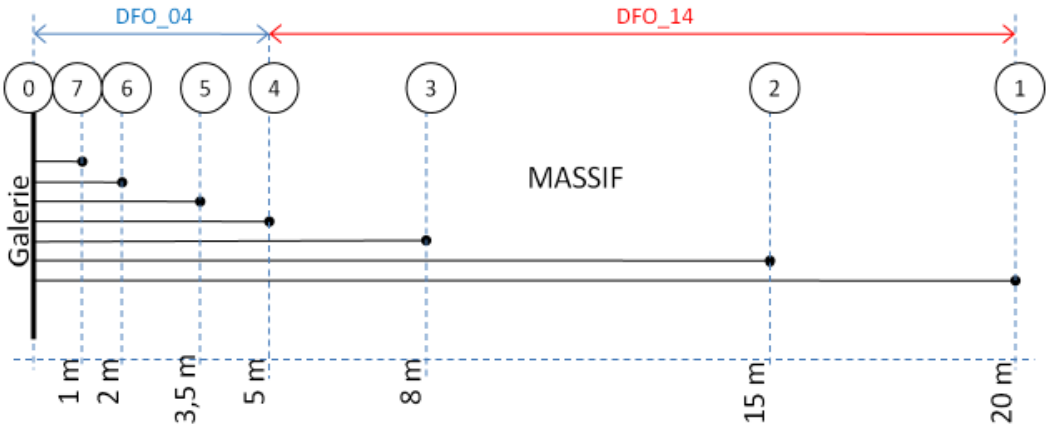

Figure 110: Schematic representation of an extensometer.

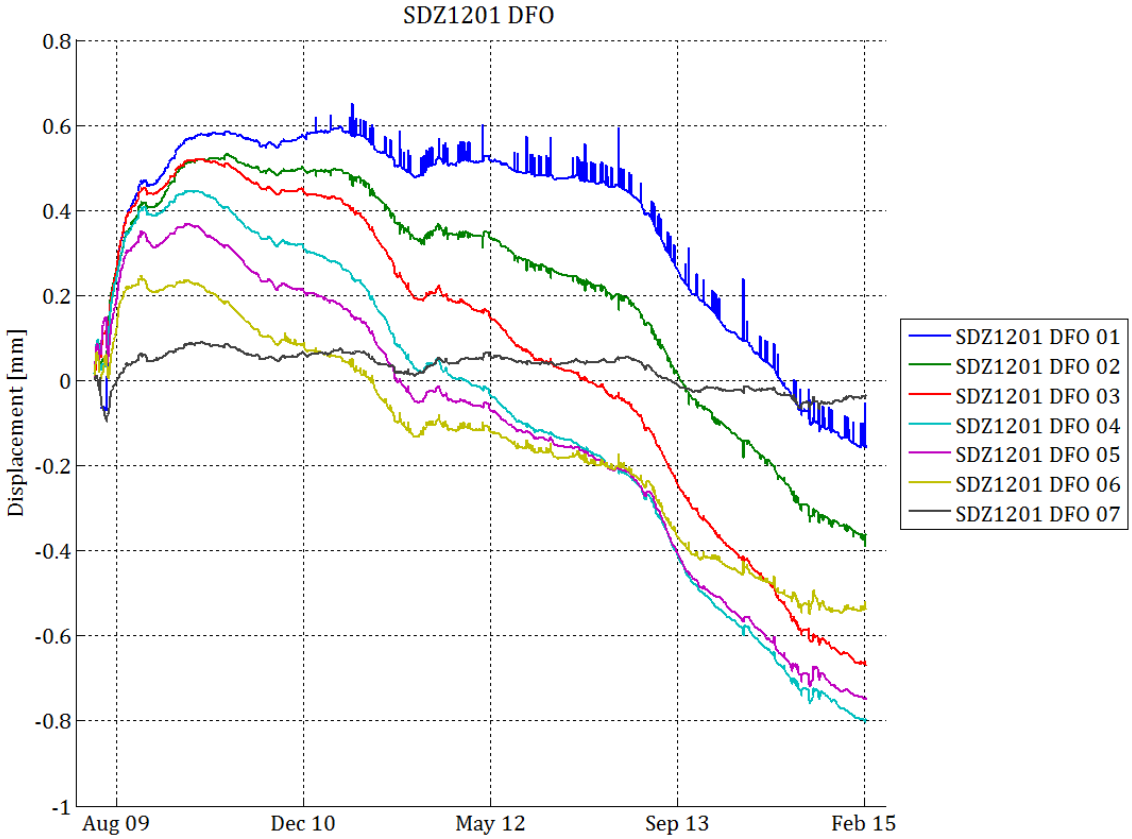

Figure 111: Measures of the horizontal convergence obtained with extensometers.

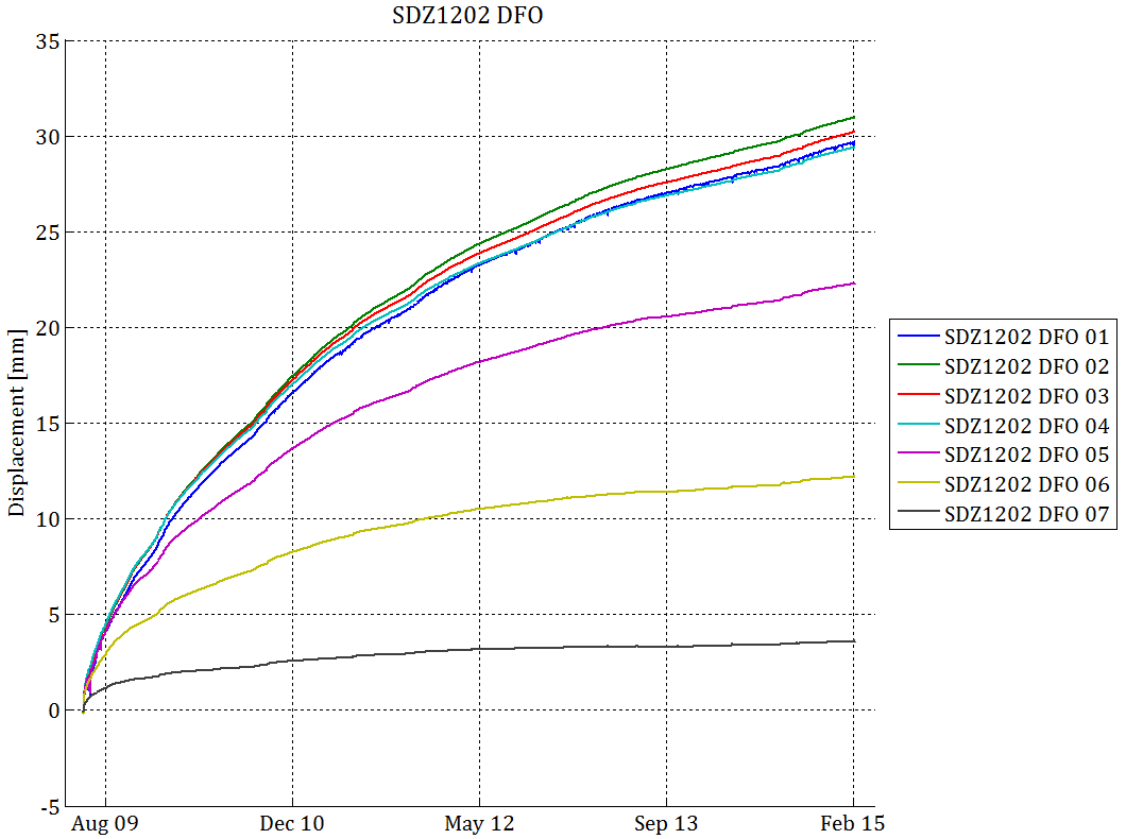

Figure 112: Measures of the vertical convergence obtained with extensometers.

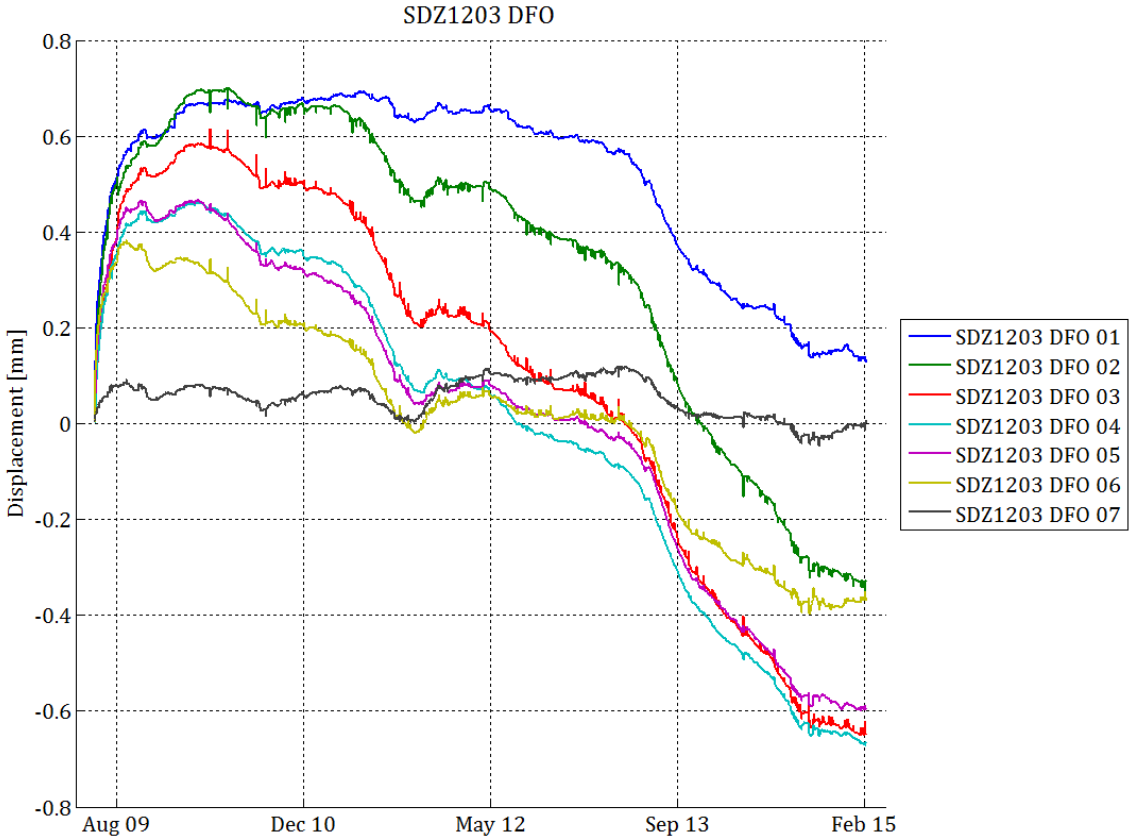

Figure 113: Measures of the horizontal convergence obtained with extensometers.

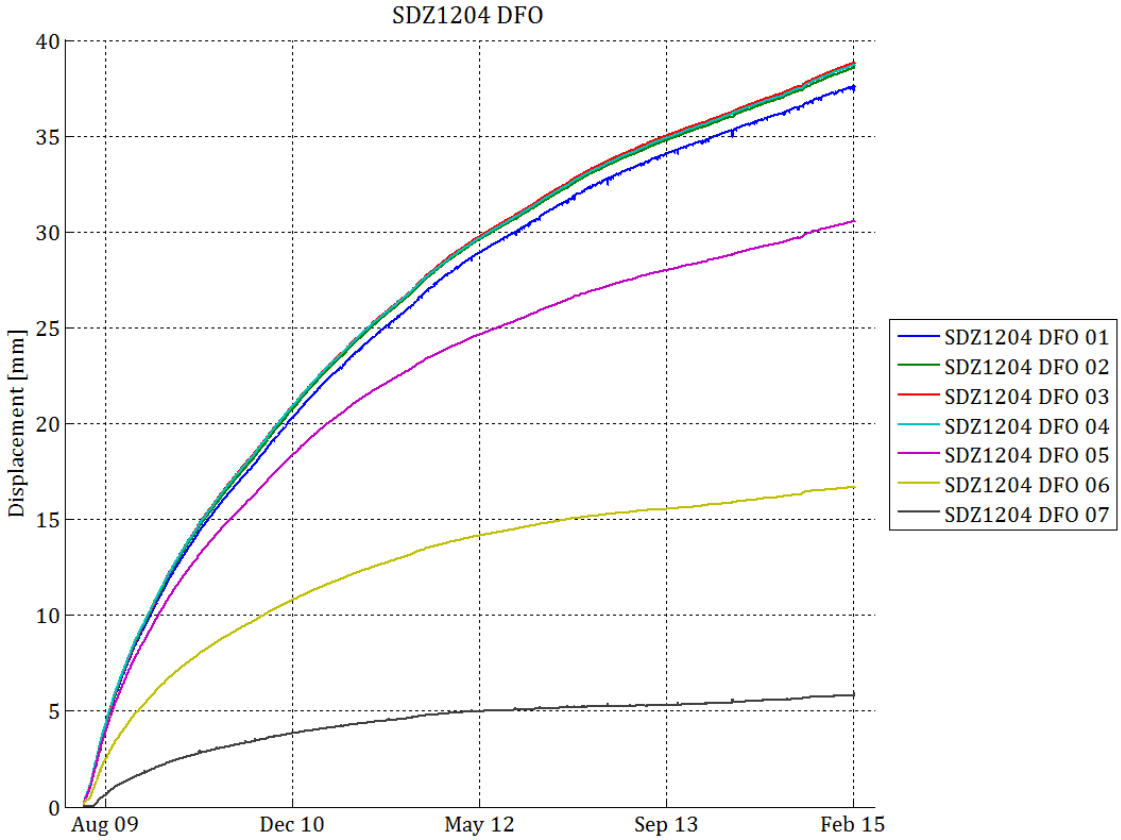

Figure 114: Measures of the horizontal convergence obtained with extensometers.

8.6 Appendix 6: Finite Elements Used in the Modelling

The meshing is mainly composed of classical quadrilateral 2-D elements. For both flow and mechanical descriptions, the elements are defined by 8 nodes and 4 integration points (Gauss points). The flow description is related to the water, air and temperature, while the mechanical consists in the displacements. Therefore, in 2D, the degrees of freedom considered are (order used in the finite element code LAGAMINE):

1) The horizontal displacement
2) The vertical displacement
3) The water pressure
4) The gas pressure
5) The temperature

In isoparametric elements, the interpolation functions are given as follows:

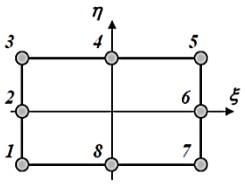

$$h^1(\xi,\eta) = -\frac{1}{4}(1-\xi)(1-\eta)(\xi+\eta+1)$$
$$h^2(\xi,\eta) = \frac{1}{2}(1-\xi)(1-\eta^2)$$
$$h^3(\xi,\eta) = -\frac{1}{4}(1-\xi)(1+\eta)(\xi-\eta+1)$$
$$h^4(\xi,\eta) = \frac{1}{2}(1+\eta)(1-\xi^2)$$
$$h^5(\xi,\eta) = \frac{1}{4}(1+\xi)(1+\eta)(\xi+\eta-1)$$
$$h^6(\xi,\eta) = \frac{1}{2}(1+\xi)(1-\eta^2)$$
$$h^7(\xi,\eta) = \frac{1}{4}(1+\xi)(1-\eta)(\xi-\eta-1)$$
$$h^8(\xi,\eta) = \frac{1}{2}(1-\eta)(1-\xi^2)$$

Figure 115: Isoparametric description [DUCHENE, 2013]

In addition to that, the water and vapour exchanges are modelled through FMIVP elements. They are associated with a classical quadrilateral 2-D finite element, and are defined by four nodes (Figure 116). While the first three nodes (N1, N2 and N3) intervene in the scope of the spatial discretisation of the pore water pressure distribution along the boundary, the fourth node (N4) defines the relative humidity within the cavity. The position of the latter does not influence the water exchanges

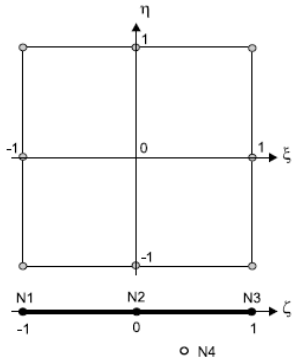

Figure 116: 2-D finite element and boundary element in isoparametric description. [GERARD, et al., 2008]

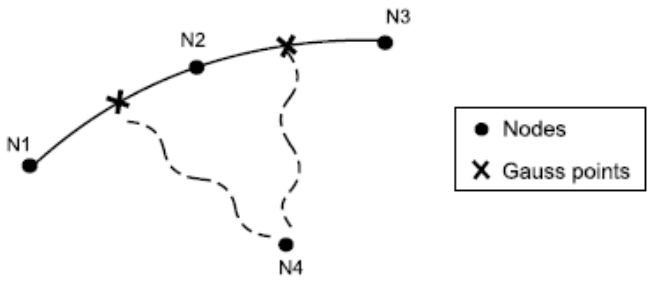

Figure 117: Boundary finite element description [GERARD, et al., 2008]

8.7 Appendix 7: Anisotropy of Mechanical parameters (SET2)

According to Equation 74, the values are [PARDOEN, et al., 2015]:

$$c = f(c_0, A_{11}, b_1, l_2) \quad with \quad \begin{cases} c_0 = 4.10\ [MPa] \\ A_{11} = 0.1171\ [-] \\ b_1 = 14.236\ [-] \end{cases}$$

Nonetheless, these values were determined considering isotropic initial stresses ($\sigma_{H;0} = \sigma_{v;0}$), which does not correspond to our case (cf. section 5.1.2). The following table shows the consequences of such hypotheses by comparing the cases of isotropic initial stresses with ours.

	Isotropic Initial Stresses	**Initial Stresses of this work**
	$\sigma_{11;0} = \sigma_{22;0} = \sigma_{33;0}$	$\sigma_{22;0} = \sigma_{\perp;0} = 15.6\ MPa$ $\sigma_{11;0} = \sigma_{33;0} = \sigma_{\parallel;0} = 12.0\ MPa$
$\sigma_{ij;0} = \begin{bmatrix} \sigma_{11;0} & 0 & 0 \\ 0 & \sigma_{22;0} & 0 \\ 0 & 0 & \sigma_{33;0} \end{bmatrix}$	$\sigma_{ij;0} = \begin{bmatrix} \sigma_0 & 0 & 0 \\ 0 & \sigma_0 & 0 \\ 0 & 0 & \sigma_0 \end{bmatrix}$	$\sigma_{ij;0} = \begin{bmatrix} \sigma_{\parallel;0} & 0 & 0 \\ 0 & \sigma_{\perp;0} & 0 \\ 0 & 0 & \sigma_{\parallel;0} \end{bmatrix}$
$l_{2;0} = \sqrt{\frac{(\sigma_{22;0})^2}{(\sigma_{11;0})^2 + (\sigma_{22;0})^2 + (\sigma_{33;0})^2}}$	$l_{2;0} = \sqrt{1/3} = 0.58\ [-]$	$l_{2;0} = \sqrt{\frac{15.6^2}{12^2 + 15.6^2 + 12^2}} = 0.52\ [-]$
$c = f(c_0, A_{11}, b_1, l_2)$	$c_{l_{2;0}=0.58} = 4.10\ MPa$	$c_{l_{2;0}=0.52} = 4.22\ MPa$

Table 32: Initial cohesion – Comparison between isotropic and anisotropic initial stresses.

Therefore, with that set of parameters, we find an initial cohesion of $4.22\ MPa$ instead of $4.10\ MPa$, due to the anisotropy of the initial stresses (4.1MPa corresponds to the cohesion for an isotropic loading). Consequently, the shifting results in the increase of $0.28\ MPa$ of the initial cohesion.

The experimental data's are obtained from simple compression tests on samples with different orientations (0°, 30° and 90°). These values of cohesion are shifted upwards by $0.28\ MPa$, giving three new points that we can interpolate by a second order curve. Using the following typical expression for a second-order polynomial

$$y = \mathrm{B}_2.x^2 + B_1.x + B_0 \qquad \textbf{(75)}$$

We can obtain the three desired parameters: c_0, b_1, A_{11} by solving the set of equations:

$$\begin{cases} B_2 = \ \ 9.c_0.b_1.(A_{11})^2 \\ B_1 = -3.c_0.(A_{11} + 2.b_1.(A_{11})^2) \\ B_0 = \ \ \ c_0.(1 + A_{11} + b_1.(A_{11})^2) \end{cases} \qquad \textbf{(76)}$$

and finally find:

$$c_0 = 4.38\ MPa, \quad A_{11} = 0.1096, \qquad b_1 = 15.208$$

Hydromechanical modelling of a ventilation test in the Underground Research Laboratory of ANDRA

Abstract

When producing electricity, nuclear energy plays an important role in our modern societies: more than 13 % of the world electricity production comes from nuclear sources. This share rises up to 75 % in France. With its 58 nuclear reactors among the 439 operational around the world, it is the country the most dependent on nuclear electricity. However, the nuclear wastes generated can be extremely harmful to man and nature, in such a way that it is crucial to isolate them. Deep geological storage was thus selected as a potential solution for the most critical wastes. Yet, the feasibility of such task is still under study. In France, ANDRA runs scientific research programs that investigate the storage possibilities in the Callovo-Oxfordian argillite, located at a depth between 400 and 600 m in the Meuse/Haute-Marne region.

An underground research laboratory (URL) was installed in the rock formation. It carries out series of experiments to study the thermal, hydraulic and mechanical behaviours of the rock formation following the disposal phase (excavation, wastes storage and sealing). Among these, the Saturation Damaged Zone (SDZ) experiment investigates the impact of the exploitation phase in the argillite through saturation/desaturation cycles (i.e. ventilation test). In particular, the excavation damaged zone (EDZ) and its evolution has to be characterised.

In this context, one of the main contributions of this work is to propose laws of behaviour that modify the hydraulic parameters on the basis of the mechanical variables, such that the hydraulic behaviour of the medium evolves in the same way regardless of the orientation. Furthermore, we developed a formulation able to describe correctly the EDZ by correlating the intrinsic permeability of the medium with the ratio of plasticity. Then, the influence of the ventilation test itself was examined in further details. Among the aspects discussed, the analysis of the influence of the mass transfer coefficient suggested that using values determined through drying tests was possible. In addition to that, the work also introduced the concept of anisotropy of the mechanical parameters and explores the limitations of the newly proposed formulation.

Résumé

Dans nos sociétés modernes, l'énergie nucléaire joue un rôle important lors de la production d'électricité : plus de 13% de la production d'électricité mondiale provient du nucléaire. En France, cette part monte jusqu'à 75%. Avec ses 58 réacteurs nucléaires parmi les 439 opérationnels dans le monde, c'est le pays le plus dépendant de l'électricité nucléaire. Cependant, cela génère des déchets radioactifs nocifs pour l'Homme et la nature ; de telle sorte qu'il faille à tout prix les isoler. Le stockage géologique profond a été sélectionné comme solution potentielle pour les déchets les plus critiques. Or, la faisabilité d'une telle tâche reste toujours en cours de recherche. En France, ANDRA mène des programmes de recherche dédiés à l'étude des possibilités de stocker dans les couches de l'argilite du Callovo-Oxfordien, situé entre 400 et 600 m de profondeur, dans la région de la Meuse/Haute-Marne.

Un laboratoire de recherche souterrain fut installé dans cette formation rocheuse. On y mène des séries d'expériences axées sur les comportements de nature thermique, hydraulique et mécanique que la roche adopte suite à la phase de stockage (excavation, entreposage des déchets et scellement). Parmi ces aspects, l'expérience de la zone endommagée saturée (SDZ) enquête l'impact de la phase d'exploitation sur l'argilite à travers des cycles de saturation/désaturation (i.e. test de ventilation). Plus particulièrement, il s'agit de caractériser la zone excavée endommagée (EDZ) ainsi que son évolution.

Dans ce contexte, une des majeures contributions de ce travail est de proposer des lois de comportement qui modifient les paramètres hydrauliques sur base des variables mécanique, de telle sorte que le comportement hydraulique du milieu évolue de la même manière et ce, peu importe l'orientation considérée. En outre, ce travail développe une formulation capable de décrire correctement l'EDZ en corrélant la perméabilité intrinsèque du milieu avec le ratio de plasticité. Ensuite, l'influence du test de ventilation en lui-même est étudiée plus en détails. Parmi les sujets abordés, l'analyse de l'influence du coefficient de transfert montre qu'il est possible de servir des valeurs déterminées au moyen de tests de séchage pour modéliser le test. A côté de cela, le travail introduit le concept d'anisotropie des paramètres mécaniques, et explore les limites du la nouvelle formulation proposée.

Academic Year 2014-2015 Công-Tâm THAI